Measurement of the fiducial differential Higgs cross-section with respect to p_{T} using the diphoton decay channel at $\sqrt{s} = 8\,\mathrm{TeV}$ with ATLAS

Dissertation

zur Erlangung des Doktorgrades
an der Fakultät für Mathematik,
Informatik und Naturwissenschaften
Fachbereich Physik der Universität Hamburg

vorgelegt von

Christopher James Hengler

Hamburg
2017

Datum der Disputation:	03.07.2017
Vorsitzender der Prüfungskommission:	Prof. Dr. Dieter Horns
Gutachter/in der Dissertation:	Dr. Kerstin Tackmann
	Prof. Dr. Peter Schleper

Hiermit erkläre ich an Eides statt, dass ich die vorliegende Dissertationsschrift selbst verfasst und keine anderen als die angegebenen Quellen und Hilfsmittel benutzt habe.

Hamburg, den 27.01.2017 Christopher Hengler

I hereby declare, on oath, that I have written the present dissertation by my own and have not used other than the acknowledged resources and aids.

Hamburg, 27.01.2017 Christopher Hengler

Abstract

This thesis presents a measurement of the fiducial differential cross-section with respect to p_{T} of Higgs boson production, using the diphoton decay channel. The analysis uses $20.3\,\mathrm{fb}^{-1}$ of proton-proton collision data at a centre-of-mass energy of $8\,\mathrm{TeV}$ taken with the ATLAS detector in the year 2012. The diphoton invariant mass spectrum is measured, and a fitting procedure is used to extract the signal. The measured signal is corrected for detector inefficiencies and resolution effects to produce a fiducial differential cross-section, which is compared to theoretical predictions. The measurement is statistically limited, but broadly compatible with theoretical expectations.

Zusammenfassung

Diese Arbeit präsentiert eine Messung des differenziellen Wirkungsquerschnitts für die Produktion von Higgs Bosonen als Funktion des Transversalimpulses. Die Analyse nutzt den Zerfallskanal $H \rightarrow \gamma\gamma$ mit Daten von $20.3\,\mathrm{fb}^{-1}$ gesammelt vom ATLAS-Experiment im Jahr 2012. Das Spektrum der invarianten Masse des Zwei-Photonen-Systems ist gemessen und das Signal ist mit einer Ausgleichtsfunktion extrahiert. Das gemessene Spektrum ist um Detektorineffizienz und -auflösung korrigiert, um einen differenziellen Wirkungsquerschnitt zu produzieren. Der differenzielle Wirkungsquerschnitt ist mit theoretischen Vorhersagen verglichen. Die Präzision des Spektrums ist durch Statistik limitiert, aber das Spektrum ist generell kompatibel mit Erwartungen von theoretischen Vorhersagen.

Acknowledgements

I would first like to thank my PhD supervisor, Kerstin Tackmann. I will be forever grateful for the valuable guidance she provided during the course of my PhD, and also for her patience and encouragement, without which this thesis might never have been completed.

I would also like to thank Peter Schleper, for providing the second review of this thesis and sitting on my defence committee. Additionally, I wish to thank Dieter Horns, Sven-Olaf Moch, and Christian Sander for giving up their time to be a part of my defence committee.

Thank you to Mike Medinnis and Ingrid Gregor, for making the ATLAS group a pleasant working environment, and to all the friends I made within the group. To mention you all by name would double the length of this thesis, but I want to especially thank my office mate Marco Filipuzzi for the moral support as we each reached the end of our time as PhD students. I also wish to especially thank Elisabeth Petit and Marcos Jimenez, both of whom were a pleasure to work closely with, and taught me so much.

Thank you also to Alberto, Fede, Timon, and so many more, for the friendly competition on the football pitch over the last six years (and counting).

Finally, thank you to my wonderful parents, who never stopped supporting or believing in me.

Preface

The work presented in this thesis was performed as a member of the ATLAS collaboration. Many results presented within benefit from work performed by other members of the collaboration. The direct individual contributions of the author are noted here.

In chapter 5, the measurement of photon identification efficiencies at $\sqrt{s} = 8\,\text{TeV}$ via the electron-extrapolation method and the assessment of all uncertainties on this measurement is the work of the author. This work was published as a part of [1], alongside contributions from several ATLAS colleagues.

In chapter 6, the measurement of the fiducial differential cross-section in p_{T} was performed working in parallel to a similar analysis [2] by other members of the ATLAS collaboration, and the evaluation of many major sources of systematic uncertainty is the work of those colleagues. The fitting procedure from which the fiducial differential cross-section is derived was performed independently by the author for this thesis and the evaluation of the systematic and statistical uncertainties resulting from the fitting procedure is the work of the author. Also in chapter 6, the study of the contribution of various production modes to the overall Higgs boson production rate is entirely the work of the author, as is the evaluation of how the precision of this method may evolve as a function of integrated luminosity.

Contents

List of Figures

List of Tables

Chapter 1

Introduction

The Standard Model of particle physics was developed in the second half of the 20^{th} century, as a description of fundamental particles and the interactions between them. In addition to providing accurate descriptions of previously observed physical phenomena, the Standard Model has made numerous predictions (such as the existence of the W and Z bosons, and the top and charm quarks) which were later verified experimentally. One aspect of the Standard Model which until recently remained unverified was the mechanism by which fundamental particles gain mass. In the 1960s, the Higgs mechanism was proposed, in which an additional scalar field spontaneously breaks the gauge symmetry of the Standard Model giving mass to the elementary particles. The existence of this field also implies the existence of a scalar boson, known as the Higgs boson. In the year 2012, the first experimental observations of this particle were made by the ATLAS and CMS collaborations.

Since the first observation, the collection of additional data has allowed for further investigation of the newly-discovered particle's properties. This thesis describes a measurement of the Higgs boson production differential cross-section in p_{T} with

the $H \to \gamma\gamma$ decay channel, using data collected with the ATLAS detector at the LHC in the year 2012.

Chapter 2 gives a description of the particles and forces of the Standard Model of particle physics. A description of the Higgs mechanism is provided, and the production and decay modes of the Higgs boson are discussed.

Chapter 3 describes the LHC accelerator at CERN, and the ATLAS detector. Particular attention is given to the components of the ATLAS detector which play important roles in the reconstruction and identification of photons.

Chapter 4 gives a description the 2012 ATLAS dataset. The methods by which electrons and photons are reconstructed in ATLAS data are described. A description is given of the electron and photon energy calibration procedure.

Chapter 5 describes a measurement of the efficiency of the method used to identify photons within the ATLAS detector. A method by which the photon identification efficiency can be extrapolated from studies of $Z \to e^+e^-$ events is described. The relevant systematic uncertainties are described and evaluated, and the results of the measurement are presented. A description is given of the way this result is combined with the results of two other studies, extending the photon identification efficiency measurement to a wider p_{T} range and allowing for reduced uncertainty on the measured values in the p_{T} regions where multiple mesaurements are available.

Chapter 6 describes the measurement of the Higgs boson production differential cross-section in p_{T}. To provide context, the first observation of the Higgs boson by the ATLAS and CMS experiments in 2012 is discussed. The theoretical expectations are described. The choice of p_{T} binning is motivated, and the event selection process is described. The sources of systematic uncertainty on the differential cross-section measurement are described and evaluated. The method used for signal extraction is described, and the measured p_{T} distribution is presented and compared to theoretical predictions. A method is described by which the shape of

the observed p_{T} distribution can be used to measure the relative contributions of various Higgs boson production modes to the overall Higgs boson production rate. The results of applying this method to the observed p_{T} distribution are described, and a comparison is made to theoretical expectations. A study is undertaken to evaluate how the uncertainties on studies of this kind may develop as further data is taken.

Chapter 2

Theory

2.1 The Standard Model

The Standard Model (SM) of particle physics provides a description of the fundamental components of matter, and three of the four fundamental forces (the Standard Model does not describe gravity, which does no play an important role in the processes the Standard Model is concerned with). The Standard Model has been experimentally tested to high precision. In this chapter, an overview is provided of the Standard Model, and of the particles and forces it describes.

2.1.1 Particles of the Standard Model

The particles of the Standard Model can be split into two categories, based upon their spin. Particles with half-integer spin are referred to as *fermions*, while those with integer spin are known as *bosons*. Both types of particle are said to be indistinguishable. The fermions are so-called as they obey Fermi-Dirac statistics, in which no two particles may exist in the same state. Bosons similarly receive

their name as they obey Bose-Einstein statistics. The fermions are the building blocks of matter; bosons act as mediators of forces.

2.1.1.1 Fermions

Within the category of fermions, a further distinction can be drawn between *quarks*, which interact via the strong force, and *leptons*, which do not. The fermions exist in three families, each of which contains two quarks and two leptons.

Within each family, one quark has electric charge $+2/3$ (in order of increasing mass, the *up, charm*, and *top* quarks), and one $-1/3$ (the *down, strange*, and *bottom* quarks). Quarks also possess *colour charge*, which will be discussed in section 2.1.2.1.

Each family also possesses two leptons, one of which possesses electric charge -1 (the *electron, muon*, and *tau*), and one of which is neutrally charged (the *electron neutrino, muon neutrino* and *tau neutrino*).

The fermions described above are shown in table 2.1, along with their standard symbols and their electric charge. For each of these particles, there also exists an anti-particle of the same mass which has the opposite charge.

	Family			Charge
	I	II	III	
Quarks	up, u	charm, c	top, t	$+2/3$
	down, d	strange, s	bottom, b	$-1/3$
Leptons	electron neutrino, ν_e	muon neutrino, ν_μ	tau neutrino, ν_τ	0
	electron, e	muon, μ	tau, τ	-1

Table 2.1: The three families of fermions, and the standard symbols used to represent them.

2.1.1.2 Bosons

The Standard Model describes several spin-1 bosons, which act as mediators of interactions between particles. They may be categorised according to the forces with which they are associated. Photons, γ are the force-carrier particle for electromagnetic (EM) interactions. Gluons, g, mediate interactions of the strong force. The W^+, W^-, and Z bosons are associated with the weak force. These forces will be described in section 2.1.2.

This section omits the Higgs boson, which will be discussed in section 2.2.

2.1.2 Forces

The Standard Model describes three forces: the electromagnetic force, the weak force, and the strong force. The electromagnetic and weak forces can be considered aspects of the same *electroweak* (EW) interaction. The strong and electroweak interactions are described as quantum field theories, in which particles are considered as excited states of underlying fields. The Standard Model in its entirety combines the strong and electroweak interactions into one quantum field theory of the symmetry group $SU(3) \times SU(2) \times U(1)$.

2.1.2.1 The Strong Interaction

The strong force, also known as *quantum chromodynamics* (QCD), is a quantum field theory describing interactions between quarks and gluons. It is of symmetry group $SU(3)_C$, where the C denotes the colour charge to which the force couples. Quarks carry the three colour charges, which are typically labelled red, green and blue (r, g, b). Anti-quarks carry the opposite antired, antigreen, and antiblue charges ($\overline{r}, \overline{g}, \overline{b}$, sometimes described in combination as the *anticolour* charges).

There are eight gluons, each carrying a linear superposition of colour and anticolour charges (e.g. $red, antiblue$). Self-interaction among gluons is possible due to their colour-charge.

The coupling constant of the strong force, α_s, increases with distance, which leads to some interesting phenomena. Strong force interactions are weak at short distances, this phenomenon is known as *asymptotic freedom*. As a result of the strong interaction's strength at long distances, colour-charged particles are not observed freely, but only in bound, colour-singlet, states. This phenomenon is known as *colour confinement*. Bound states may take the form of baryons, made up of three quarks or three antiquarks, or mesons, consisting of a quark-antiquark pair. Some recent results[3] hint at the possibility that more exotic hadrons may also exist, although this remains to be confirmed.

2.1.2.2 The Electroweak Interaction

The electromagnetic and weak interactions appear, on the surface, rather different. The electromagnetic interaction has an infinite range; the weak interaction can occur only over a very short range (approximately 10^{-17} m). The electromagnetic interaction is parity-symmetric; the weak interaction is not (only left-handed particles participate in the weak interaction). Despite these differences, it has been shown that the two interactions can be described within a unified theory[4–6], referred to as the electroweak interaction.

The electroweak interaction is described by a quantum field theory of the symmetry group $SU(2)_L \times U(1)_Y$. Three gauge bosons are associated to the $SU(2)_L$ symmetry (the L denoting that they couple only to left-handed particles), from this symmetry three gauge bosons are predicted, labelled W^i_μ (where $i = 1, 2, 3$), which couple to weak isospin. The $U(1)_Y$ symmetry gives rise to one gauge boson, labelled B_μ, which couples to hypercharge.

The electroweak Lagrangian has the form:

$$\mathcal{L}_{EW} = i\overline{\psi}_L \gamma^\mu \partial_{\mu L} \psi_L + i\overline{\psi}_R \gamma^\mu \partial_{\mu R} \psi_R - \frac{1}{4} W^i_{\mu\nu} W^{\mu\nu}_i - \frac{1}{4} B^i_{\mu\nu} B^{\mu\nu}_i \,, \tag{2.1}$$

where the first two terms relate to the interactions between fermionic and gauge fields, γ^μ are the Dirac matrices, and $\partial_{\mu L}$ and $\partial_{\mu R}$ are covariant derivatives introduced to maintain the local gauge invariance of the electroweak Lagrangian, defined:

$$\partial_{\mu L} \phi_L = (\partial_\mu + ig \frac{\sigma_i}{2} W^i_\mu + ig' \frac{Y_L}{2} B_\mu) \phi_L \,, \tag{2.2}$$

$$D_{\mu R} \phi_R = (\partial_\mu + ig' \frac{Y_R}{2} B_\mu) \phi_R \,, \tag{2.3}$$

where σ_i are the Pauli matrices, g and g' denote the coupling constants of $SU(2)_\mathrm{L}$ and $U(1)_\mathrm{Y}$ respectively, and Y_L and Y_R are the left- and right-handed components of the fermion fields.

The remaining two terms of equation (2.1) are the gauge field terms, where:

$$W^i_{\mu\nu} = \partial_\mu W^i_\nu - \partial\nu W^i_\mu - g\epsilon^{ijk} W^j_\mu W^k_\nu \,, \tag{2.4}$$

where $\epsilon^{i,j,k}$ are the structure constants of the $SU(2)_L$ symmetry group, and

$$B^i_{\mu\nu} = \partial_\mu B^i_\nu - \partial_\nu B^i_\mu \,. \tag{2.5}$$

The four gauge bosons, γ, W^+, W^-, and Z, arise from linear combinations of the four gauge fields:

$$A_\mu = B_\mu \cos\theta_W + W^3_\mu \sin\theta_W \,, \tag{2.6}$$

$$Z_\mu = -B_\mu \sin\theta_W + W^3_\mu \cos\theta_W \,, \tag{2.7}$$

$$W^\pm_\mu = \frac{W^1_\mu \mp W^2_\mu}{\sqrt{2}} \,, \tag{2.8}$$

where θ_W is the weak mixing angle, also known as the Weinberg angle, and is given by:

$$\cos\theta_W = \frac{g'}{\sqrt{g^2 + g'^2}} \,, \tag{2.9}$$

$$\sin\theta_W = \frac{g}{\sqrt{g^2 + g'^2}} \,. \tag{2.10}$$

The gauge bosons associated with the electroweak force are described here as massless particles. While the photon, the mediating particle of the electromagnetic interaction, is indeed massless, the theoretical prediction of massless gauge bosons mediating the weak interaction is directly contradicted by experimental data, in which the weak interaction is observed to act only over a short range, and the W and Z bosons are observed to be massive. However, the introduction of a mass term into the electroweak Lagrangian leads to the breaking of local gauge invariance. A mechanism was proposed[7–10] in the 1960s by which the $SU(2)_L \times U(1)_Y$ symmetry of the electroweak interaction is spontaneously broken, allowing for the generation of non-zero $W^\pm$ and Z boson masses without breaking the local gauge invariance of the electroweak Lagrangian.

2.1.3 Spontaneous Symmetry Breaking and the Higgs Mechanism

The dynamics of a field theory are described by the Lagrangian, whose symmetry may be broken in two ways. One method, explicit symmetry breaking, simply

involves the addition of a symmetry-breaking term to the symmetric Lagrangian:

$$\mathcal{L} = \mathcal{L}_{\text{sym}} + \mathcal{L}_{\text{breaking}} \,, \tag{2.11}$$

where $\mathcal{L}_{\text{sym}}$ is the symmetric Lagrangian, and $\mathcal{L}_{\text{breaking}}$ an additional symmetry-breaking term. In the case of a vanishing $\mathcal{L}_{\text{breaking}}$ term, this reduces to the symmetric Lagrangian, and the method is useful when the symmetry-breaking term is small and a perturbative treatment may be used. However, as there is no fundamental principle by which the form of the $\mathcal{L}_{\text{breaking}}$ term may be determined, it is somewhat artificial. An alternative form of symmetry-breaking is *spontaneous symmetry breaking SSB*). In SSB, the Lagrangian remains symmetric under particular group transformations, but the vacuum is made non-invariant.

A simple case demonstrating the concept is that of a complex scalar field, invariant under $U(1)$ group transformations, for which the Lagrangian can be expressed as:

$$\mathcal{L} = \partial_\mu \phi^* \partial^\mu \phi - V(\phi^* \phi) \,, \tag{2.12}$$

where

$$V(\phi^* \phi) = \mu \phi^* \phi + \lambda (\phi^* \phi)^2 \,, \tag{2.13}$$

and μ and λ are constants. For the theory to be physically meaningful, the potential must be bounded from below to ensure the existence of a stable ground state. As such, it is required that the value of λ be positive.

The system may be equivalently described as:

$$\mathcal{L} = \frac{1}{2} \partial_\mu \varphi_1 \partial^\mu \varphi_1 + \frac{1}{2} \partial_\mu \varphi_2 \partial^\mu \varphi_2 - V(\varphi_1^2 + \varphi_2^2) \,, \tag{2.14}$$

where φ_1 and φ_2 are real fields, related to ϕ and ϕ^* by:

$$\phi = \frac{\varphi_1 + i\varphi_2}{\sqrt{2}}; \quad \phi^* = \frac{\varphi_1 - i\varphi_2}{\sqrt{2}}\,. \tag{2.15}$$

This alternate Lagrangian is $O(2)$ symmetric, remaining invariant under the transformation

$$\begin{pmatrix} \varphi_1 \\ \\ \varphi_2 \end{pmatrix} \rightarrow \begin{pmatrix} \varphi_1' \\ \\ \varphi_2' \end{pmatrix} = \begin{pmatrix} \cos\theta & -\sin\theta \\ \\ \sin\theta & \cos\theta \end{pmatrix} \begin{pmatrix} \varphi_1 \\ \\ \varphi_2 \end{pmatrix}\,. \tag{2.16}$$

Particles in quantum field theories are defined as quantised fluctuations around the lowest energy state (the vacuum state) of the field. The value of the field which corresponds to this state is known as the vacuum expectation value (VEV) of the field, written $\langle 0|\,\phi\,|0\rangle \equiv \phi_0$. Particle spectra are found by expanding the potential around its minimum:

$$\begin{aligned} V(\varphi_1,\varphi_2) = V(\varphi_{1,0},\varphi_{2,0}) &+ \sum_{a=1,2}\left(\frac{\partial V}{\partial\varphi_a}\right)_0 (\varphi_a - \varphi_{a,0}) \\ &+ \frac{1}{2}\sum_{a,b=1,2}\left(\frac{\partial^2 V}{\partial\varphi_a\partial\varphi_b}\right)_0 (\varphi_a - \varphi_{a,0})(\varphi_b - \varphi_{b,0}) + \cdots\,, \end{aligned} \tag{2.17}$$

where $\phi_0 = (\varphi_{1,0},\varphi_{2,0})$ is the VEV of $\phi = (\varphi_1,\varphi_2)$. Since ϕ_0 is, by definition, the field value which minimises the value of the potential V, the second term here is necessarily zero. Diagonalising the *mass matrix* (the factor $\frac{\partial^2 V}{\partial\varphi_a\partial\varphi_b}$ from the third term) gives the particle spectrum.

In the case where $\mu > 0$, the field has one unique minimum, which corresponds to the VEV. When $\mu < 0$, this is no longer the case. The potential takes the shape illustrated in 2 dimensions in figure 2.1

$$V(\varphi_2^2 + \varphi_2^2) = \frac{\mu}{2}(\varphi_1^2 + \varphi_2^2) + \frac{\lambda}{4}(\varphi_1^2 + \varphi_2^2)^2\,, \tag{2.18}$$

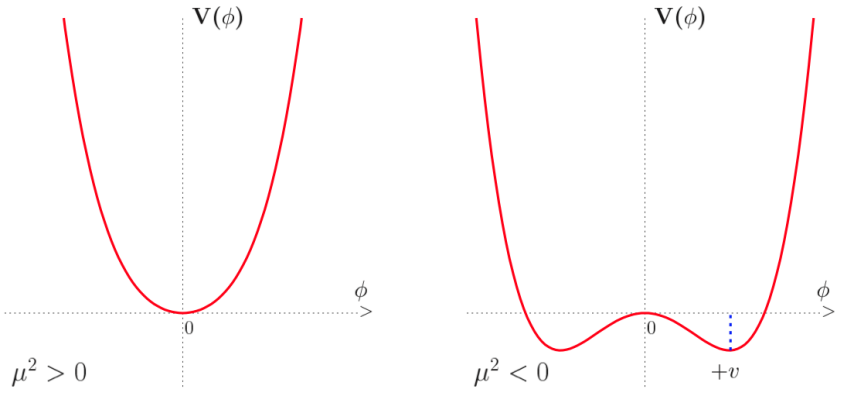

FIGURE 2.1: An illustration[11] of how the sign of the μ parameter alters the shape of the potential V.

and minima are found in degenerate states with $\varphi_1 \neq 0$ and/or $\varphi_2 \neq 0$, wherever:

$$\left(\frac{\partial V}{\partial \varphi_1}\right)_0 = \mu\varphi_{1,0} + \lambda\varphi_{1,0}(\varphi_{1,0}^2 + \varphi_{2,0}^2) = 0\,, \qquad \left(\frac{\partial V}{\partial \varphi_2}\right)_0 = \mu\varphi_{2,0} + \lambda\varphi_{2,0}(\varphi_{1,0}^2 + \varphi_{2,0}^2) = 0\,, \tag{2.19}$$

leading to the condition

$$\varphi_{1,0}^2 + \varphi_{2,0}^2 = \frac{-\mu^2}{\lambda} \equiv v^2\,. \tag{2.20}$$

There is no longer a unique vacuum state, but rather the potential has minima at all points along a circle of radius $v = \sqrt{\mu^2/\lambda}$ in the φ_1, φ_2 plane. Any of these stable minima may be arbitrarily chosen as the physical vacuum, and this choice spontaneously breaks the $U(1)$ symmetry. A convenient choice is $\varphi_{1,0} = v, \varphi_{2,0} = 0$, choosing this point gives a mass matrix:

$$m^2 = \begin{pmatrix} 2\lambda v^2 & 0 \\ 0 & 0 \end{pmatrix}\,. \tag{2.21}$$

The field $\varphi_1' = \varphi_1 - v$ thus corresponds to a particle of mass $m^2 = 2\lambda v^2$, while

$\varphi'_2 = \varphi_2$ corresponds to a massless particle. The Lagrangian may also be rewritten using these fields, as

$$\mathcal{L} = \frac{1}{2}(\partial_\mu \varphi'_1)^2 + \frac{1}{2}(\partial_\mu \varphi'_2)^2 - \frac{1}{2}(2\lambda v^2)\varphi'^2_1 + \lambda v \varphi'_1(\varphi'^2_1 + \varphi'^2_2) - \frac{\lambda}{4}(\varphi'^2_1 + \varphi'^2_2)^2\,, \quad (2.22)$$

which, as a result of the broken symmetry of the vacuum state, no longer has the $O(2)$ symmetry of the original Lagrangian (2.14). It can be shown[12] to be generally the case that breaking a continuous global symmetry in this way results in the appearance of a massless scalar boson. This is the Goldstone theorem, and these particles are known as Goldstone bosons.

The Higgs mechanism is a particular application of the Goldstone theorem to the electroweak sector of the Standard Model, which allows for the generation of non-zero masses for the $W^\pm$ and Z bosons. The Higgs field, labelled as Φ_H, is introduced, taking the form of a complex scalar doublet:

$$\Phi_H = \frac{1}{\sqrt{2}} \begin{pmatrix} \Phi^+ \\ \Phi^0 \end{pmatrix} = \frac{1}{\sqrt{2}} \begin{pmatrix} \phi_1 + i\phi_2 \\ \phi_3 + i\phi_4 \end{pmatrix}\,, \quad (2.23)$$

where Φ^+ is a charged scalar field and Φ^0 a neutral scalar field. As well as being a doublet under $SU(2)$, Φ also carries a weak hypercharge associated with $U(1)$, which will be denoted here as Y. The Lagrangian for these scalars can be written as

$$\mathcal{L}_{scalar} = \partial_\mu \Phi^\dagger_H \partial^\mu \Phi_H - V(\Phi^\dagger_H \Phi_H)\,, \quad (2.24)$$

with the covariant derivative:

$$\partial_\mu \Phi_H = \left(\partial_\mu - ig\frac{\sigma_i}{2}W^i_\mu - \frac{ig'}{2}YB_\mu\right)\Phi_H\,, \quad (2.25)$$

The gauge invariant potential is of the form:

$$V(\Phi_H^\dagger \Phi_H) = \mu^2 \Phi_H^\dagger \Phi_H + \lambda(\Phi_H^\dagger \Phi_H)^2 \,, \tag{2.26}$$

where $\mu^2 < 0$ and $\lambda > 0$. As illustrated for the simpler $U(1)$ case in figure 2.1, with $\mu^2 > 0$, the minimum value of the potential has a unique solution – and therefore a unique ground state – at the origin. Constraining $\mu^2 < 0$ again forces the potential to develop a local maximum at $\Phi_H = 0$, while many degenerate minima are found where:

$$\frac{1}{2}(\phi_1^2 + \phi_2^2 + \phi_3^2 + \phi_4^2) = \frac{-\mu^2}{2\lambda} \,. \tag{2.27}$$

The solutions to this equation trace a hypersphere in 4-dimensional space. While there are infinite solutions, a convenient choice is:

$$\phi_1 = 0; \quad \phi_2 = 0; \quad \phi_4 = 0; \quad \phi_3^2 = \frac{-\mu^2}{\lambda} = v \,, \tag{2.28}$$

which leads to a VEV of

$$\Phi_{H,0} \equiv \langle 0 | \, \Phi_H \, | 0 \rangle = \begin{pmatrix} 0 \\ \\ v \end{pmatrix} \,, \tag{2.29}$$

spontaneously breaking the symmetry of the theory.

This choice of solution is not arbitrary, but motivated by the fact that each broken symmetry results in the generation of a non-zero mass for the corresponding gauge boson. The $U(1)_{em}$ symmetry associated to the electromagnetic interaction should thus be unbroken, as photons are observed to be massless. By applying the electric

charge operator Q:

$$Q\Phi_{H,0} = (T^3 + \frac{Y}{2})\Phi_{H,0} = \begin{pmatrix} 1 & 0 \\ 0 & 0 \end{pmatrix} \begin{pmatrix} 0 \\ v \end{pmatrix} = 0\,, \tag{2.30}$$

it can be seen that the transformation $\Phi_{H,0} \to \Phi'_{H,0} = e^{i\epsilon Q}\Phi_{H,0}$ results in $\Phi'_{H,0} = \Phi_{H,0}$ for any arbitrary value of ϵ, and so the symmetry is unbroken and no mass is produced for the photon.

The field Φ_H may now be rewritten as:

$$\Phi_H = \begin{pmatrix} \Phi^+ \\ \Phi^0 \end{pmatrix} = e^{i\sigma^i\xi_i/v} \begin{pmatrix} 0 \\ v + H \end{pmatrix}\,, \tag{2.31}$$

replacing the original 2 complex scalar fields with 4 real fields, labelled ξ_i (for $i = 1, 2, 3$) and H. The ξ_i fields correspond to Goldstone bosons, and the H field to a Higgs boson. The Lagrangian here can be rewritten in the unitary gauge, with the result that the 3 Goldstone bosons ξ_i are eaten by the $W^\pm$ and Z bosons. The $SU(2)$ transformation

$$U(\xi) = e^{-i\sigma^i\xi_i/v} \tag{2.32}$$

is applied, generating the fields:

$$\Phi'_H = U(\xi)\Phi_H = \frac{1}{\sqrt{2}}(v + H)\chi\,, \tag{2.33}$$

$$\vec{A}'_\mu = U(\xi)\vec{A}_\mu U(\xi)^{-1} - \frac{i}{g}(\partial_\mu U(\xi))U^\dagger(\xi)\,, \tag{2.34}$$

where $\chi = \begin{pmatrix} 0 \\ 1 \end{pmatrix}$. The Lagrangian in the unitary gauge is written

$$\mathcal{L}_{\text{scalar}} = (D_\mu\Phi_H)'(D^\mu\Phi_H)' - V(\Phi'^\dagger_H\Phi')\,, \tag{2.35}$$

where

$$(D_\mu \Phi_H)' = (\partial_\mu - ig\frac{\vec{\tau}}{2} \cdot \vec{A}'_\mu - \frac{i}{2} g' B'_\mu)(v + H)\chi \,. \tag{2.36}$$

The mass-squared terms for the gauge bosons of the weak interaction are given in the first term of (2.35), and can be written:

$$\mathcal{L}_{mass} = \frac{v^2}{8}(g^2 A'^1_\mu A'^{1\mu} + g^2 A'^2_\mu A'^{2\mu} + (g A'^3_\mu - g' B'_\mu)^2) \,. \tag{2.37}$$

By introducing the fields

$$W^\pm_\mu = \frac{A'^1_\mu \mp i A'^2_\mu}{\sqrt{(2)}} \,, \tag{2.38}$$

it is possible to rewrite the first and second terms of (2.37) in the form

$$\frac{1}{4} g^2 v^2 W^+_\mu W^{-\mu} \,, \tag{2.39}$$

giving a mass to the $W^\pm$ bosons of

$$m_W = \frac{1}{2} g v \,. \tag{2.40}$$

Meanwhile, the third term of (2.37) may be written as

$$\frac{v^2}{8}(A'^3_\mu B'_\mu) \begin{pmatrix} g^2 & -gg' \\ -gg' & g'^2 \end{pmatrix} \begin{pmatrix} A'^{3\mu} \\ B'^\mu \end{pmatrix} \,. \tag{2.41}$$

By applying the transformation

$$\begin{pmatrix} Z_\mu \\ A_\mu \end{pmatrix} = \begin{pmatrix} \cos\theta_W & -\sin\theta_W \\ \sin\theta_W & \cos\theta_W \end{pmatrix} \begin{pmatrix} A'^3_\mu \\ B'_\mu \end{pmatrix} \,, \tag{2.42}$$

where θ_W is the Weinberg mixing angle[5],

$$\sin\theta_W = \frac{g'}{\sqrt{g^2+g'^2}}\,; \quad \cos\theta_W = \frac{g}{\sqrt{g^2+g'^2}}\,, \tag{2.43}$$

(2.41) can be diagonalised as:

$$\frac{v^2}{8}(Z_\mu A_\mu)\begin{pmatrix} g^2+g'^2 & 0 \\ 0 & 0 \end{pmatrix}\begin{pmatrix} Z^\mu \\ A^\mu \end{pmatrix} = \frac{v^2}{8}(g^2+g'^2)Z_\mu Z^\mu + 0\cdot A_\mu A^\mu\,, \tag{2.44}$$

producing a mass for the Z boson of

$$m_z = \frac{1}{2}v\sqrt{g^2+g'^2}\,. \tag{2.45}$$

Another neutral boson remains massless, and so can be identified with the photon. A relationship between m_W and m_Z can be deduced from (2.43):

$$m_Z = \frac{m_W}{\cos\theta_W}\,. \tag{2.46}$$

After symmetry breaking, the form of the potential V becomes

$$V(\Phi_H'^\dagger\Phi') = -\frac{\mu^2v^2}{4} + \frac{1}{2}(2\mu^2)H^2 + \lambda v H^3 + \frac{\lambda}{4}H^4\,, \tag{2.47}$$

from which it can be seen that the Higgs boson should have mass

$$m_H = \sqrt{2\mu^2}\,, \tag{2.48}$$

and so the Lagrangian after SSB now describes two charged gauge bosons with mass m_W (2.40); two neutral gauge bosons, one massless and one with mass m_Z (2.45); and one Higgs boson with mass m_H.

2.1.3.1 Fermion masses

In this way an explanation is provided for the observed non-zero masses of the $W^{\pm}$ and Z bosons. So far, the fermions remain massless, but this is again in contradiction of observations. As was the case for the boson masses, the naïve introduction of a mass term $\mathcal{L}_m = -m(\bar{\psi}_L\psi_R + \bar{\psi}_R\psi_L)$ into the electroweak Lagrangian would break its local gauge invariance. It is, however, possible to generate fermion masses with the same Higgs doublet used to generate the masses of the gauge bosons by the addition of a Yukawa term, $\mathcal{L}_Y$, invariant under $SU(2) \times U(1)$:

$$\begin{aligned}\mathcal{L}_Y \;&=\; c_d^{i,j}(\bar{u}_i, \bar{d}_i)_L \Phi_L d_{jR} \;+\; c_u^{i,j}(\bar{u}_i, \bar{d}_i)_L \Phi_R u_{jR} \\ &+\; c_e^{i,j}(\bar{\nu}_{e_i}, \bar{e}_i)_L \Phi_L e_{jR} \;+\; c_\nu^{i,j}(\bar{\nu}_{e_i}, \bar{e}_i)_L \Phi_R \nu_{jR} \;+\; \text{h.c.}\,,\end{aligned} \tag{2.49}$$

where $c^{i,j}$ $i,j = 1,\ldots,N$, with N the number of fermion families, are matrices describing the so-called Yukawa couplings between the fermions and the Higgs doublet, and $\Phi_L = \begin{pmatrix} \Phi^+ \\ \\ \Phi^0 \end{pmatrix}$ and $\Phi_R = \begin{pmatrix} -\bar{\Phi}^0 \\ \\ \Phi^- \end{pmatrix}$ correspond to the left- and right-handed doublets respectively. By substituting Φ_L with $\begin{pmatrix} 0 \\ \\ v+H \end{pmatrix}$ and Φ_R with $\begin{pmatrix} v+H \\ \\ 0 \end{pmatrix}$, the Yukawa Lagrangian takes on a form:

$$\mathcal{L}_Y = \frac{1}{\sqrt{2}}(v+H)(c_d^{ij}\bar{d}_i d_i + c_u^{ij}\bar{u}_i u_i + c_e^{ij}\bar{e}_i e_i)\,, \tag{2.50}$$

therefore generating fermion mass terms of the form:

$$m_d^i = -c_d^{ij}\frac{v}{\sqrt{2}}; \quad m_u^i = -c_u^{ij}\frac{v}{\sqrt{2}}; \quad m_e^i = -c_e^{ij}\frac{v}{\sqrt{2}}\,, \tag{2.51}$$

where the mass terms m_d^i, m_u^i, and m_e^i depend upon c_d^{ij}, c_u^{ij}, and c_e^{ij} respectively. Note that Yukawa coupling does not produce any neutrino mass, due to the lack of a right-handed neutrino partner in the SM. By inspecting the form of these mass terms it is clear that the strength of the Yukawa coupling is proportional to the fermion mass. The Yukawa Lagrangian may also be re-written in such a way as to make this relationship clearer:

$$\mathcal{L}_Y = -\left(1 + \frac{H}{v}\right)\left(m_d^i \bar{d}_i d_i + m_u^i \bar{u}_i u_i + m_e^i \bar{e}_i e_i\right). \tag{2.52}$$

The Yukawa couplings are arbitrary parameters within the theory, but can be probed experimentally due to the relationship between Yukawa coupling and fermion mass.

2.2 The Higgs Boson

As described in section 2.1.3, the SM predicts the existence of the Higgs boson, with a mass m_H dependant upon the parameters v and λ. For the Higgs mechanism to explain the non-zero masses of the $W^{\pm}$ and Z bosons, m_H must be non-zero, but as λ is a characteristic of the Higgs field itself, the value of m_H cannot be predicted from theory alone. This mass is important as one of the free parameters of the Standard Model, and the preferred production and decay modes of the Higgs boson are strongly dependant upon its mass. The Higgs boson had for a long time been a theoretically-expected but unobserved particle. In 2012, both the ATLAS[13] and CMS[14] experiments observed a particle with properties expected of a Higgs boson, at a mass of around 126 GeV. This discovery and results of subsequent research will be discussed in detail in section 6.1, while this section presents some brief discussion of the properties expected of a Standard Model Higgs boson.

2.2.1 Production Modes

The Standard Model predicts several mechanisms by which the Higgs boson may be produced. Figure 2.2 illustrates the production cross-sections predicted by the Standard Model in proton-proton collisions at a centre-of-mass energy $\sqrt{s} =$ 8 TeV, as a function of m_H.

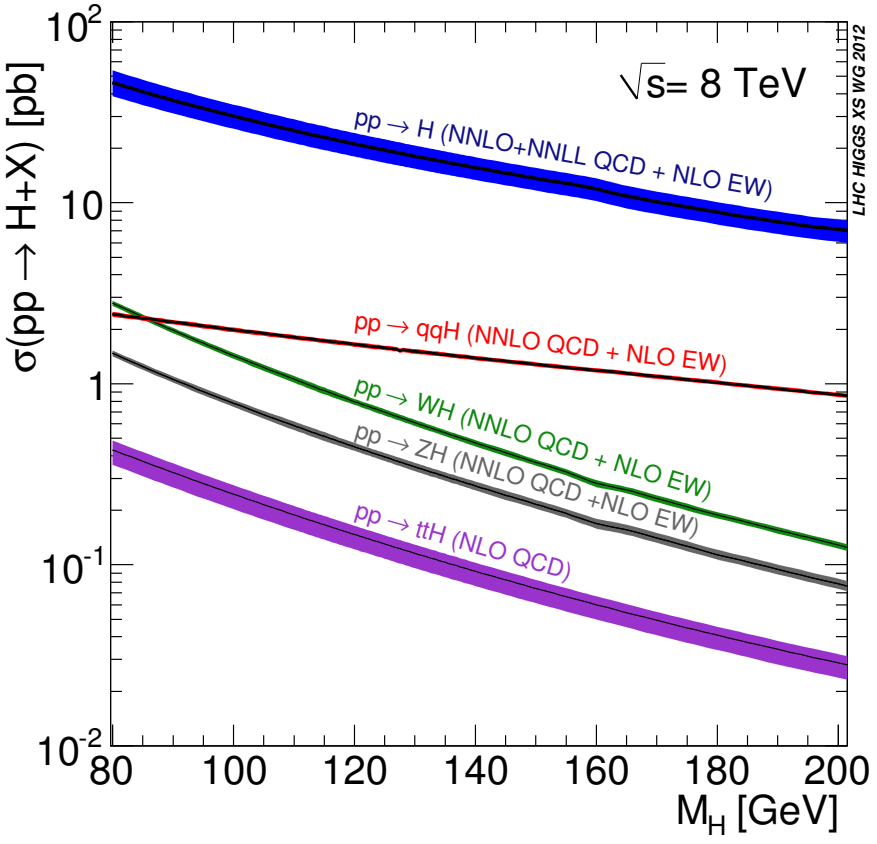

Figure 2.2: The production cross-sections predicted[15] for a Standard Model Higgs boson in proton-proton collisions at centre-of-mass energy $\sqrt{s} = 8$ TeV, as a function of the mass of the Higgs boson. The coloured bands indicate the uncertainties on the values.

The primary production mode in the LHC is gluon-gluon fusion ($gg \to H$, ggF production), in which gluons annihilate via a quark loop. This occurs predominantly via loops of top quarks, due to their strong coupling to the Higgs boson. This is by far the dominant production mode, with a cross-section approximately an order of magnitude larger than any other. The cross-section for ggF Higgs production

has been calculated at next-to-leading order (NLO)[16–18] and next-to-next-to-leading-order ($NNLO$) in QCD[19–21] with NLO QED corrections applied[22–24].

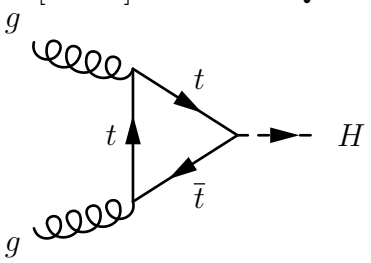

FIGURE 2.3: This Feynman diagram shows the production of a Higgs boson via gluon-gluon fusion, the dominant production mode according to SM predictions.

The second largest production mode is vector boson fusion ($qq' \rightarrow qq'H$, VBF production), in which two W or Z bosons radiated from quarks annihilate to produce a Higgs boson. The two quarks undergo hadronisation, typically producing a high-mass dijet system in the forward region of the detector. The region between the two jets is expected to be free of QCD activity, this is dissimilar to most QCD processes and can be exploited to improve background suppression. The cross-section is calculated with full QCD and QED corrections up to NLO[25, 26], and includes approximate NNLO QCD corrections[27].

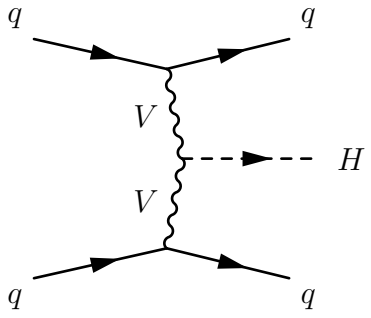

FIGURE 2.4: This Feynman diagram shows the production of a Higgs boson via vector boson fusion. The two V bosons indicated on the diagram may be either a pair of Z bosons or a W^+ and a W^-.

Associated W/Z production ($pp \rightarrow WH, pp \rightarrow ZH$; WH or ZH production respectively, also known as *Higgsstrahlung*), involves a Higgs boson being produced in association with a $W^{\pm}$ or Z boson. The W or Z boson is produced by coupling to a quark-antiquark pair, and then the Higgs boson is radiated off the weak boson.

Cross-sections for this production method include QCD corrections calculated to NNLO[28, 29] and QED corrections to NLO[30].

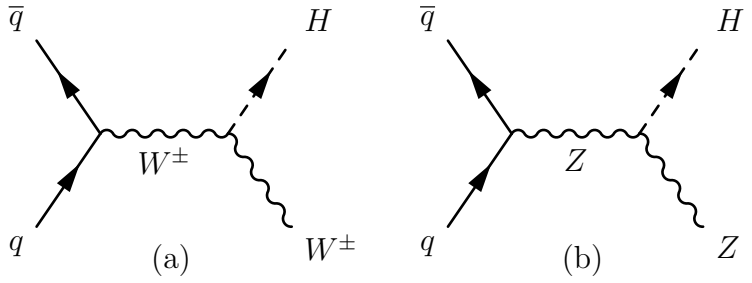

FIGURE 2.5: These Feynman diagrams show Higgs boson production via Higgsstrahlung, with a W boson and a Z boson in subfigures 2.5(a) and 2.5(b) respectively

Higgs bosons may also be produced in association with top quark pairs ($pp \rightarrow ttH$, ttH production). This production mode accounts for only a very small fraction of the total production cross-section, approximately two orders of magnitude less than the dominant ggF production mode. However, it is interesting as it has a relatively distinct experimental signature, due to the presence of the $t\bar{t}$ in the final state, and allows for a direct measurement of the top-Higgs Yukawa coupling. Cross-section calculations are performed with full QCD corrections up to NLO[31–34].

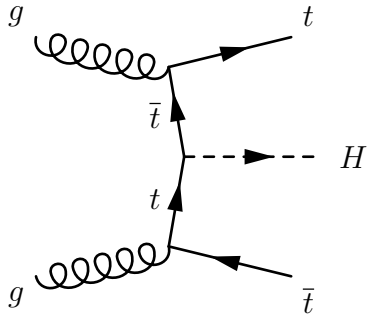

FIGURE 2.6: This Feynman diagram shows the production of a Higgs boson in association with a pair of top quarks.

2.2.1.1 THEORETICAL UNCERTAINTIES

One of the primary sources of uncertainty on theoretical predictions of the cross-sections of the various Higgs boson production modes is the uncertainty on the

parton distribution functions (*PDF*) used in the calculations. These PDFs are crucial to predicting the cross-section of any LHC process, as they describe the distribution of partons and their momentum within the photons. Specifically, the PDF $f_i(x, Q^2)$ describes the probability of finding a parton (i.e. a quark or gluon) of flavour i which carries a fraction x of the total momentum of the proton, where Q denotes the momentum transfer of the hard scattering process. PDFs are derived experimentally, using deep-inelastic scattering, the Drell-Yan process, and jet production data. A number of different groups produce PDFs independently. Significant differences can arise between the various PDFs as a result of factors such as different statistical treatments, different choices of α_s (the strong coupling constant), different parameterisations of the PDF, and the usage of different datasets in producing the PDF.

Another major source of uncertainty on the cross-section predictions is the so-called *scale dependence*. This term refers to the dependence of calculated cross-section on the QCD factorisation and renormalisation scales, μ_R and μ_F. In the ideal situation of calculations to all orders QCD predictions would not depend upon these values, which are not physical parameters and cannot be determined from data. However, QCD calculations cannot practically be made to all orders, and instead finite order calculations are made using a truncated perturbative expansion series. In this case, the results of the calculation are sensitive to the chosen values of μ_R and μ_F. The impact is especially significant for the gluon-gluon fusion production process. Performing calculations to higher orders generally results in a reduction of the effect. An uncertainty corresponding to this effect is estimated from the change in predicted cross-section when varying the values assigned to μ_R and μ_F.

Table 2.2 summarises the cross-section predicted by the Standard Model for a Higgs boson at mass $m_H = 125\,\text{GeV}$ in proton-proton collisions with $\sqrt{s} = 8\,\text{TeV}$ for each production mode. The table also displays the highest order to which QCD

and electroweak corrections are calculated for each production mode, and presents the uncertainties on the predicted cross-sections resulting from PDF uncertainties and QCD scale dependence.

	order (QCD)	order (EW)	σ [pb]	Scale [%]	PDF+α_s [%]
ggF	NNLO+NNLL	NLO	19.27	$+7.2\ -7.8$	$+7.5\ -6.9$
VBF	NNLO	NLO	1.578	± 0.2	$+2.6\ -2.8$
WH	NNLO	NLO	0.7046	± 1.0	± 2.3
ZH	NNLO	NLO	0.4153	± 3.1	± 2.5
ttH	NLO		0.1293	$+3.8\ -9.3$	± 8.1

TABLE 2.2: The predicted[35] production cross-sections for a Standard Model Higgs boson with mass $m_H = 125\,\text{GeV}$ in proton-proton collisions at $\sqrt{s} = 8\,\text{TeV}$, with uncertainties resulting from scale dependence and PDF-related uncertainties treated according to the PDF4LHC recommendations[36].

2.2.2 Decay Modes

The Higgs boson may decay into many final states via a number of decay channels. The channels with the largest branching ratios are displayed in terms of their decay cross-section, as a function of the Higgs mass m_H, in figure 2.7.

For an SM Higgs with m_H in the region of 125 GeV, the dominant decay channel is $H \to b\bar{b}$. The channel with the next highest cross-section in this mass region is $H \to W^+W^-$. The next largest contributions come from the $H \to \tau\tau$ channel and the $H \to gg$ channel (which proceeds via a quark loop, as gluons do not directly couple to the Higgs). Further contributions come from decays to other fermion pairs, or Z boson pairs. Additionally, the Higgs boson may decay via loops of W bosons or fermions (dominated by the top quark, due to its large Yukawa coupling) into either a photon pair or a Z boson plus a photon. These decay channels are illustrated in Feynman diagram form in figure 2.8.

The sensitivity which can be achieved when studying any given decay channel is dependent not only on the branching fraction, but also upon factors such as the

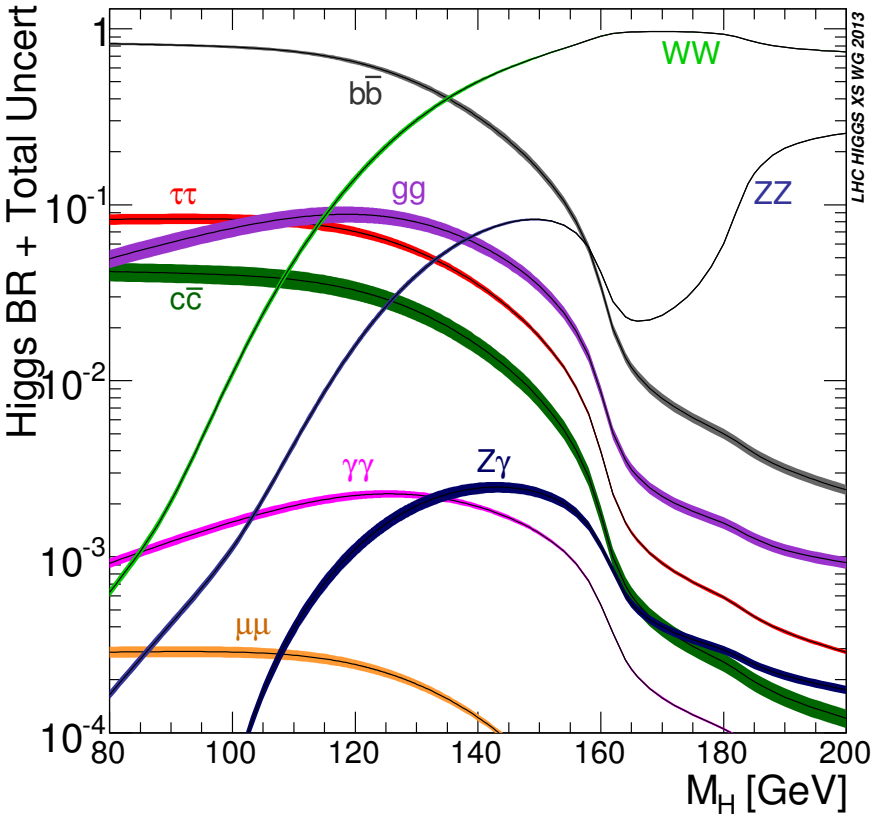

FIGURE 2.7: The decay cross-sections predicted[15] for a number of possible Higgs boson decay channels, as a function of Higgs boson mass m_H. The coloured bands indicate the uncertainties on the values.

signal selection efficiency, the resolution which can be achieved, and how much background exists for the final state. The $H \to b\bar{b}$ channel has a large cross-section and a final state which allows for reasonably precise measurement of the invariant mass, nevertheless it is rather challenging to study due to the large background resulting from QCD processes. The $H \to \tau\tau$ decay channel is promising due to its distinctive signature and reasonably large branching fraction, but also suffers from a significant background (predominantly from the $Z \to \tau\tau$ process).

The $H \to \gamma\gamma$ channel (via an intermediate quark or vector boson loop) is very sensitive despite a small small branching fraction, as its final state provides a clean detector signature and allows excellent invariant mass resolution. This channel will be discussed further in chapter 6.

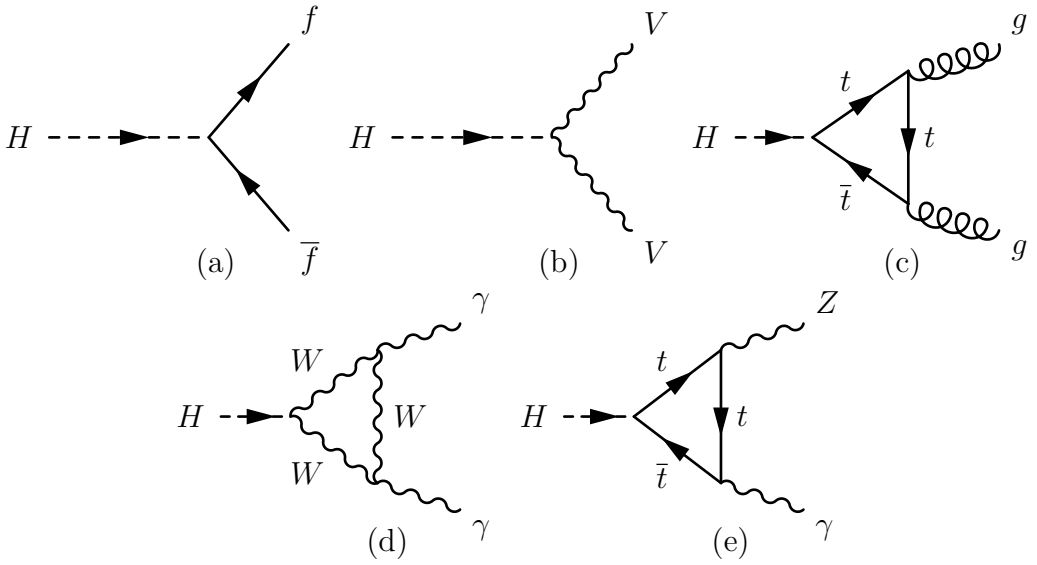

FIGURE 2.8: Feynman diagrams of the dominant decay modes of the Standard Model Higgs boson. Subfigures 2.8(a) and 2.8(b) show decay to a fermion-antifermion pair and a vector boson pair (W^+W^- or ZZ) respectively. Decay to a gluon pair via a top quark loop is shown in subfigure 2.8(c). Subfigure 2.8(d) shows decay to a photon pair via a W boson loop, and subfigure 2.8(e) illustrates the $H \to Z\gamma$ process proceeding via a top loop.

Decay mode	Branching fraction	Uncertainty (%)	
$H \to b\bar{b}$	5.77×10^{-1}	$+3.21$	-3.27
$H \to W^+W^-$	2.15×10^{-1}	$+4.26$	-4.20
$H \to gg$	8.57×10^{-2}	$+10.22$	-9.98
$H \to \tau\tau$	6.32×10^{-2}	$+5.71$	-5.67
$H \to c\bar{c}$	2.91×10^{-2}	$+12.17$	-12.21
$H \to ZZ$	2.64×10^{-2}	$+4.28$	-4.21
$H \to \gamma\gamma$	2.28×10^{-3}	$+4.98$	-4.89
$H \to Z\gamma$	1.54×10^{-3}	$+9.01$	-8.83

TABLE 2.3: The predicted[35] branching fractions for the dominant decay modes of an SM Higgs boson with mass $m_H = 125\,\text{GeV}$.

Chapter 3

The Large Hadron Collider and the ATLAS Detector

3.1 The Large Hadron Collider

The Large Hadron Collider (*LHC*) [37] is a particle accelerator located at the European Organisation for Nuclear Research (CERN), near Geneva, Switzerland. It is situated in an approximately-circular tunnel (formerly home to the *LEP* accelerator) which lies between 45 and 170 m below ground, with a circumference of around 27 km. The topics covered in this thesis relate to LHC operations as a proton-proton collider, however it is worth noting that the LHC program also includes operation with heavy ion beams (Pb), in both lead-lead and lead-proton modes. The first proton injections occurred in 2008, but the machine had to be shut down soon afterwards due to an electrical fault. Operation restarted on 20th November 2009, with the first recorded collisions taking place a few days later at the injection energy of 450 GeV per beam.

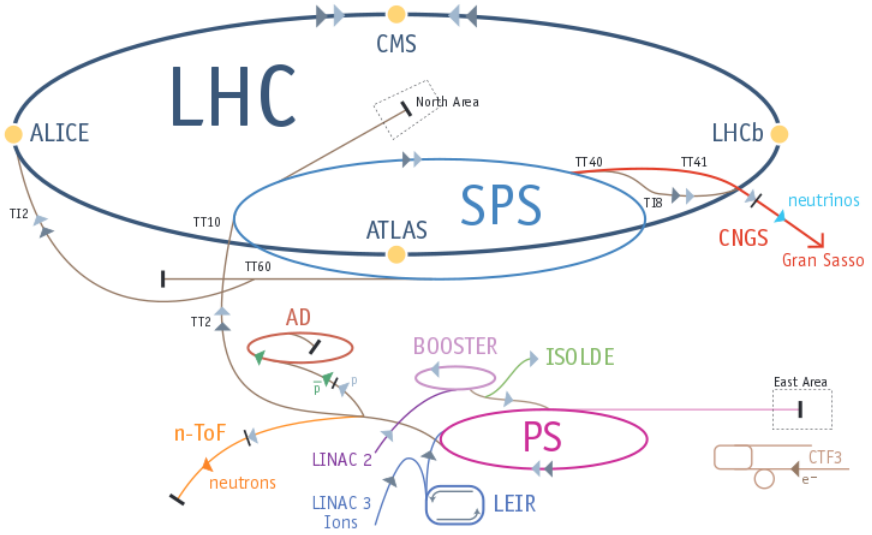

FIGURE 3.1: A diagram [38] illustrating the CERN accelerator complex, including the pre-accelerators used to prepare beams for injection into the LHC.

3.1.1 Pre-accelerator Chain

The LHC is designed for high-energy operations, and and so a series of pre-accelerators must be used to accelerate the beams before they are injected into the LHC. Protons are first accelerated by the linear accelerator *Linac2* up to an energy of around 50 MeV. From there, they are injected into the Proton Synchrotron Booster, a synchrotron accelerator which boosts the protons up to an energy of around 1.4 GeV. Another two, increasingly large, synchrotron accelerators follow: the Proton Synchrotron (*PS*), and the Super Proton Synchrotron (*SPS*), which accelerate the protons up to energies of 25 GeV and 450 GeV respectively. The SPS is the final stage of the pre-accelerator complex, and injects the beams into the LHC itself.

3.1.2 The LHC

After injection from the SPS into the LHC, beams are accelerated further to a centre of mass energy $\sqrt{s} = 8\,\text{TeV}$ (in the 2012 data-taking period; in 2010 and

2011 the machine operated at $\sqrt{s} = 7\,\text{TeV}$). The LHC is designed to provide a centre of mass energy $\sqrt{s} = 14\,\text{TeV}$ at an instantaneous luminosity of $10^{-34}\,\text{cm}\,\text{s}^{-1}$ when operating at full capacity. The instantaneous luminosity, $\mathcal{L}$, is given by the expression

$$\mathcal{L} = \frac{N_b^2 n_b f_{\text{rev}} \gamma_r}{4\pi \epsilon_n \beta^*} F \tag{3.1}$$

where:

- N_b is the number of particles per bunch,
- n_b is the number of bunches per beam,
- f_{rev} is the revolution frequency,
- γ_r is the relativistic gamma factor,
- ϵ_n is the transverse beam emittance,
- β^* is the beta function at the collision point:

  $$\beta^* = \frac{\sigma^2 \gamma_r}{\varepsilon_n} \tag{3.2}$$

  which relates the beam size, σ, to the beam's emittance, and
- F is the geometric luminosity reduction factor, resulting from the crossing angle of the beams at the interaction point:

  $$F = 1/\sqrt{1 + \left(\frac{\theta_c \sigma_z}{2\sigma^*}\right)^2} \tag{3.3}$$

  where θ_c is the crossing angle of the beams, σ_z is the RMS bunch length, and σ^* is the RMS transverse beam size at the interaction point (assuming equal parameters for both beams).

Parameter	2012	Design value
Energy per beam (TeV)	4	7
Number of protons per bunch	1.6–1.7×10^{11}	1.15×10^{11}
Number of bunches, n_b	1374	2808
Bunch spacing (ns)	50	25
Emittance, ε (µm rad)	2.5	3.75
Beta function, β^* (m)	0.6	0.55
Luminosity, $\mathcal{L}$ ($\mathrm{cm}^{-2}\,\mathrm{s}^{-1}$)	7.7×10^{33}	1×10^{34}

TABLE 3.1: This table presents typical LHC beam parameters from the 2012 data-taking period. The design values are also shown.

Table 3.1 shows typical beam parameters from the 2012 data-taking period[39], and the nominal design values[40]

The LHC supports four major experiments, *ALICE*, *ATLAS*, *CMS*, and *LHCb*. ATLAS and CMS are both general purpose detectors, designed for high sensitivity to a wide range of physics phenomena, both within and beyond the Standard Model. The ALICE detector specialised for studies of heavy-ion collisions, while LHCb is optimised for the purposes of studying CP violation and other phenomena in the physics of hadrons containing b quarks and other heavy flavours.

3.2 The ATLAS Detector

The ATLAS detector is located in a cavern approximately 90m underground at CERN's Meyrin campus, near the main CERN site on the outskirts of Geneva. The detector has a height of around 25 m and a length of approximately 44 m, and weighs around 7000 t. The detector is symmetric in the forward/backward regions with respect to the nominal interaction point.

3.2.1 The ATLAS Co-ordinate System

A right-handed cylindrical co-ordinate system is defined for usage within all ATLAS studies, with the origin centred on the nominal interaction point (*IP*). The z-axis is defined by the beam direction, the positive x-axis points from the IP to the centre of the LHC ring, and the positive y-axis is defined to point upwards. The azimuthal angle ϕ is measured around the beam axis, and the polar angle θ is the angle from the beam axis. Rapidity, y, is defined as $y = 1/2 \ln[(E + p_z)/(E - p_z)]$. For massless objects, this is equivalent to pseudorapidity, $\eta = -\ln \tan(\theta/2)$. The difference between y and η is negligible for stable, high p_{T} particles, and η is often used as an angular co-ordinate in place of θ. Angular separation, ΔR, between objects is defined as $\Delta R = \sqrt{\Delta\eta^2 + \Delta\phi^2}$. Transverse momentum ($p_{\mathrm{T}}$), transverse energy ($E_{\mathrm{T}}$), and missing transverse momentum ($E_{\mathrm{T}}^{\mathrm{miss}}$) are all defined in the x-y plane.

3.2.2 Design of the ATLAS Detector

The wide physics program of the ATLAS experiment imposes many requirements on the design of the detector[41]:

- LHC experimental conditions require fast, radiation-hard electronics
- High detector granularity is necessary, to handle high particle densities
- Large solid angle coverage
- Good momentum resolution for charged particle tracks
- High-performance electromagnetic and hadronic calorimeters
- Good muon identification, with high momentum resolution over a wide momentum range, and accurate charge discrimination for high p_{T} muons

- High efficiency triggers for low p_{T} objects, while maintaining good background rejection

A number of sub-detectors are designed to fulfill these requirements. These sub-detectors are arranged concentrically, as displayed in figure 3.2. The inner layers make up the Inner Detector (*ID*), primarily used for tracking of charged objects in the detector, vertex measurements, and identification of electrons and positrons. Outside the ID lie the calorimeters, designed to provide high resolution energy and position measurements for electrons, photons, and jets. At the outer region of the detector is the muon spectrometer, situated in a toroidal magnetic field of up to 3.5 T, which provides identification and momentum measurement of muons. Each subdetector can be split into two regions, the low-η *barrel* region (arranged concentrically around the beam line) and the high-η *endcap* region (aligned perpendicularly to the direction of the beam line, at each end of the detector).

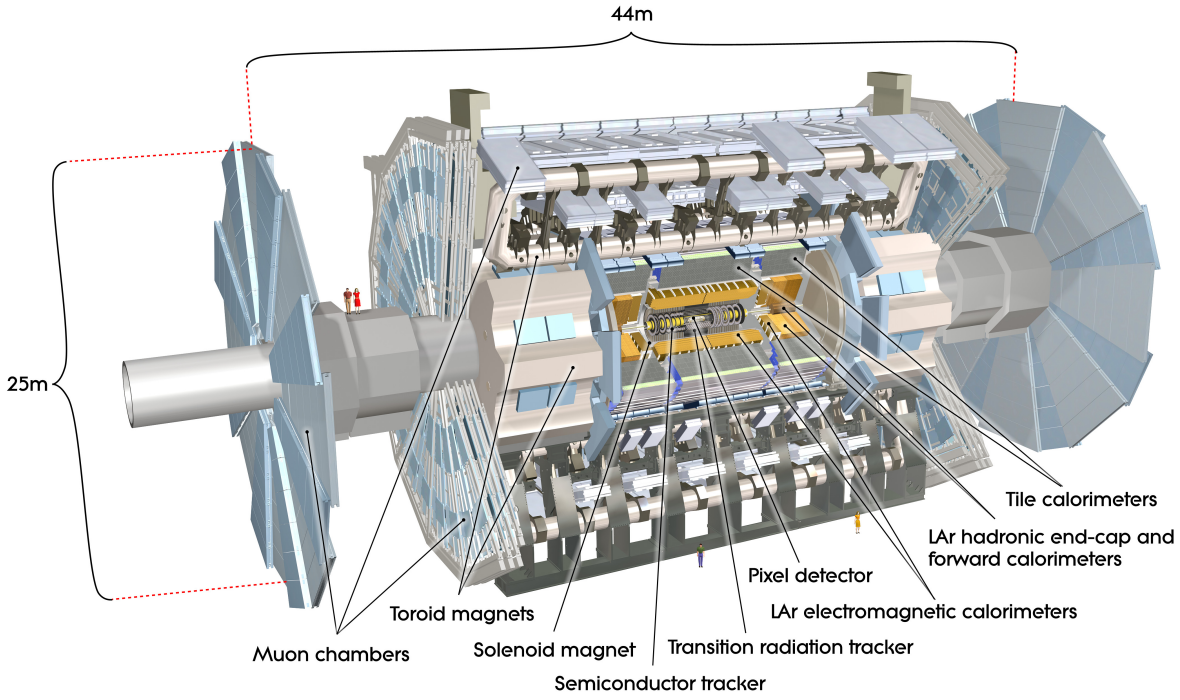

FIGURE 3.2: A computer generated image [41] of the ATLAS detector, with a cut-away to illustrate the inner layers

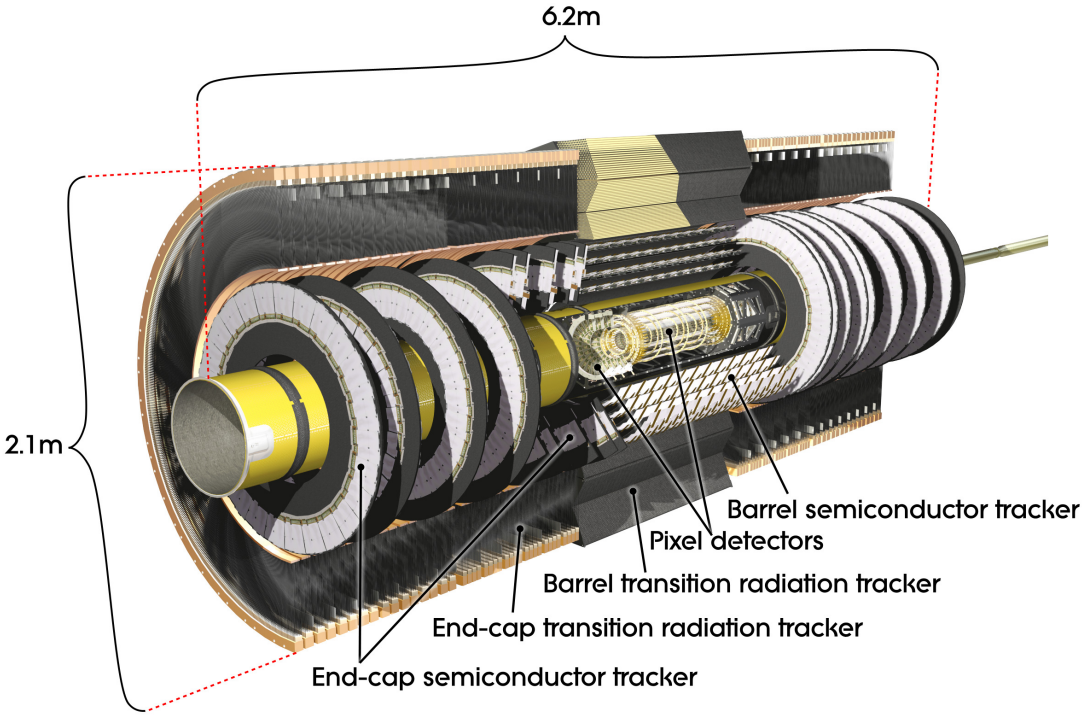

FIGURE 3.3: An illustration [42] of the ATLAS Inner Detector, with component sub-detectors labelled.

3.2.3 The Inner Detector

Positioned around the central beam pipe is the Inner Detector, designed to provide accurate tracking and momentum resolution, and determination of primary and secondary vertices. The ID can itself be broken down into a number of sub-components, illustrated in figure 3.3. It is surrounded by a solenoid magnet with a length of 5.2 m and diameter 2.5 m, which generates a 2 T magnetic field.

3.2.3.1 Silicon Pixel Detector

In the barrel region, the silicon pixel detector[41, 43] consists of three concentrically-arranged silicon-pixel layers, at distances of 50.5 mm, 88.5 mm, and 122.5 mm from the beam pipe. In each endcap region, silicon-pixel detectors are located on disks perpendicular to the beam axis, at distances of 495 mm, 580 mm, and 650 mm from the nominal interaction point. The pixel layers are segmented in R-ϕ (where

R-ϕ is a plane defined with R as the radial distance from the centre of the detector) and z, and arranged in such a way that tracks typically cross three pixel layers while traversing the ID. Coverage is provided in the range $|\eta| < 2.5$. In total, 1744 identical pixel sensors are used, each with dimensions of 19 mm × 63 mm and 46080 readout channels, giving a total of approximately 80 million readout channels. The pixel sensors provide a spatial resolution of around 10 µm in the transverse direction, and 115 µm longitudinally.

3.2.3.2 Semiconductor Tracker

Outside the pixel detector lies the semiconductor tracker (SCT)[41, 43]. The SCT is built up from four double-sided barrel layers of silicon microstrip detectors, plus nine 'wheels' in each endcap region. Each individual silicon detector in the SCT barrel measures 6.36 mm × 6.40 mm, and consists of 768 readout strips of width 80 µm. In each barrel layer, one set of strips is aligned parallel to the beam direction, and the other at a small (40 mrad) stereo-angle, allowing for measurement of z position. The SCT wheels use sensors which are not of constant width, but have constant azimuthal angle coverage along their length, and an average pitch of approximately 80 mm. The wheels contain double-layer strips, and the two layers of each wheel are aligned with a small stereo angle to allow for measurement of R. In total, the SCT sensors cover an area of 61 m^2, with approximately 6.2 million readout channels. It provides a spatial resolution of 16 µm in the R-ϕ plane and 580 µm along the z axis, with coverage of the range $|\eta| < 2.5$. Tracks within the SCT can be distinguished if they are separated by more than around 200 µm.

3.2.3.3 Transition Radiation Tracker

The outer layer of the ID is the Transition Radiation Tracker[41, 43] (TRT). The basic elements of the TRT are polyimide straw drift tubes with a diameter of

4 mm. The centre of each tube contains a 31 µm wire anode, made from gold-plated tungsten and supported by end-plugs at each end of the straw tube. The tubes are filled with a gas mixture of 70% Xe, 27% CO_2, and 3% O_2, at a pressure of 5–10 mbar. Straws within the barrel region are positioned in 73 layers aligned parallel to the beam direction with a length of 144 cm, and are split into two halves at $\eta = 0$. The TRT endcaps contain 160 layers of 37 cm long tubes are arranged radially around the beam axis. In total, the TRT has approximately 351,000 readout channels, which provide coverage of the pseudorapidity range $|\eta| < 2.0$. The TRT provides lower spatial resolution than the pixel detector and SCT, but the large number of hits (an average of 36 per track) allow for robust pattern recognition and momentum measurement.

3.2.4 Calorimetry

The ATLAS calorimeters are located outside the ID, and can be broken down into three subdetectors:

Electromagnetic Calorimeter (*ECAL*)

for detection and reconstruction of electrons and photons, and precise energy measurement,

Hadronic Calorimeter (*HCAL*)

for detection and energy measurement of hadrons and jets,

Forward Calorimeter (*FCAL*)

which provides both EM and hadronic calorimetry in the forward region.

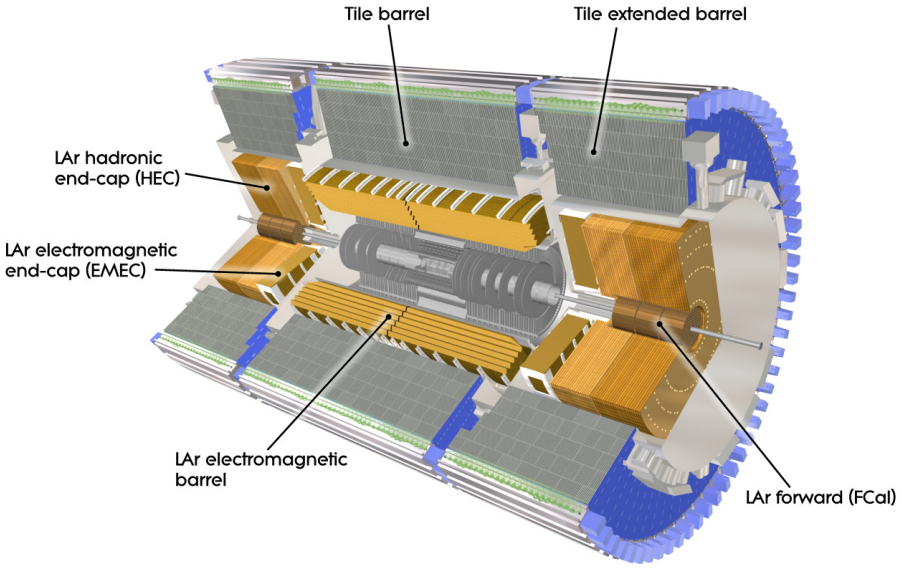

FIGURE 3.4: A computer generated image [42] of the ATLAS calorimetry.

3.2.4.1 The ATLAS Electromagnetic Calorimeter

The ATLAS electromagnetic calorimeter[41, 44–46] is designed to measure the energy of electromagnetically-interacting particles. It is a sampling detector, consisting of many layers, alternately of a dense absorber material and a less-dense active medium. In the case of the ATLAS electromagnetic calorimeter, the absorber material is lead, and the active medium liquid argon (for this reason it is also sometimes known as the *liquid argon calorimeter*). The interaction of charged particles with the lead of the calorimeter results in electromagnetic showering, a process of repeated bremsstrahlung and material interaction (at the energies targeted by the ATLAS electromagnetic calorimeter, this is predominantly electron-positron pair production) causing the build up of many charged particles which ionise the argon. Electrodes are located within the active medium and kept at high voltage, while the absorber material is grounded, producing an electric field within the detector. The ionised argon and the electrons drift under the influence of this field, producing a signal which can be detected on the electrodes.

The barrel section of the EM calorimeter covers the central region $|\eta| < 1.475$. Its

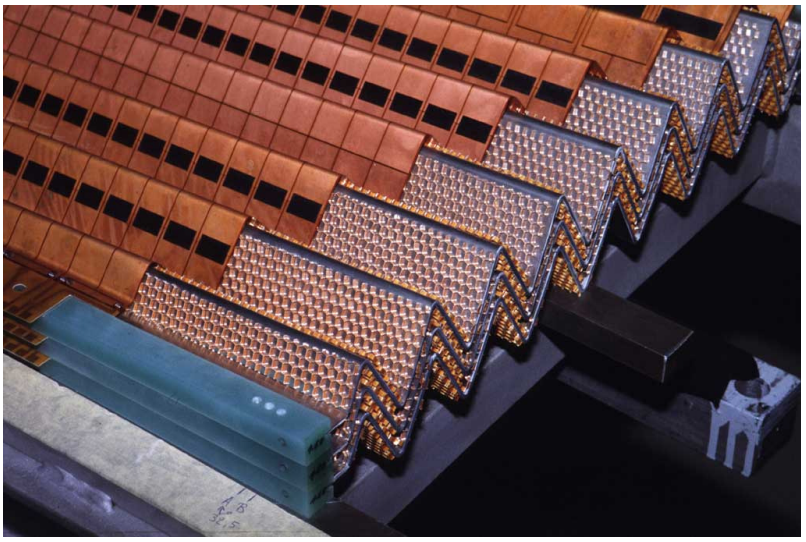

FIGURE 3.5: A section of the ATLAS electromagnetic calorimeter during construction, the so-called accordion geometry can be seen[42].

accordion geometry (see figure 3.5) allows the calorimeter to provide complete ϕ coverage, with no azimuthal cracks. Structurally, the barrel is made up of two half-barrels, separated by a gap of approximately 4 mm, each with a length of 3.2 m and an outer radius of 2 m. Two end-caps provide electromagnetic calorimetry outside the barrel region. The calorimeter cells are projective in η, effectively pointing towards the nominal interaction point through the full η coverage of the calorimeter.

The barrel of the electromagnetic calorimeter is split into three layers, or samplings, with varying η and ϕ resolutions. The first layer of the calorimeter is built from strip cells which are broad in ϕ but provide very fine resolution in η. This fine η-resolution is helpful in the determination of the p_{T} of incoming particles, and in γ/π^0 separation. The second layer consists of almost square cells, providing less η resolution but finer ϕ granularity than in the first layer. Electromagnetic particles deposit the majority of their energy in this layer, and the distribution of a shower's energy in this layer is heavily used in identification algorithms for these particles. The third and final layer, which typically collects only the tail of an EM shower, is more coarsely segmented in η. Figure 3.6 illustrates the cell sizes used within the various layers of the barrel region of the electromagnetic calorimeter.

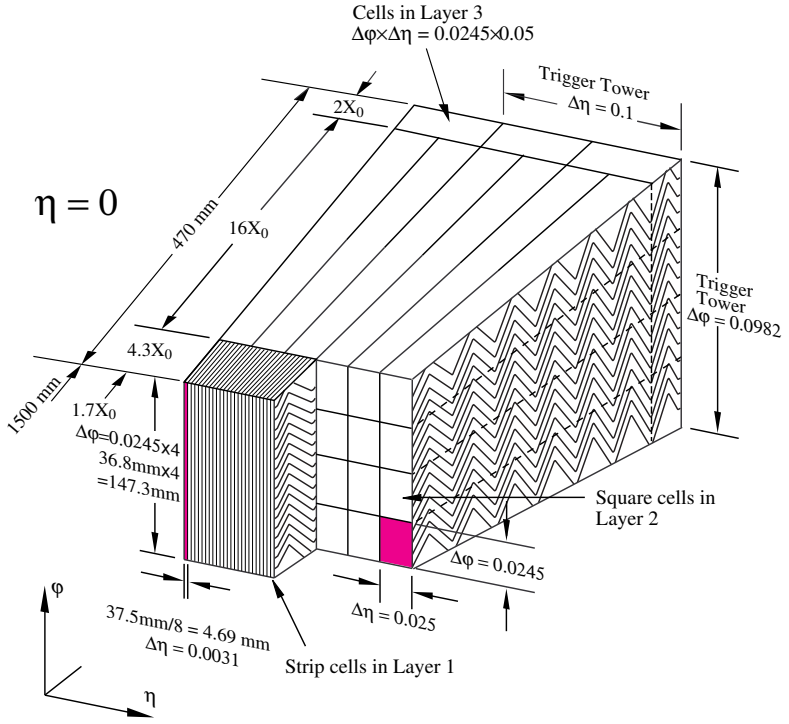

FIGURE 3.6: A sketch showing how the dimensions of cells in the barrel region vary between the different layers of the ATLAS electromagnetic calorimeter.

In the region $|\eta| < 1.8$, an additional *presampler* (*PS*) layer is also installed in front of the first layer of the electromagnetic calorimeter barrel. This extra layer consists solely of active LAr. The PS is used to correct for energy lost by electrons and photons before reaching the calorimeter. Within the barrel region ($|\eta| < 1.475$), the PS has a depth of 1.1 cm, in the end-cap ($1.475 < |\eta| < 1.8$) this is reduced to 0.5 cm.

The two EM calorimeter end-caps cover the region $1.375 < |\eta| < 3.2$. The end-caps have an accordion geometry similar to that in the barrel, to ensure full ϕ coverage. Each wheel consists of an inner wheel (which covers the high-$|\eta|$ range $2.5 < |\eta| < 3.2$) and an outer wheel ($1.375 < |\eta| < 2.5$). In the *precision region* ($1.5 < |\eta| < 2.5$), the outer wheels have three samplings. The inner wheels and the outer regions of the outer wheel have only two samplings. The cell sizes of the wheels are varied as a function of both sampling and pseudorapidity. Within the precision region, the layers are segmented similarly to the barrel. The first layer consists of strips providing high η granularity, the middle layer contains projective

	Barrel		**End-cap**	
	Granularity in $\Delta\eta \times \Delta\phi$ versus $\lvert\eta\rvert$			
Presampler	0.025×0.1	$\lvert\eta\rvert < 1.52$	0.025×0.1	$1.5 < \lvert\eta\rvert < 1.8$
Layer 1	0.025×0.1	$\lvert\eta\rvert < 1.4$	0.05×0.1	$1.375 < \lvert\eta\rvert < 1.425$
	0.025×0.025	$1.4 < \lvert\eta\rvert < 1.475$	0.025×0.1	$1.425 < \lvert\eta\rvert < 1.5$
			0.025×0.1	$1.5 < \lvert\eta\rvert < 2.5$
			0.1×0.1	$2.5 < \lvert\eta\rvert < 3.2$
Layer 2	0.025×0.025	$\lvert\eta\rvert < 1.4$	0.05×0.025	$1.375 < \lvert\eta\rvert < 1.425$
	0.075×0.025	$1.4 < \lvert\eta\rvert < 1.475$	0.025×0.025	$1.425 < \lvert\eta\rvert < 2.5$
			0.1×0.1	$2.5 < \lvert\eta\rvert < 3.2$
Layer 3	0.050×0.025	$\lvert\eta\rvert < 1.35$	0.05×0.025	$1.5 < \lvert\eta\rvert < 2.5$
	Total readout channels			
Presampler	7808		1536	
ATLAS electromagnetic calorimeter	101760		62208	

TABLE 3.2: Cell sizes (in $\Delta\eta \times \Delta\phi$) in each layer of the ATLAS electromagnetic calorimeter (including presampler) as a function of $|\eta|$ in both barrel and end-cap regions. The total number of readout channels are also shown.

cells with the same dimensions as in the barrel, and the rear layer is twice as coarse in $|\eta$ as the second layer. The outer regions of the outer wheel ($|\eta| < 1.5$) and the inner wheel ($2.5 < |\eta| < 3.2$) are made up of only two layers, with coarser transverse granularity than in the precision region. The cell geometries of all layers in the barrel and end-cap (including presampler) are summarised in table 3.2. The ATLAS electromagnetic calorimeter provides energy measurement with a resolution of: $\frac{\sigma_E}{E} = \frac{10\%}{\sqrt{E}} \oplus 0.7\%$

3.2.4.2 The ATLAS Hadronic calorimeter

The ATLAS Hadronic Calorimeter [47, 48] consists of two main components, using different technologies for the barrel and end-cap regions. Hadronic calorimetry in the barrel region ($|\eta| < 1.7$) is provided by the Tile Calorimeter, a sampling calorimeter which uses steel as the absorber material and scintillating tiles as the

active material. The Tile Calorimeter can be further split into *barrel* (5.8 m long, covering the range $|\eta| < 1.0$) and *extended barrel* (2.6 m long, covering $0.8 < |\eta| < 1.7$). The Tile Calorimeter is split longitudinally into three layers, and azimuthally into 64 modules. In the end-cap regions ($1.5 < |\eta| < 3.2$), hadronic calorimetry is provided by the Hadronic End-cap Calorimeters (*HEC*), which use copper as the absorber material and liquid argon as the active medium. The HEC is made up of two independent wheels per end-cap. They are positioned behind the end-caps of the ATLAS electromagnetic calorimeter and share their end-cap cryostats. The energy resolution of the ATLAS hadronic calorimeter is $\frac{\sigma_E}{E} = \frac{50\%}{\sqrt{E}} \oplus 3\%$

3.2.4.3 The ATLAS Forward Calorimeter

The final component of the ATLAS calorimetry system is the ATLAS Forward Calorimeter (*FCAL*) [41, 47, 49], located within the same cryostats used for the ECAL and HCAL end-caps, which provides both electromagnetic and hadronic calorimetry in the very forward region ($3.1 < |\eta| < 4.9$). Like the ECAL and HEC, the active material in the FCAl is liquid argon. The absorber material in the first of its three layers copper, and this layer is mostly dedicated to electromagnetic measurements. The two outer layers use tungsten as their absorber material, and are devoted predominantly to hadronic measurements. The FCAL's position at high pseudorapidity, 4.7 m from the interaction point, means it is exposed to high particle flux. As such, the design of the FCAL modules differs from that used in the other liquid argon calorimeters in ATLAS. Rather than alternating flat layers of absorber and active material, the structure of the FCAL is based on rods of active material within a block of the absorber material. The FCAL electrodes take the form of small-diameter rods, located centrally in tubes oriented parallel to the beam axis. The liquid argon gaps are smaller than the 2 mm gaps used in the ECAL barrel (approximately an eight of that size in the first layer, increasing by about 50% in each of the two subsequent layers), reducing ion build-up which

would otherwise distort the electric field within the detector sufficiently to degrade the signal.

3.2.5 The ATLAS Muon Spectrometer

The outermost layer of the ATLAS detector is the muon spectrometer[41, 50, 51], designed to detect and measure the momentum of charged particles passing through the barrel and end-cap calorimeters within the pseudorapidity range $|\eta| < 2.7$. The working principle is based on the magnetic deflection of muon tracks by superconducting toroid magnets, instrumented with high-precision tracking chambers. Within the region $|\eta| < 1.4$, magnetic bending is provided by the large barrel toroid magnet. Smaller end-cap magnets provide the magnetic bending in the $1.6 < |\eta| < 2.7$ range, while bending in the *transition region* $1.4 < |\eta| < 1.6$ comes from a combination of the barrel and end-cap fields. This configuration of magnets provides a magnetic field which remains mostly orthogonal to muon trajectories, and minimises the resolution degradation from multiple scattering.

The muon spectrometer system consists of two different chamber types (precision tracking chambers and fast trigger chambers) arranged in eight azimuthally symmetric octants. Each octant is divided into two sectors, one larger than the other, with overlapping coverage in ϕ. The ϕ overlap reduces gaps in detector coverage, and enables relative alignment of the sectors with tracks recorded in both. Within the barrel, chambers are arranged in three concentric shells, approximately 5 m, 7.5 m, and 10 m from the beam axis. In the end-cap regions, muon chambers are arranged in wheels perpendicular to the z-axis, located at around $|z| = 7.4$ m, 10.8 m, 14 m, and 21.5 m at each end of the detector. A small gap in chamber coverage exists around $\eta = 0$, allowing for services to the solenoid magnet, calorimeters, and inner detector.

Two varieties of precision tracking chamber are in use. Monitored Drift Tube chambers (*MDT*s) consist of three to eight layers of drift tubes, and provide a typical resolution of about 35 µm per chamber. They provide coverage of the muon system's whole pseudorapidity range $|\eta| < 2.7$, except for in the first end-cap layer where they cover only the region $|\eta| < 2.0$. In the forward region $2.0 < |\eta| < 2.7$ the first end-cap uses Cathode Strip Chambers (*CSC*s), due to their better time resolution and higher rate capability. The CSCs are multi-wire proportional chambers, with cathode planes segmented into strips in orthogonal directions. They provide resolution of 40 µm in the bending plane and 5 mm in the transverse plane.

Fast trigger chambers provide fast information on muon tracks traversing the ATLAS detector, across the range $|\eta| < 2.4$ and with full ϕ coverage. Two technologies are used. Within the barrel ($|\eta| < 1.05$), Resistive Plate Chambers (*RPC*s) are used, which provide good spatial and time resolution. They have no wires, simplifying construction. Within the end-cap ($1.05 < |\eta| < 2.4$), Thin Gap Chambers (*TGC*s) are used. TGCs provide good time resolution and a higher rate capability than RPCs.

3.2.6 The ATLAS Trigger System

The 40 MHz bunch-crossing rate provided by the LHC results in far more collisions than it is practical to store. It is therefore important to have an effective trigger system which efficiently selects interesting events to be recorded and stored for analysis. The ATLAS trigger system consists of three levels, each of which uses input from the detector and previous levels of the trigger system to progressively refine the selection of events to be written to disk. The first stage of the ATLAS trigger system is known as the *Level 1 trigger* (*L1*). Events which pass the L1

trigger continue to the *High-Level Trigger* system (*HLT*), which consists of two components: the *Level 2* trigger (*L2*) and the *Event Filter* (*EF*).

The L1 trigger has access to reduced-granularity information from the ATLAS calorimeters and muon chambers, and searches for events with high-p_{T}muons, electrons, photons, jets, and τ-leptons undergoing hadronic decays. Events with large missing and total transverse energy are also identified. *Regions of Interest* (*RoI*) are defined in regions of the detector surrounding any possible trigger objects identified by the L1 trigger. The maximum acceptance rate of the L1 trigger is around 75 kHz. Decisions must reach the front-end electronics within a time period of 2.5 µs.

L2 trigger has access to event information using the full granularity of the detector within each event's RoI, including information from the Inner Detector (which is not available at L1). The L2 trigger uses a sequential selection strategy[52], in which a number of steps are performed sequentially. At each step, only the data required to make the decision at that step is acquired and analysed. This selection strategy allows for some events to be rejected before reading the full event data, reducing bandwidth requirements. The L2 trigger reduces the accepted event rate to a maximum of around 3.5 kHz, with a latency on the order of tens of milliseconds. Events passing the L2 trigger proceed to the EF. Full ATLAS reconstruction algorithms are applied to the objects seeded by the L1 and L2 triggers, and the accepted event rate is further reduced to around 200 Hz.

Chapter 4

ATLAS Data and Reconstruction

4.1 ATLAS Data

The ATLAS detector measured its first proton-proton collisions in 2009, at the relatively low energy of 450 GeV per beam. The beam energy was gradually increased to 3.5 TeV per beam for the 2010 data-taking period, in which an integrated luminosity of approximately $47\,\text{pb}^{-1}$ was measured. A further $5.5\,\text{fb}^{-1}$ of data was taken at the same 3.5 TeV per beam energy in the 2011 data-taking period. The work in this thesis is based upon analysis of proton-proton collision data taken by the ATLAS detector during the 2012 data-taking period, during which the energy was increased to 4 TeV per beam.

4.1.1 The 2012 Dataset

Throughout the 2012 data-taking period, the LHC operated at a centre-of-mass energy $\sqrt{s} = 8\,\text{TeV}$ (4 TeV per beam), with a bunch spacing of 50 ns. In total,

the LHC delivered an integrated luminosity of $22.8\,\text{fb}^{-1}$ during the 2012 data-taking period. Of this, $21.3\,\text{fb}^{-1}$ was recorded by the detector. ATLAS data is organised into units known as *lumi blocks*, each covering the data taken over a short period of time so as to minimise the amount of data which is discarded if a particular block is unsuitable for physics usage (e.g. due to detector components not functioning correctly, or any other issue which may cause problems with the data collected). After removing these unsuitable blocks, a total of $20.3\,\text{fb}^{-1}$ usable data was collected. This luminosity value was extracted from the proton-proton scattering cross-section in the forward direction. The uncertainty on the integrated luminosity is $\pm 2.8\%$, as derived from a preliminary calibration of the luminosity scale derived from beam-separation scans[53] performed in November 2012.

The instantaneous luminosity of the LHC during 2012 operation reached a peak of $7.73 \times 10^{33}\,\text{cm}^{-2}\,\text{s}^{-1}$, close to the nominal design luminosity of $10^{34}\,\text{cm}^{-2}\,\text{s}^{-1}$. Due to the high luminosity of the LHC beams, it is common that when an event is recorded, there are many soft interactions in addition to the hard interaction by which the trigger is fired. These additional interactions are referred to as pile-up, and come in two varieties:

In-time pile-up,

resulting from additional interactions within the same bunch crossing as the interaction which fired the trigger.

Out-of-time pile-up,

resulting from interactions occurring in other bunch crossings than the hard interaction.

The amount of pile-up is characterised by the variable $\langle\mu\rangle$, which denotes the average number of pileup events overlaid above the hard interaction. The presence of large numbers of pile-up events can introduce complications in reconstructing

physics objects from an interaction. In the 2012 dataset, the number of interactions per crossing reached a maximum of around 40, and $\langle\mu\rangle$ for the whole 2012 dataset was 20.7[54].

4.2 Reconstruction

Accurate reconstruction of physics objects in the ATLAS detector is crucial for physics studies. This section will discuss the methods used to reconstruct electron and photon candidates, the determination of *isolation*, and calibration of the detector for energy measurements.

The typical signature of an electron traversing the ATLAS detector includes a curved track through the ATLAS Inner Detector, and an electromagnetic shower in the ATLAS ECAL. A photon, in the simplest case, leaves no track in the Inner Detector, but will interact with the ECAL in a manner very similar to electrons. Additionally, photons may interact with material in the detector before reaching the ECAL, leading to production of an electron pair $\gamma \rightarrow e^+e^-$. In this case, the electrons will leave tracks within the Inner Detector before showering in the ECAL. As the signatures of electrons and photons (especially converted photons) are rather similar, a process is used for reconstruction of both electrons and photons. First, *preclusters* are sought, and tracks reconstructed. Final clusters are built around the identified preclusters, their size dependent upon the location in the detector and the type of particle (determined by track information).

4.2.1 Clustering Algorithm

Reconstruction of electrons and photons within the central calorimeter region ($|\eta| < 2.47$) starts with a search for energy clusters in the calorimeter[55–57]. The calorimeter is divided into a grid of $N_\eta \times N_\phi = 200 \times 256$ *towers*, each sized

($\Delta\eta \times \Delta\phi = 0.025 \times 0.025$), corresponding to the granularity of the middle layer of the ATLAS ECAL. Energy deposits from all layers of the calorimeter are summed to determine the tower energy, with the energy in cells covering multiple towers distributed evenly between those towers. A sliding window algorithm then operates, with a window size of $\eta \times \phi = 3 \times 5$ towers, selecting so-called *cluster seeds* or *preclusters* where the total transverse energy within the window is 2.5 GeV or more. The precluster position is defined as the energy-weighted barycentre in η and ϕ of the cells contained within the window. A duplicate removal algorithm operates where multiple preclusters are selected within any 2×2 tower region, keeping only the precluster with the largest transverse energy. Track information is then used to classify the preclusters as electrons, converted photons, or unconverted photons, and build the appropriate cluster type.

4.2.2 Track Reconstruction

The standard track reconstruction method[58, 59] in ATLAS first operates an *inside-out* tracking algorithm. in which tracks are built initially from hits in the ATLAS silicon pixel and strip detectors. Track *seeds* are produced from three-dimensional space-points corresponding to the hit locations. Track seeds provide sufficient directional information to predict regions in which further hits from the same track are likely. If further hits are found in those regions, track fitting proceeds from the seeds with a Kalman filter[60, 61] algorithm, iteratively adding hits to the track and refitting after each hit addition.

This typically produces a very large number of track candidates, many of which are incomplete, share hits with other track candidates, or are not true tracks (i.e. their hits do not result from a single particle). The track candidates are ranked according to a scoring strategy[62] which assigns a score to each track

candidate. The score is affected positively or negatively by a number of characteristics, weighted differently for different detector components. After each track candidate is scored, shared hits are assigned to one track candidate (typically that with the highest score), and the remaining track candidate(s) are refitted without it. This is an iterative procedure, with each refitted track candidate re-entering the set of track candidates to be evaluated. Track candidates which fall below a certain quality threshold are discarded and not processed further. The tracks remaining after quality cut and ambiguity resolution are then extended into the TRT. Tracks fitted within the Inner Detector are extrapolated, and additional hits sought within the TRT. At this stage, additional hits may be added to the hit collection corresponding to each track, but the Inner Detector track seed is not refitted or otherwise modified. The final fit, accounting for all hits associated to the track, is then performed by the ATLAS Global χ^2 Track Fitter[63].

Some tracks may not be identified by the inside-out tracking algorithm. A number of reasons exist which may cause this, such as ambiguous hits not successfully resolved, or substantial energy loss guiding the extrapolation of the track seed into the TRT in the wrong direction. A particularly relevant reason is that those tracks which come from secondary decay vertices (e.g. photon conversions) inside the Inner Detector may not have enough hits in the silicon detector to form a track seed in the silicon detectors. To detect these tracks, the inside-out algorithm is followed by an *outside-in* tracking algorithm. Track seeds for the outside-in algorithm are formed from track segments observed within the TRT which do not correspond to any of the tracks previously identified. The segments are identified via pattern recognition. As the TRT drift tube measurements do not provide measurement of position along the straw directions, the pattern recognition must be performed in projective planes. The planes chosen as most suitable are r-ϕ in the TRT barrel region, and r-z in the TRT end-cap region. In these planes, a track segment originating from near the primary interaction point will appear as

an approximately straight line when projected into the chosen plane and so may be relatively easily recognised. These segments may then be propagated back into the pixel and strip detectors, by searching for hits within narrow wedges of the silicon pixel and strip detectors, corresponding to the r-ϕ or $r-z$ position of the TRT segment. In the case that further hits are found, the track is refined by the same Kalman filter technique as used in the inside-out algorithm.

4.2.3 Vertex Reconstruction

Once tracks are formed, the vertices from which they originate must be reconstructed. This process begins with an iterative vertex finding algorithm[64, 65] which is used to identify the primary vertices. Vertex seeds are taken from the z-position of reconstructed tracks, and a χ^2-based fit performed, with tracks weighted in according to their compatibility with the seed. Tracks displaced from existing seeds by more than 7σ are used to seed a new vertex, and the process repeats until there are no further vertex seeds found. The vertex whose associated tracks give the largest Σp_{T}^2 is typically assigned as the primary vertex, although a different method (described in section 6.6) is used in the $H \to \gamma\gamma$ analysis.

Reconstruction of photon conversion vertices is quite different from primary vertex reconstruction as it cannot be assumed that the vertex will be within the primary interaction region, and it is possible to apply additional constraints relating to masslessness of the converted photon. As such, they are reconstructed with a modified vertex-finding algorithm[66]. Conversion vertices can be identified at distances up to 800 mm from the IP (at larger distances, there track is unlikely to leave sufficient hits in any element of the detector for accurate reconstruction of the particle trajectory). Conversion vertices are classified depending on the number of tracks associated to them as single-track or double-track conversion vertices. Single-track conversion vertices typically occur at greater radial separation from

the IP. With only one reconstructed track, it is not possible to perform a full vertex fit, the conversion vertex is placed the locaion of the first measurement of the track. Single-track conversion vertices typically occur as a result of asymmetric conversions where one track has $p_{\mathrm{T}} < 0.5\,\mathrm{GeV}$ or from symmetric conversions which occur deep in the tracker, producing two high-p_{T} tracks which cannot be adequately separated from each other.

4.2.4 Classification as Electron or Photon Candidates

The reconstructed tracks are loosely matched to a cluster if they fulfill either of the following requirements:

- The difference between the cluster position and the track position extrapolated to the second layer of the calorimeter is:
  - not greater than 0.05 in η for tracks with silicon hits, and
  - not greater than 0.05 in ϕ if no deviations due to bremsstrahlung are expected, or 0.2 in ϕ if deviations due to bremsstrahlung are expected.
- The difference between the cluster position and the track position after rescaling the track's energy to that measured in the cluster is:
  - not geater than 0.05 in ϕ for tracks with silicon hits, and
  - not greater than 0.05 in ϕ where no deviations due to bremsstrahlung are expected, and not greater than 0.1 in ϕ where deviations due to bremsstrahlung are expected.

The second of these requirements is aimed at selecting low momentum tracks which may fail the first set of matching criteria due to significant losses from bremsstrahlung before reaching the calorimeter.

Reconstructed objects in which the cluster is not matched to any track are classified as unconverted photon candidates. Those with clusters matched to tracks originating from the interaction region are classified as as electron candidates. If the cluster is matched to tracks consistent with originating from a photon conversion, and a corresponding conversion vertex is also reconstructed, then the object is considered as a converted photon candidate. The matching of clusters to conversion vertices is dependent on the properties of the vertex.

Single-track conversion vertices

If the track associated to the vertex, when extrapolated to the second layer of the electromagnetic calorimeter, falls within a small η-ϕ window of the cluster centre in that layer then the conversion vertex is considered matched to that cluster.

Double-track conversion vertices

Criteria for double-track conversions depend upon the relative momenta of the tracks:

- If the track momenta differ by a factor of 4 or more, the original converted photon is reconstructed from the track parameters at the vertex, and a straight-line fit is performed from the conversion vertex to the second layer of the electromagnetic calorimeter. If the position within this layer is within a small η-ϕ window of the cluster centre in that layer, the conversion vertex is considered matched to that cluster.
- If the track momenta differ by a factor of less than 4, each track is individually extrapolated to the second layer of the electromagnetic calorimeter. If the extrapolated tracks are both matched to the same cluster, then the conversion vertex is also considered matched to that cluster.

In each of the above cases, the η-ϕ window used for matching tracks to clusters has dimensions of 0.05 on each side of the impact point in η and ϕ, extended to 0.1 in ϕ on the side where losses are expected due to bremsstrahlung.

4.2.5 Isolation

Isolation is a variable defined to quantify the activity surrounding a reconstructed object. This information can be useful for discriminating between electrons or photons (which typically have a *clean*, isolated detector signature) and backgrounds such as jets from light mesons (which are typically associated with a large amount of hadronic activity). Isolation may be measured in the Inner Detector (*track isolation*) and in the calorimeter (*calorimetric isolation*).

4.2.5.1 Track Isolation

Track isolation[67] for a given track is computed as the sum of p_{T} for all other tracks found within a cone of ΔR. In the case of double-track converted photons, the other track from the conversion is not considered. A typical choice of ΔR is 0.3, though some analyses use smaller or larger cones. To remove low quality tracks and tracks from pile-up events which may accompany the reconstruted object, the standard track isolation definition places the following requirements on tracks to be included in the calculation:

- $p_{\mathrm{T}} > 0.4\,\mathrm{GeV}$
- $|d_0| < 1.5\,\mathrm{mm}$
- $|z_0| < 1.0\,\mathrm{mm}$
- at least 7 hits in the silicon detector

- at least one b-layer hit
- tracks within $\Delta R \leq 0.1$ of the electron candidate must not be matched to a conversion vertex

where d_0 and z_0 are the transverse and longitudinal impact parameters. This prescription is altered for some analyses, including $H \to \gamma\gamma$ studies (the track isolation prescription used in $H \to \gamma\gamma$ will be described in section 6.6).

4.2.5.2 Calorimetric Isolation

The calorimetric isolation[68] of a cluster is computed by summing the transverse energies of all topological clusters[56] within a cone of some ΔR ($\Delta R = 0.4$ is a common choice, but other values may be used depending on the requirements of the study) around the cluster barycentre. Any topological clusters within the cone which have negative energy are not considered in the summation. The energy of cells within a $5 \times 7(\eta \times \phi)$ cell region is also excluded from the summation. To improve the pile-up robustness of the calorimeteric isolation variable, corrections are applied on an event-by-event basis to account for the ambient energy density within the calorimeter and for out-of-cluster energy leakage[69].

4.2.6 Energy Calibration for Electrons and Photons

As described in section 4.2.1, reconstruction of photons and electrons within the ATLAS detector starts with the identification of energy clusters within the calorimeter. A basic measurement of the deposited energy can be obtained simply and directly from the strength of the signal which is read out of the calorimeter cells. This method, however, does not account for effects such as energy loss in material before the calorimeter, or lateral and longitudinal leakage outside the

cluster. To make a more accurate measurement of particle energy, an in-depth calibration procedure[70] is required.

A multivariate analysis (*MVA*) method is used to link the electromagnetic clusters to the true electron or photon energy from MC samples, based on cluster properties and information from the ATLAS ID, taking advantage of the longitudinal segmentation of the electromagnetic calorimeter. This MVA calibration step is optimised separately for electrons, converted photons, and unconverted photons. For this process it is important that the simulation accurately models both the detector geometry and the interaction of particles with the material within the detector. The accuracy of the material distribution within the detector is ensured by measurements using the ratio of energy in the first layer of the EM calorimeter to energy in the second layer of the EM calorimeter.

Before this MVA calibration can be applied to data, it is necessary to implement corrections for differences in the response between different regions of the calorimeter. Another set of corrections are derived such that the scale of the energy responses of the various longitudinal layers of the calorimeter are equalised in data with respect to MC. With these corrections applied, the MVA calibration can be performed. The overall response is then calibrated so that the data agrees with the expectations from MC, using a large sample of $Z \to e^+e^-$ events. Per-electron scale factors are extracted, and are applied to electron and photon candidates from data. Corrections are then derived which can be applied to simulated data, so that it matches what is observed in real data. These scale factors derived from electrons are assumed to remain valid for photons.

Chapter 5

Photon Identification Efficiency Measurement

The typical signature of photons passing through the ATLAS detector was discussed in section 4.2. However, similar signatures may also be produced from other processes. A major source is QCD jets containing neutral hadrons such as π^0, which may decay into photon pairs and be reconstructed as photon candidates (often referred to as *fake photons*). The abundance of this and other backgrounds necessitates photon selection procedures designed to separate true photons from the jet background. In this section, a study is performed to evaluate the efficiency of these procedures.

5.1 Photon Identification

The algorithms used for photon identification in the ATLAS experiment rely on rectangular cuts on calorimetric variables which describe how the energy deposited in the electromagnetic shower is deposited. These variables are known as *shower*

shapes, can be broadly categorised into measuring hadronic leakage, measuring energy distribution in the middle layer of the ATLAS EM calorimeter, and measuring energy distribution in the strip layer of the ATLAS calorimeter. They are briefly described in table 5.1. A more detailed description can be found in references [71, 72]. Two levels of identification, *loose* and *tight*, are defined. The loose selection applies cuts only on the shower shapes R_η, w_{η_2}, and either R_{had} or R_{had_1}, depending on the pseudorapidity of the photon candidate. The tight selection applies stricter cuts on these shower shapes, and additionally applies further cuts to other shower shapes, designed to have a high background rejection rate while retaining high signal yield. The loose selection applies the same cuts to both converted and unconverted photons, while the tight selection is optimised separately for converted and unconverted photons.

Throughout this study, all efficiencies and sources of uncertainty are studied in bins of p_{T} and $|\eta|$. The p_{T} binning covers the entire range from 30 GeV to 100 GeV. All measurements in the study are presented in 4 $|\eta|$ bins over the range $0 < |\eta| < 2.37$, excluding the region $1.37 < |\eta| < 1.52$. During the analysis, the samples is split into 8 $|\eta|$ bins covering the same range, which are then combined into the 4 bins presented here. The binning is motivated by changes in detector geometry. The excluded $1.37 < |\eta| < 1.52$ region corresponds to the so-called crack region between the barrel and end-cap sections of the electromagnetic calorimeter.

5.2 Photon ID Efficiency

The tight identification (ID) efficiency is an estimate of the fraction of reconstructed photons which will pass the tight photon ID criteria. It is defined as the efficiency for a reconstructed true photon (i.e. photon candidates reconstructed from calorimeter energy deposits left by actual photons) with calorimeter isolation (as defined in section 4.2.5) below 4 GeV to pass the tight photon ID criteria

Category	Description	Shower Shape	Loose	Tight
Hadronic leakage	Ratio of the E_T in the first sampling of the hadronic calorimeter to the E_T of the EM cluster (used over the ranges $\|\eta\| < 0.8$ and $\|\eta\| > 1.37$)	R_{had_1}	✓	✓
	Ratio of the E_T in all layers of the hadronic calorimeter to the E_T of the EM cluster (used over the range $0.8 < \|\eta\| < 1.37$)	R_{had}	✓	✓
Middle layer	The ratio between the sum $E^{S2}_{3\times7}$ of the cell energies in a 3×7 rectangle (measured in cell units in $\eta\times\phi$), and the sum $E^{S2}_{7\times7}$ of the cell energies in a 7×7 rectangle, both centered around the cluster seed	R_η	✓	✓
	Lateral width of the shower in the η direction	w_{η_2}	✓	✓
	Ratio between the sum $E^{S2}_{3\times3}$ of the cell energies contained in a 3×3 rectangle (measured in cell units in $\eta\times\phi$), and the sum $E^{S2}_{3\times7}$ of the cell energies in a 3×7 rectangle, both centered around the cluster seed	R_ϕ		✓
Strip layer	Lateral shower width for maximum strip and two neighbours	$w_{s\,3}$		✓
	Total lateral shower width	$w_{s\,\mathrm{tot}}$		✓
	Fraction of energy outside core of three central strips but within seven strips	F_{side}		✓
	Difference between the energy of the strip associated with the second maximum in the strip layer, and the energy reconstructed in the strip with the minimal value found between the first and second maxima	ΔE_s		✓
	Ratio of the energy difference associated with the largest and second largest energy deposits over the sum of these energies	E_{ratio}		✓

TABLE 5.1: Discriminating variables used in photon identification, with indication of which cuts are used in the loose and tight photon identification prescriptions. E^{S2} denotes energy deposited in the second layer of the calorimeter.

$\|\eta\|$ bin number	1	2	3	4	5	6	7	8
lower boundary	0	0.1	0.6	0.8	1.15	1.52	1.81	2.01
upper boundary	0.1	0.6	0.8	1.15	1.37	1.81	2.01	2.37

TABLE 5.2: The upper and lower boundaries of the 8 $|\eta|$ bins in which the study is performed. The crack region ($1.37 < |\eta| < 1.52$) is excluded.

$\|\eta\|$ bin number	1	2	3	4
lower boundary	0	0.6	1.52	1.81
upper boundary	0.6	1.37	1.81	2.37

TABLE 5.3: The upper and lower boundaries of the 4 $|\eta|$ bins used for presentation. The crack region ($1.37 < |\eta| < 1.52$) is excluded.

(tight ID) as laid out in equation (5.1). The efficiency measurement is binned two-dimensionally in pseudorapidity and transverse energy.

$$\varepsilon_{\text{tight}} \equiv \frac{N^{\gamma}(E^{\text{iso}}_{\text{T,reco}} < 4 \text{ GeV}, \text{tight ID})}{N^{\gamma}(E^{\text{iso}}_{\text{T,reco}} < 4 \text{ GeV})} \tag{5.1}$$

5.3 Electron Extrapolation

Obtaining a pure photon sample from data is usually difficult, with the exception of low energy photons which can be obtained from $Z \to \ell^+\ell^-\gamma$ ($\ell = e, \mu$) processes. It is however possible to extract a high-purity sample of electrons with a *tag and probe* selection (see section 5.4) designed to select electrons from $Z \to e^+e^-$ events. By taking advantage of similarities between the electromagnetic showers produced in the EM calorimeter by electrons and photons, it is possible to use this sample of electrons to make an estimation of photon ID efficiency in the ATLAS detector.

Section 5.4 of this thesis describes the $Z \to e^+e^-$ selection which is used to extract the electron sample from data. Section 5.5 describes the *Smirnov transformation*

method of extrapolation from electrons to photons. While there are similarities between the showers left by electrons and photons, differences exist and are an important source of systematic uncertainty for photon ID efficiency measurements using electron extrapolation. Several Monte Carlo (MC) samples are used in this analysis, using two detector geometries. Samples with *nominal* geometry reflect the best estimation of the real geometry of the detector. The primary origin of uncertainty regarding the detector geometry relates to how dead material (resulting primarily from cabling and cooling services) is distributed within the detector volume. This material distribution has been improved by observation of the ratio of energies deposited in the first and second layers of the electromagnetic calorimeter[70].

The *distorted* geometry samples are simulated with some material variations, reflecting the uncertainty on the amount and location of material contained within the Inner Detector. These distorted samples are used to evaluate the systematic uncertainty on the photon ID efficiency measurement resulting from differences between data and MC, including both geometry-related and detector-modelling effects. Another source of systematic uncertainty is the difference between showers in data and MC samples. These sources of systematic uncertainty are examined in section 5.6. Section 5.7 presents the results in the form of the estimated photon ID efficiency. Comparisons are provided to the nominal MC sample, and to MC samples with *fudge factors* applied. These so-called fudge factors are shifts applied to the shower shapes in the MC samples, the values of which are derived from differences between data and MC. They act to produce a tuned MC sample which resembles data measurements more closely than the nominal MC sample does.

Data Set	Process	σ [pb]	Filter type	Filter threshold [GeV]	Filter efficiency	Events in tuples	Equivalent luminosity [pb^{-1}]	Offline min photon E_{T} cut [GeV]
129170	Direct Photon	1.235E+9	1 prompt γ	17	2.34E-4	3E+6	1.03E+1	20
129171	Direct Photon	5.876E+7	1 prompt γ	35	4.02E-4	3E+6	1.27E+2	45
129172	Direct Photon	3.425E+6	1 prompt γ	70	5.70E-4	3E+6	1.53E+3	85
147806	$Z \to e^+e^-$	1.110E+3				1E+7	9.01E+3	–
129170	Direct Photon	1.235E+9	1 prompt γ	17	2.34E-4	1E+6	3.46	20
129171	Direct Photon	5.876E+7	1 prompt γ	35	4.02E-4	1E+6	4.23E+1	45
129172	Direct Photon	3.425E+6	1 prompt γ	70	5.70E-4	1E+6	5.12E+2	85
147806	$Z \to e^+e^-$	1.110E+3				5E+6	4.50E+6	–

TABLE 5.4: A summary of the MC samples used in the measurements. All samples were generated with Pythia8. Samples in the upper half of the table are those with nominal geometry, those in the lower half of the table are produced with the distorted geometry used for systematic studies. The *Direct Photon* samples include QCD 2→2, γq, and γg processes.

5.4 Electron Selection

To allow for extrapolation from electrons to photons to be truly representative, it is important that the shower shapes of the selected electrons are unbiased. To achieve this, a *tag and probe* selection method is used, in which strict cuts are placed on events and on the *tag* electron within each event. These strict cuts allow for a high confidence that the selected event really is a $Z \to e^+e^-$ decay, and that the *probe* objects are in fact electrons, without introducing a bias to the shower shapes of the selected probes. An isolation cut ($E_{\mathrm{T}} < 4\,\mathrm{GeV}$ within a cone of $\Delta R < 0.4$) is also applied, as the extrapolation is performed to photons with similar isolation criteria. The full $Z \to e^+e^-$ selection used in the study is shown below:

- The invariant mass of the electron candidate pair must be in the range $80\,\mathrm{GeV} < m_{ee} < 120\,\mathrm{GeV}$.
- The two electron candidates are required to have opposite charge.

- Both electron candidates must each have $p_{\mathrm{T}} > 25\,\mathrm{GeV}$ and fall within the pseudorapidity range $0 < |\eta| < 2.37$, excluding the crack region between $1.37 < |\eta| < 1.52$.
- Both electron candidates must pass the tracking criteria from the tight electron selection: at least 7 silicon hits and 1 pixel hit.
- Both electron candidates must pass the E_{T} isolation requirement.
- The tag electron must pass the trigger requirement `EF_e24vhi_medium1`, and must pass the tight electron identification requirements. Trigger matching is performed within a cone $\Delta R < 0.15$.
- There must not be any jet with $p_{\mathrm{T}} > 20\,\mathrm{GeV}$ within a cone of $\Delta R < 0.4$ of the probe electron.

The `EF_e24vhi_medium1` trigger which is used in the event selection process identifies events containing at least one reconstructed electron candidate with p_{T} of at least 24 GeV which passes hadronic core isolation and track isolation. Hadronic core isolation is defined as the longitudinal isolation in a 2×2 tower region behind the core of the reconstructed electromagnetic cluster, and is applied at the L1 trigger stage with a threshold of 1 GeV. The track isolation requirement is applied at the EF trigger stage, with an energy-dependent threshold $p_{\mathrm{T}}^{\mathrm{cone}\ 20}/p_{\mathrm{T}} = 0.1$, where $p_{\mathrm{T}}^{\mathrm{cone}\ 20}$ denotes the total transverse momentum within a cone $\delta R = 0.2$ around the track.

In the case of the MC samples, reweighting is applied based on μ, the average number of interactions per bunch crossing, so as to match the distribution in MC to that in the data sample. The result of this reweighting on the $Z \to e^+e^-$ MC sample is shown, with a comparison to the data distribution, in figure 5.1 Similar comparisons of the reweighted MC sample's p_{T} and $|\eta|$ distributions to those in data are shown in figures 5.2 and 5.3 respectively.

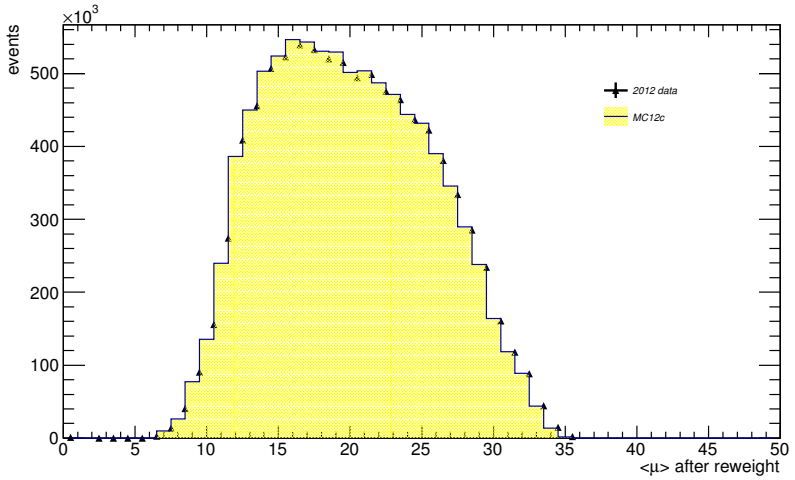

FIGURE 5.1: Average interactions per bunch crossing associated to the event sample in data (data points) and in pure $Z \to e^+e^-$ MC (yellow filled area).

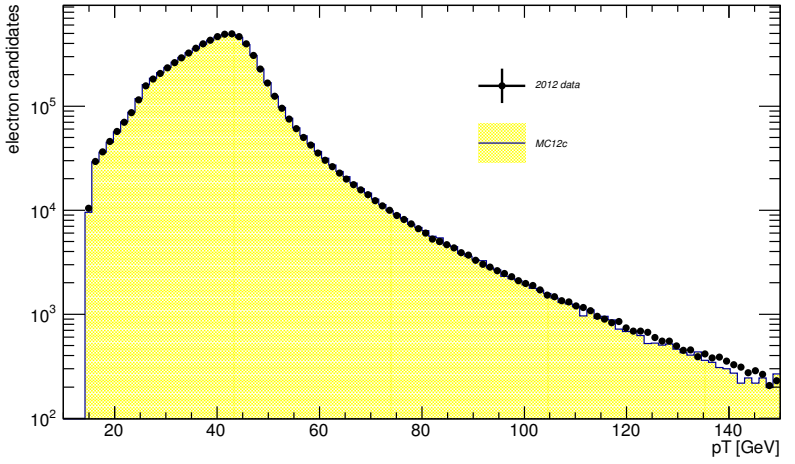

FIGURE 5.2: A comparison of the p_{T} distribution of selected probes in the MC sample with that observed in data.

5.4.1 BACKGROUND

As the shower shapes of particles from background events will differ from those of electrons selected from real $Z \to e^+e^-$ decays, the presence of such background particles in the selected electron sample may introduce a bias into the efficiency measurement. For this reason it is important to evaluate the level of background contamination in the selected sample and how it affects the identification efficiency

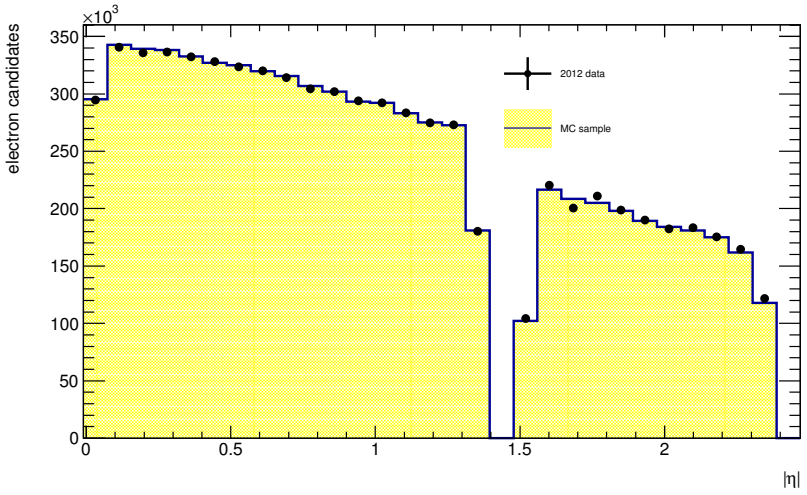

FIGURE 5.3: A comparison of the $|\eta|$ distribution of selected probes in the MC sample with that observed in data.

measurement. A study is performed to evaluate this, based on methods used in previous ATLAS studies in the $Z \to e^+e^-$ decay channel[73].

The study discriminates between the signal and background components of the selected sample by inspecting the invariant mass, m_{ee}, of electron pairs. A template is derived which describes the m_{ee} distribution of background events. This template is normalised to the m_{ee} distribution in a background dominated region of the sample passing the signal selection requirements. Subtracting the normalised template from the signal selection allows for an estimate of the level of background contamination in the selected electron sample.

The template selection is largely the same as the signal selection, with exceptions described below:

- The probe electron must fail at least two cuts of the loose electron identification menu. As is the case for photon identification, the loose electron identification algorithm applies requirements only on a subset of variables, resulting in a higher acceptance rate than the tight identification menu, at the expense of decreased background-rejection performance.

- The probe electron must have isolation $E_{\mathrm{T}} > p_{\mathrm{T}}/0.05$

These cuts result in a sample of electrons which contains an enhanced background fraction, suitable for usage in estimating the fraction of selected probes which come from background events. Normalisation is performed in the high m_{ee} tail, defined as $m_{ee} > 120$ GeV. It is also important to realise that, much as the signal selection is contaminated by some background events, the background template can similarly suffer from signal contamination. This must be accounted for when normalising the template. Normalisation is therefore not a trivial case of simply scaling the derived background template to the signal selection in a given region, but is slightly more complex. The number of signal events contained within the tail of the signal selection must be estimated. To achieve this, the number of signal events within the signal selection in which the tag electron passes tight electron identification is estimated, and then divided by the tight electron identification efficiency. Division by the tight electron identification efficiency gives an estimate of the total number of signal events within the tail, which is subtracted before normalising the template. This process allows for the template to be correctly normalised to the background component of the signal selection high-mass tail. The resulting normalised template is then used to estimate the fraction of events in the signal selection peak which come from background events. The results of this are shown in figure 5.4 for a representative p_{T} bin.

5.5 Smirnov Transformations

In the case of converted photons, shower shapes are similar enough to electrons that a reasonable approximate measurement of the photon identification efficiency may be made by simply applying the photon ID cuts to the electron sample directly. Unconverted photons, however, differ more significantly, and this simple method

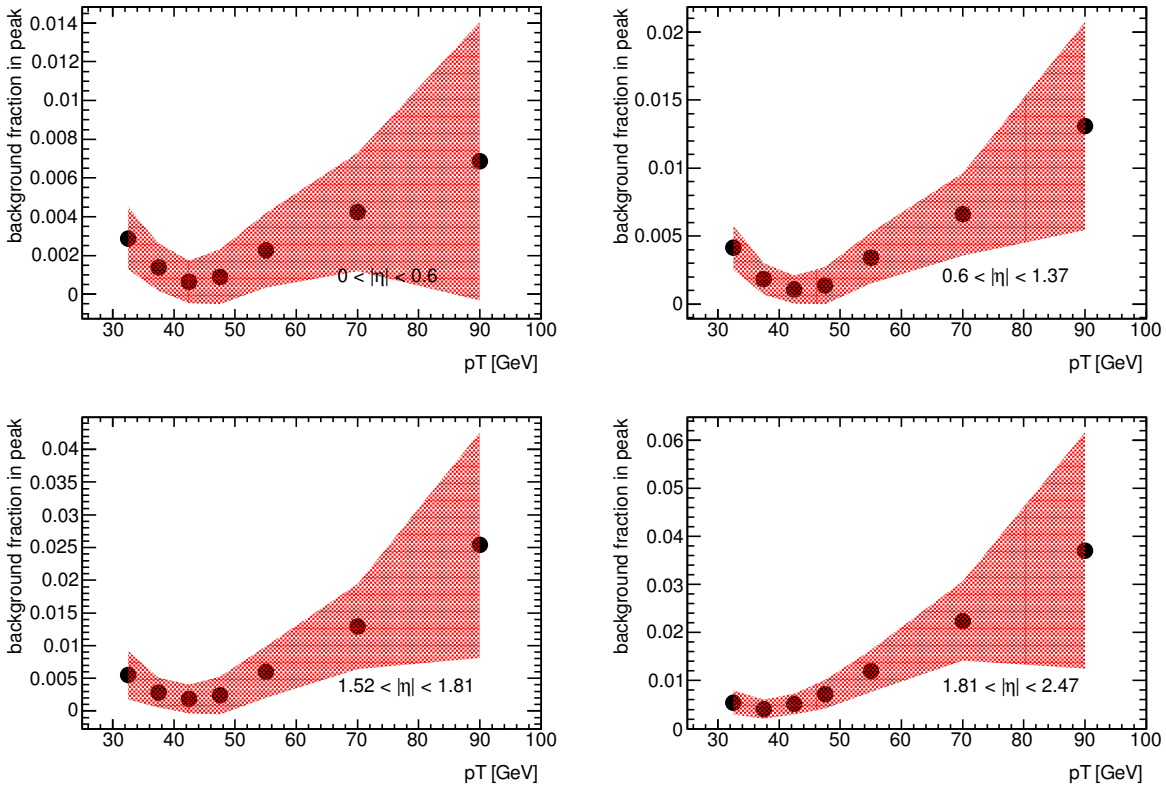

FIGURE 5.4: The estimated background contamination in the peak region (80 GeV $< M_{ee} <$ 100 GeV) of the $Z \to e^+e^-$ signal selection, in four η regions. The shaded area indicates the uncertainty resulting from the statistical uncertainties on the signal and background-enhanced samples.

would fail. This section describes one method of extrapolation from electrons, in which the shower shape distributions from the electron sample are transformed into a set of shower shape distributions more representative of photons. Unconverted and converted photons are considered separately, though the method is applied identically in each case.

The method relies on using the shower shape distributions of MC electron and photon samples to derive Smirnov transformations (described in section 5.5.1), which can be used as a mapping between electron and photon shower shape distributions. The application of these transformations to a sample of electrons from data provides a set of shower shape distributions which should closely resemble those of a true set of photons from data. An illustration of the samples used and the operations performed on them is given in figure 5.5.

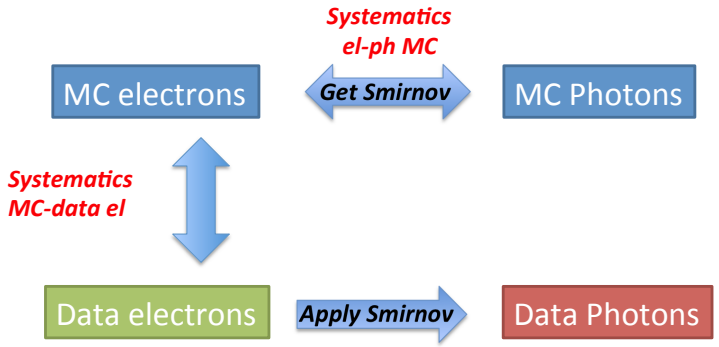

FIGURE 5.5: Diagram representing which samples are involved in each stage of the Smirnov transformation method of electron extrapolation.

5.5.1 SMIRNOV TRANSFORMATIONS

Smirnov transformations [74], also known as inverse transformations, provide a method for generating numbers according to a probability distribution. By treating the shower shape distributions of electrons and photons as probability distributions for that shower shape variable, it is possible to use the method to generate a photon-like set of shower shape distributions by starting from the shower shape distributions of electrons. Figure 5.6 illustrates the process for one shower shape variable. Initially, the cumulative distribution functions (CDFs) of both electron and photons are calculated for the given variable. A mapping is derived, giving for each source value the shift which is necessary to take it to the value which occupies the same position in the CDF of the target distribution. By deriving and applying this shift for each shower shape variable, the electron sample can be transformed into a sample of objects with photon-like shower shape distributions. As the process is applied to each shower shape variable independently, correlations between variables are preserved from the source sample. Smirnov transformations are invariant under systematic shifts which are correlated between the source and target distributions, which reduces the impact of uncertainties in the MC samples used in this study. Due to differences in the $|\eta|$ and p_{T} distributions of the source

and target samples, and to the dependency of shower shapes and photon identification cuts on $|\eta|$, p_{T} and whether or not the photon is converted, this process is performed in regions of p_{T} and $|\eta|$ and is applied separately to converted and unconverted photons.

The CDFs on which the process relies are computed from binned distributions, rather than being continuous mathematical functions. For this reason, the calculated mapping is also a non-continuous series of shift values. When applying the transformation to any given value of a shower shape, a linear interpolation is made between the two nearest bins. As a result, there are some imperfections in the transformation which is obtained when applying the method, particularly if the distributions have major discontinuities (small bins are used to minimise any bias from this effect). The ability of the Smirnov transformation to provide a reliable transformation to photon shower shape distributions is thus somewhat dependent upon the sample size, and high statistics samples are required both from MC and data. This statistics dependence also limits the extent to which the analysis can be split into separate regions according to variables such as p_{T} and $|\eta|$.

5.6 Cross-checks and Systematic Uncertainties

There are several sources of systematic uncertainty which contribute to the overall systematic uncertainty on the measurement of photon ID efficiency via electron extrapolation with Smirnov transformations. The method itself has some intrinsic error, which is assessed by the closure test shown in section 5.6.1. Another contribution results from uncertainties in the MC samples used to derive the Smirnov transformations. The method is also sensitive to differences between shower shape distributions in data and in simulation. The extent to which this affects the measurement is discussed in section 5.6.2. Aspects of the simulation such as the

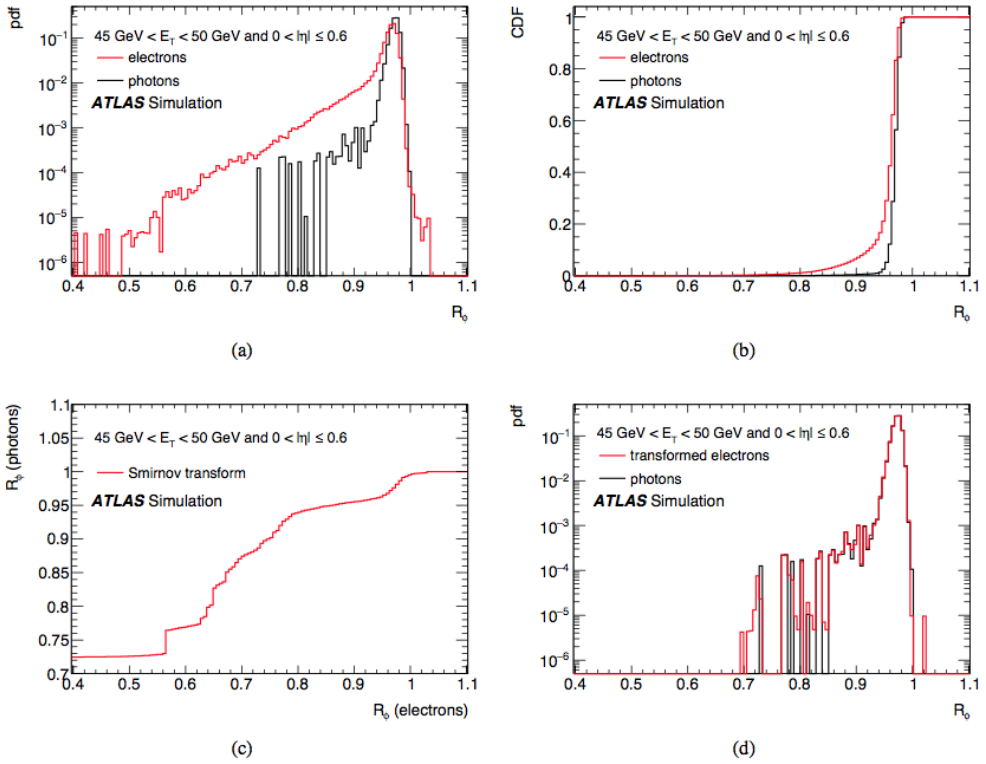

FIGURE 5.6: Diagram illustrating the process of Smirnov transformation. R_ϕ is chosen as an example of a shower shape which is particularly divergent between electrons and photons. The R_ϕ distribution in each sample (a) is used to calculate the respective CDF (b). From the two CDFs, a Smirnov transformation can be derived (c). Applying the transformation leads to an R_ϕ distribution of the transformed electrons which closely resembles the photon distribution (d).

amount of material in front of the EMC may affect the differences between photon and electron shower shapes in the MC sample, which would in turn affect the magnitude of the closure test uncertainty. Section 5.6.3 discusses the impact of this source of uncertainty. Differences in shower shape distributions between background and signal events may have an effect on the measured efficiency, this is discussed in section 5.6.4.

5.6.1 Closure Test

The Smirnov transformation discussed in section 5.5 does not account for correlations between shower shape distributions, which introduces some intrinsic uncertainty to the method. Further possible errors intrinsic to the method result from

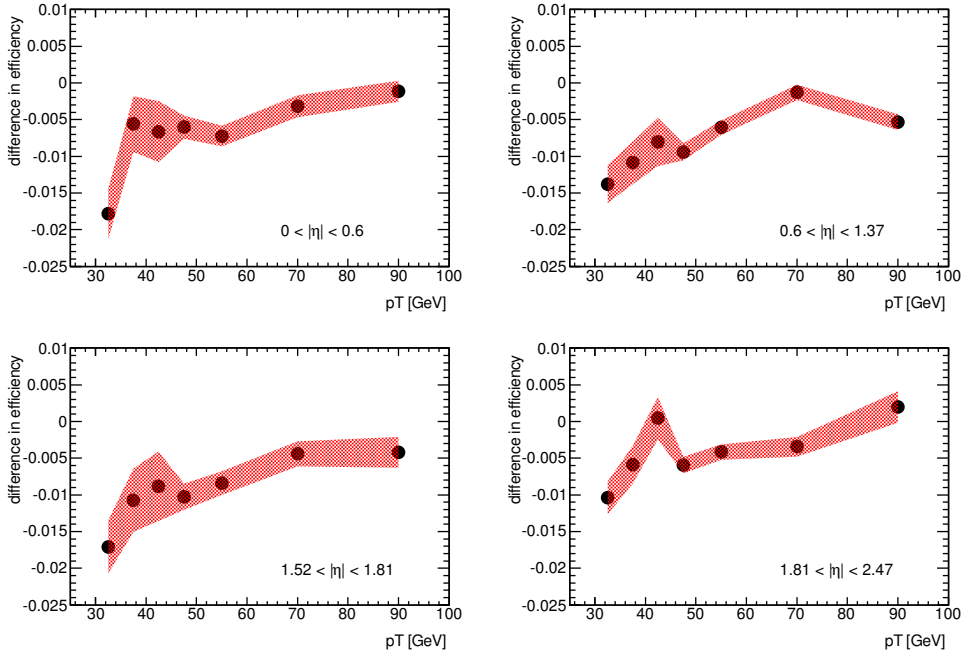

FIGURE 5.7: The closure test ($\varepsilon_{\mathrm{MC,photon}} - \varepsilon_{\mathrm{MC,electron,Smirnov}}$) for converted photons, in four regions of $|\eta|$. The shaded area indicates the combined statistical uncertainty resulting from the sizes of the photon and electron MC samples.

the different p_{T} distributions in the electron and photon samples, and the statistical limitations of the method by which the transformations are derived. These effects are assessed by comparing the efficiency measured from a pure sample of photons in MC to the efficiency measured from MC electron sample after applying Smirnov transformations.

Figures 5.7 and 5.8 show the closure test ($\varepsilon_{\mathrm{MC,photon}} - \varepsilon_{\mathrm{MC,electron,Smirnov}}$) for converted and unconverted photons respectively, in four $|\eta|$ bins. In the case of converted photons, the closure test estimates an intrinsic uncertainty from the Smirnov transform method of below 1.1% throughout the p_{T} and $|\eta|$ region considered. A larger effect is seen in the case of unconverted photons, where the maximum value is approximately 3%, and $O(1\%)$ is typical across the p_{T} and $|\eta|$ range in the study.

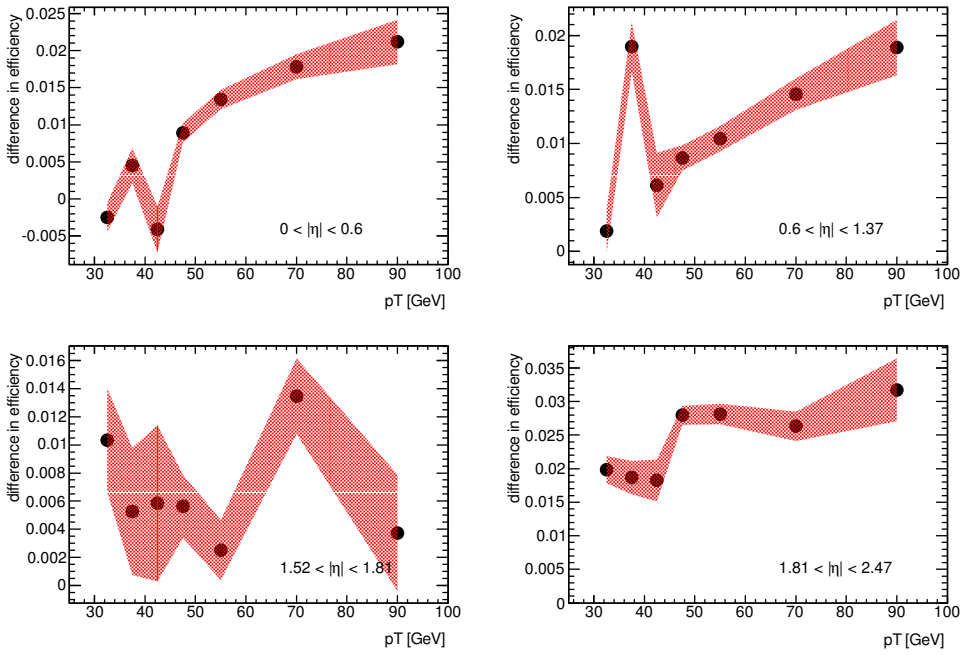

FIGURE 5.8: The closure test ($\varepsilon_{\mathrm{MC,photon}} - \varepsilon_{\mathrm{MC,electron,Smirnov}}$) for unconverted photons, in four regions of $|\eta|$. The shaded area indicates the combined statistical uncertainty resulting from the sizes of the photon and electron MC samples.

5.6.2 Differences Between Data and MC

Smirnov transformations are derived based on electrons from MC, but applied to data electrons. Differences between the shower shape distributions of data and MC which are simple uniform shifts would have no effect. This is because the Smirnov transformation applied to a data electron is that which corresponds to an MC electron occupying the same position in the CDF, which is invariant under any shift applying equally to both source and target distributions. In the case of more complex differences between data and MC, the Smirnov transform is not necessarily invariant and thus some effect may be seen. To see the extent to which these more complex differences affect the result, a comparison is made between the efficiencies obtained when applying tight photon ID to electrons in data and in MC.

Figure 5.11 shows the results of this check ($\varepsilon_{\text{data electrons}} - \varepsilon_{\text{MC electrons}}$) when applying converted photon ID requirements. The differences are most pronounced at

low p_{T} and high $|\eta|$, where a disagreement of up to 6% can be seen. At p_{T} above 45 GeV, the difference is generally around 2% or lower. The same comparison is made for unconverted photon ID in figure 5.12 and the largest effect is again seen to occur in the low p_{T} region. At low $|\eta|$, a larger difference is seen than for the converted photon ID. At high $|\eta|$, the difference observed is comparable to or smaller than for converted photon ID. The largest difference in any bin is around 7%, comparable to the maximum seen in the converted photon ID case. This check is a direct comparison of electrons in data to electrons in MC, and does not include any photon sample or application of Smirnov transformations. As such, it does not account for the fact that some differences between data and MC affect electron and photon MC samples in the same way, and so are invisible to the derived Smirnov transform. For this reason no systematic error is derived directly from this study, though the results are taken to confirm that the presence of non-trivial shower shape distortions can affect the efficiency measurement. A systematic uncertainty which estimates the extent to which these effects affect the efficiency measurement is discussed in section 5.6.3.

5.6.3 MC-related Uncertainty

Smirnov transformations are invariant under MC uncertainties which affect electrons and photons in the same way (i.e. if some distortion shifts photon shower shapes and electron shower shapes by the same amount, the derived Smirnov transformation will be the same as if there were no distortion). However, not all MC-related uncertainties have the same effect on both particle types, and the Smirnov transformation method is therefore sensitive to some uncertainties in MC modelling. To evaluate the impact of this, a test is carried out using *distorted geometry* MC samples. When producing these distorted samples, the detector geometry is simulated with more material situated in front of the electromagnetic calorimeter. The material modelling is thought to be the dominant source

of MC-related uncertainty, and in this study is the only one considered. A conservative approach is therefore taken and the difference in material distribution between nominal and distorted samples is somewhat exaggerated, such that the estimated uncertainty should also cover for the other effects (e.g. cross-talk within the detector) which are not directly considered.

Smirnov transformations are then derived using the MC samples generated with distorted geometry, and applied to data. The photon ID efficiency obtained from data after obtaining the nominal Smirnov transformations is then compared to the efficiency obtained after applying Smirnov transformations derived from the distorted samples. Figures 5.9 and 5.10 show the measured difference $(\varepsilon_{\text{nominal}} - \varepsilon_{\text{distorted}})$ for the converted and unconverted cases respectively. For converted photons the impact is relatively small, typically below 1.5% in most regions, with a largest observed difference of approximately 2%. Unconverted photons display a slightly larger effect, of up to 3% at high $|\eta|$, though the typical value remains below 2%.

The Smirnov transformation method is strongly dependent upon the sample size, and the MC samples with distorted material are somewhat smaller than those with the nominal geometry. This leads to uncertainties on the Smirnov transformations derived from those samples which are difficult to evaluate, but result in fluctuations on the efficiency measured after applying those Smirnov transformations to data electrons. As such, the individual measurements for every p_{T} bin are not retained as input for the total uncertainty calculation. Instead, the uncertainty for each $p_{\text{T}}, |\eta|$ bin is assigned as the weighted arithmetic mean of the absolute values obtained for that bin and the neighbouring p_{T} bins within the same $|\eta|$ region. This process is intended to *smooth* the uncertainty, avoiding the large fluctuations which would otherwise result from the statistical limitations of the small sample used for this study. In the calculation of the weighted arithmetic mean values,

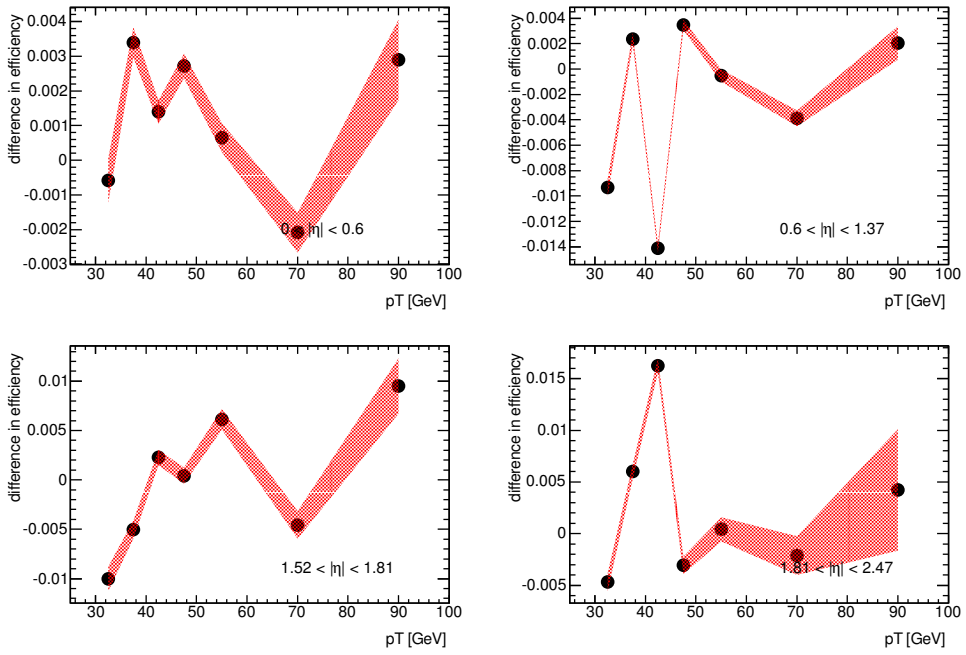

FIGURE 5.9: The difference between converted photon ID efficiency measurements obtained from data after applying Smirnov transformations computed from nominal and distorted MC samples. The difference in efficiency is presented as a function of p_{T} in four regions of $|\eta|$.

weights are assigned as $\frac{1}{\sigma^2}$, where σ is the statistical uncertainty on the measured efficiency difference in that bin.

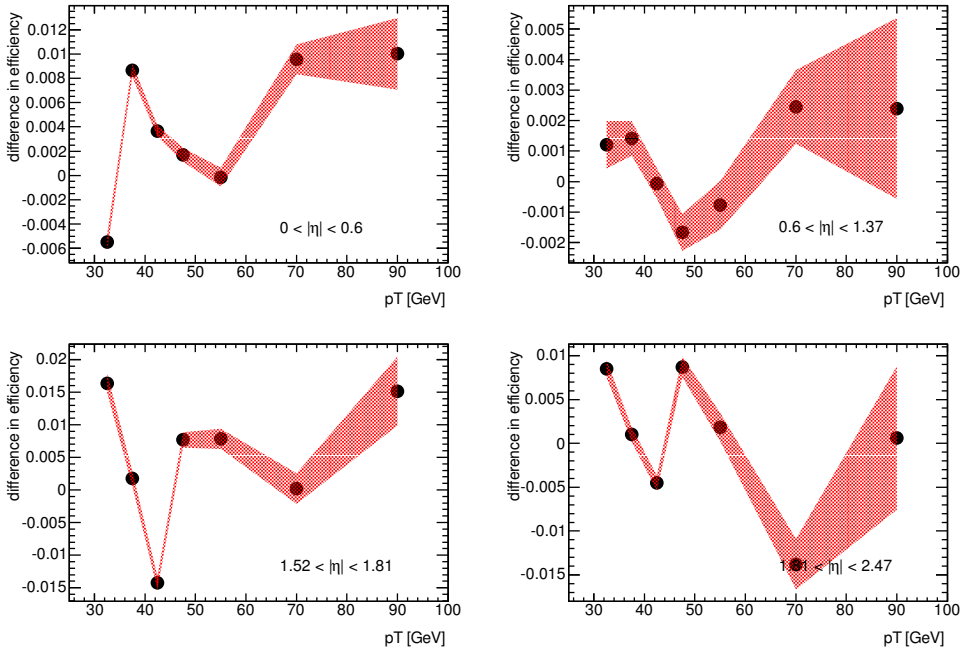

FIGURE 5.10: The difference between unconverted photon ID efficiency measurements obtained from data after applying Smirnov transformations computed from nominal and distorted MC samples. The difference in efficiency is presented as a function of p_{T} in four regions of $|\eta|$.

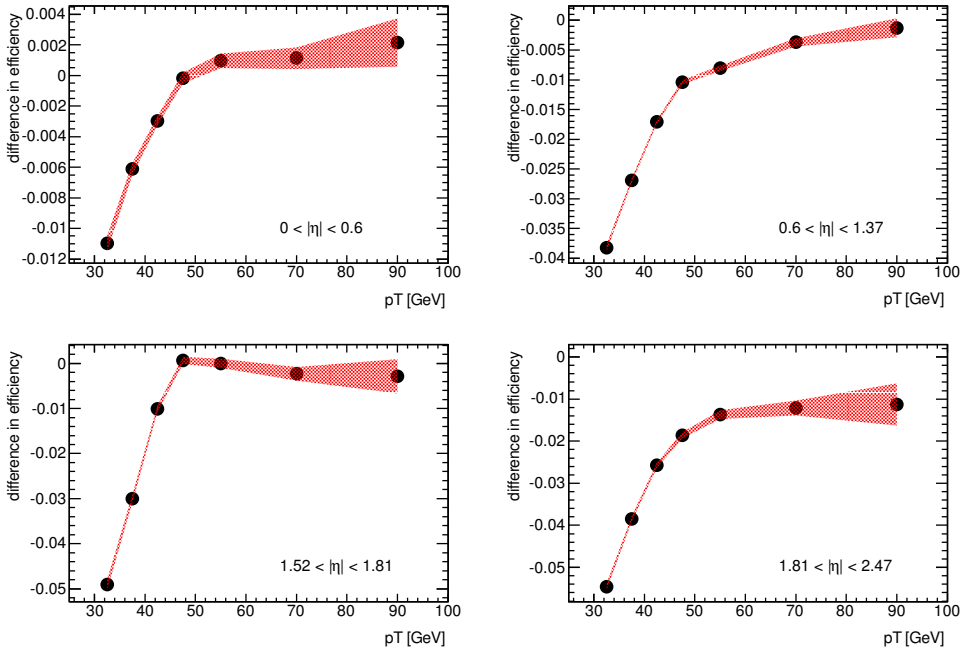

FIGURE 5.11: The difference ($\varepsilon_{\text{data electrons}} - \varepsilon_{\text{MC electrons}}$) between the efficiency obtained when applying tight converted photon ID to electrons in data and in MC. The difference in efficiency is presented as a function of p_{T} in four regions of $|\eta|$.

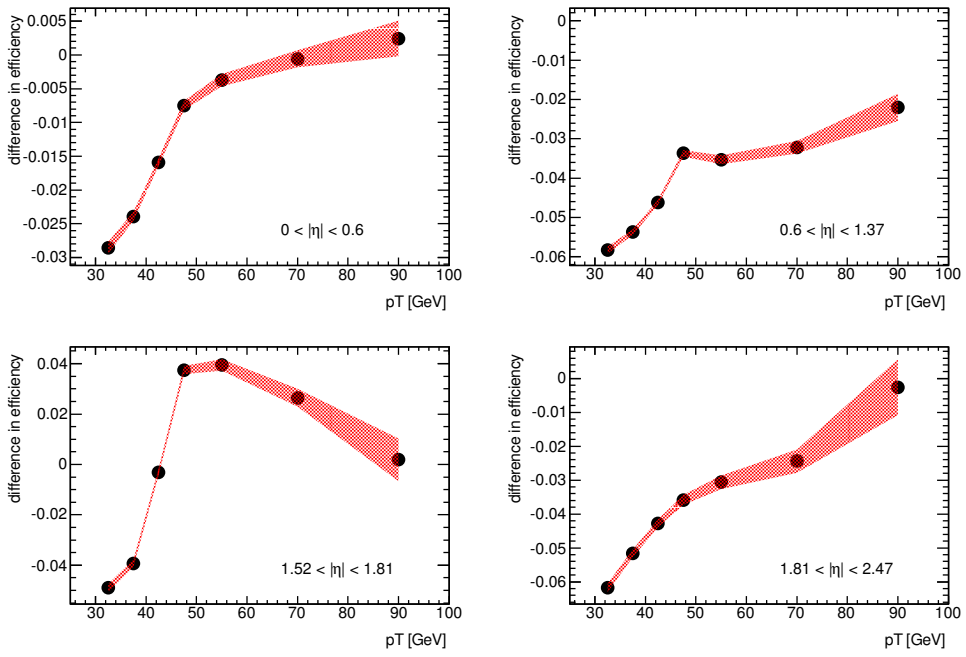

FIGURE 5.12: The difference ($\varepsilon_{\text{data electrons}} - \varepsilon_{\text{MC electrons}}$) between the efficiency obtained when applying tight unconverted photon ID to electrons in data and in MC. The difference in efficiency is presented as a function of p_{T} in four regions of $|\eta|$.

5.6.4 Background-Related Uncertainty

As discussed in section 5.4.1, a fraction of the selected electron sample comes from background events rather than true $Z \to e^+e^-$ decays. The shower shapes in this fraction of the sample may differ from the shower shapes from signal events, and so may potentially bias the efficiency measurement. Section 5.4.1 evaluated the level of background contamination within the selected sample, but to evaluate any effect on the measured efficiency it is important to also evaluate the background fraction within those transformed electrons which pass the tight photon selection. As the selection cuts are different, this must be evaluated separately for converted and unconverted photons.

To estimate this fraction of background within the tight sample, the same template described in section 5.4.1 is used. Due to the higher fraction of signal events within the tight sample, normalisation is performed in a different way. The template is normalised to the number of same-sign events passing the ID requirement in the high M_{ee} tail, which is assumed to have a negligible signal component. The background fraction remaining after applying tight ID is shown for converted and unconverted cases in figures 5.13 and 5.14 respectively.

By subtracting the estimated background components both before and after applying tight selection, an esimate can be made of the efficiency with corrections for the effect of background contamination in the selected electron sample. This background-subtracted efficiency is shown for converted and unconverted photons in figures 5.15 and 5.16 respectively. Figures 5.17 and 5.18 show the difference in efficiency measured with and without background subtraction. The value of this difference is added as a systematic uncertainty on the efficiency measurement.

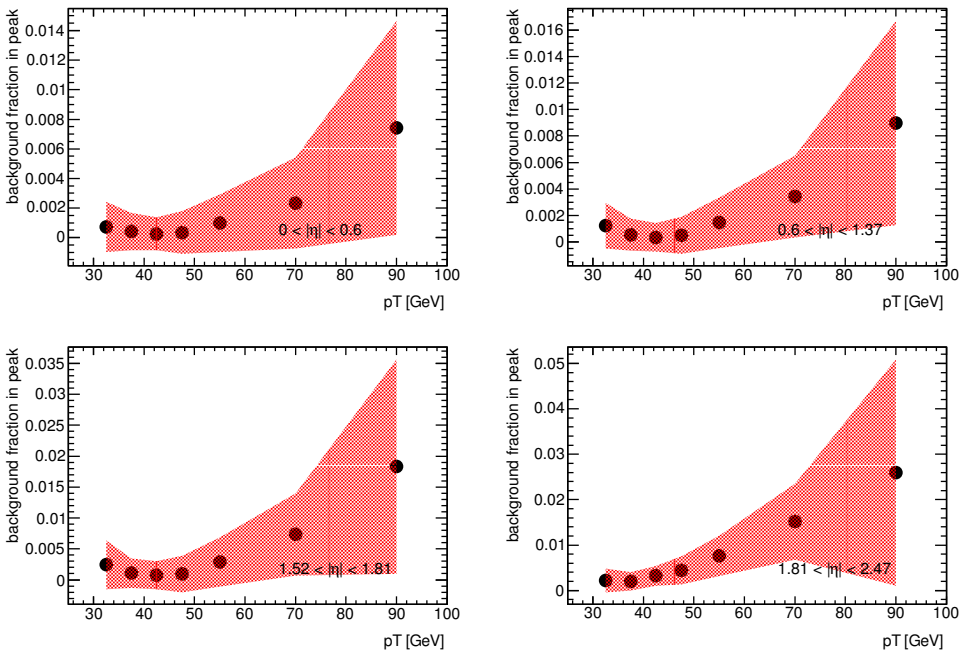

FIGURE 5.13: Estimated background contamination remaining after applying tight converted photon ID to the Smirnov-transformed electrons.

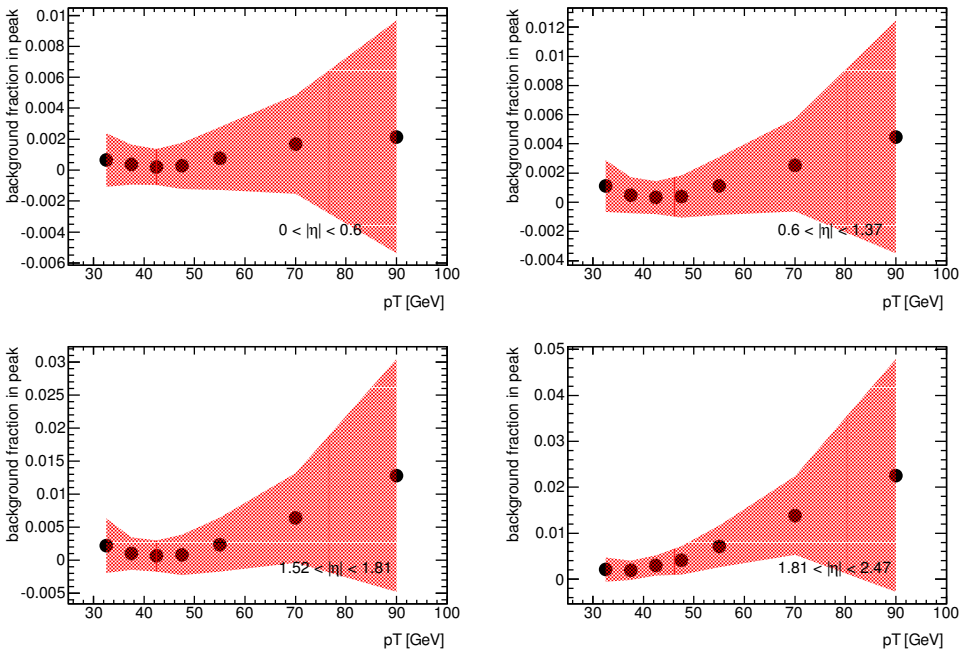

FIGURE 5.14: Estimated background contamination remaining after applying tight unconverted photon ID to the Smirnov-transformed electrons. The shaded area indicates the statistical uncertainty resulting from the size of the MC sample.

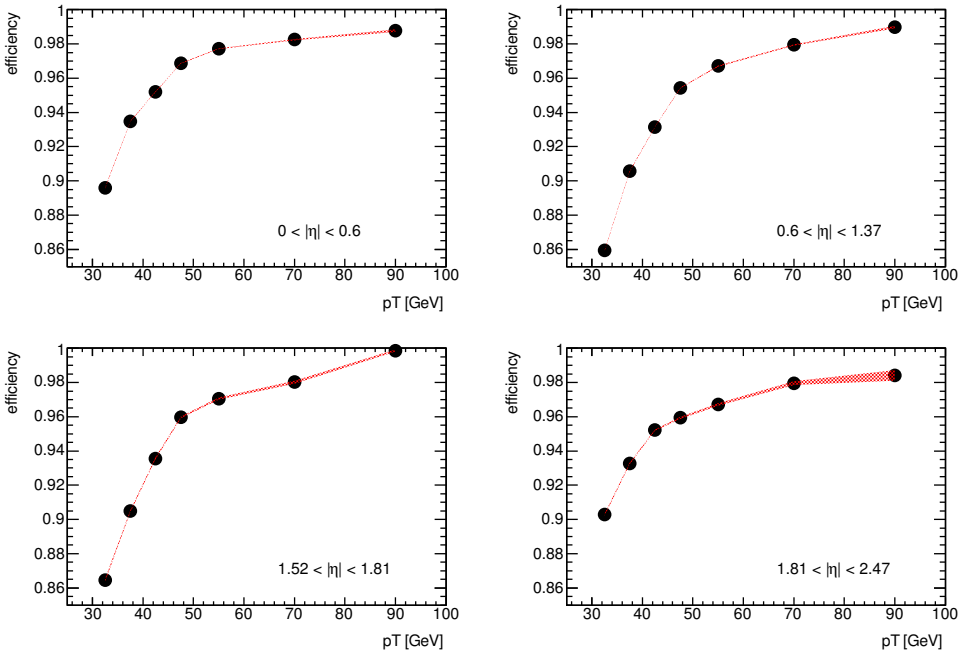

FIGURE 5.15: The background-subtracted efficiency measurement for converted photons.

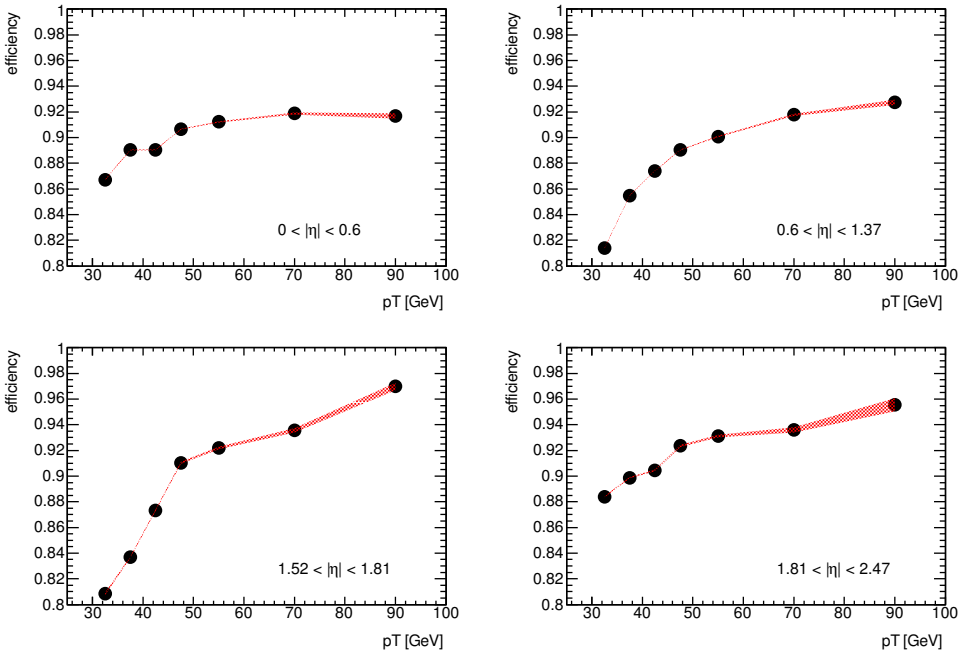

FIGURE 5.16: The background-subtracted efficiency measurement for unconverted photons.

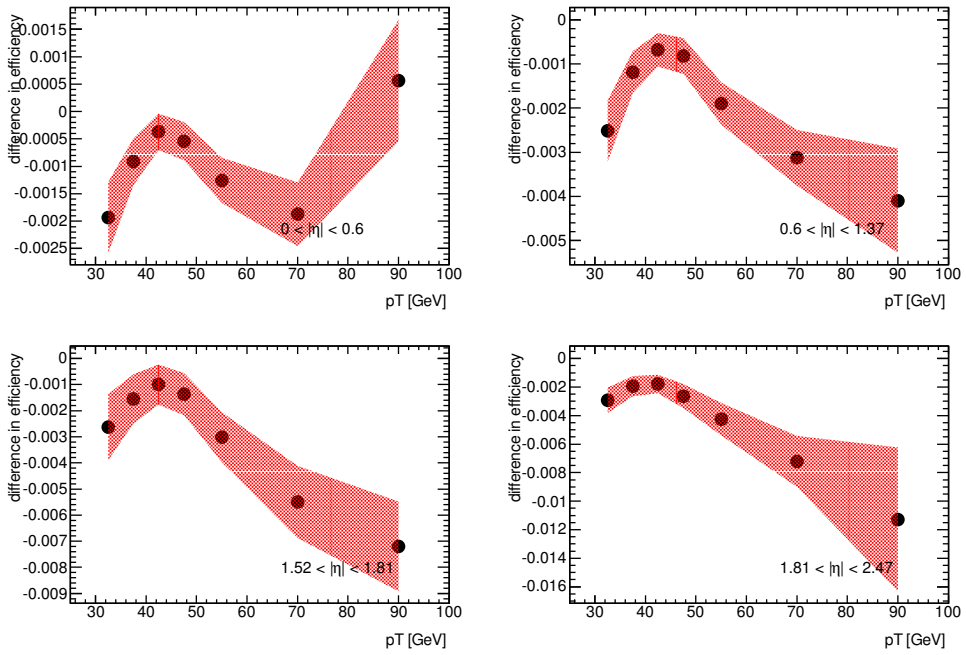

FIGURE 5.17: The difference $\varepsilon_{\text{nominal}} - \varepsilon_{\text{bkg subtracted}}$ between efficiency measurements for converted photons with and without background subtraction.

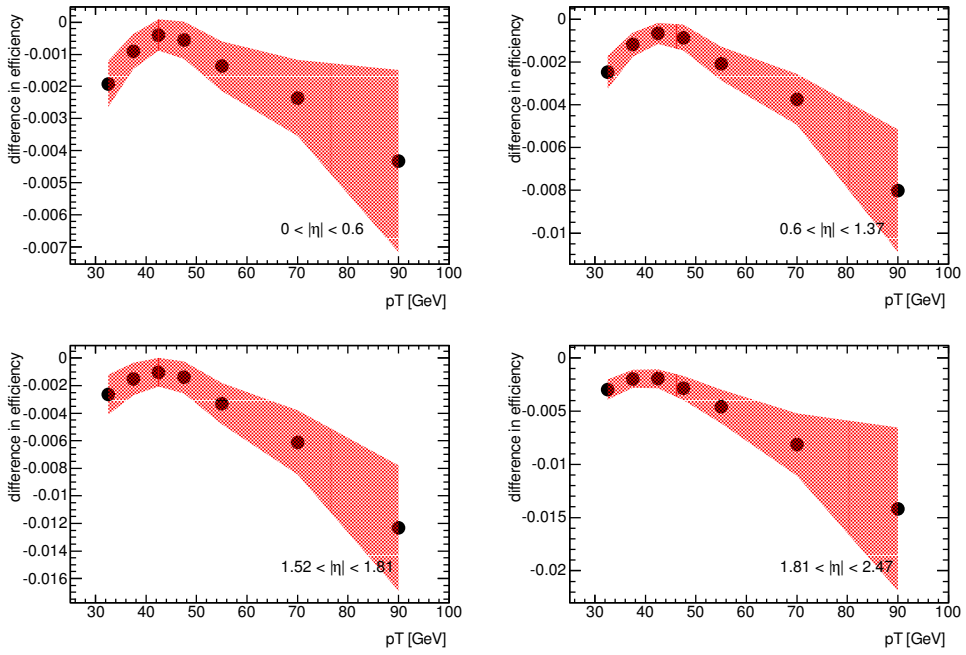

FIGURE 5.18: The difference $\varepsilon_{\text{nominal}} - \varepsilon_{\text{bkgsubtracted}}$ between efficiency measurements for unconverted photons with and without background subtraction.

5.7 Results

A sample of electrons selected from $Z \to e^+e^-$ events has been used to make a measurement of the efficiency of the ATLAS tight photon ID identification, by extrapolating from electrons to photons with Smirnov transformations, as described in section 5.5. The measurement has been carried out as a function of p_{T} in 8 $|\eta|$ regions, which are combined for presentation into a less granular set of 4 $|\eta|$ regions. The systematic uncertainties are summarised below:

- A comparison is made between the efficiency in a transformed MC electron sample and the efficiency in an MC photon sample, to assess the impact on the measurement resulting from the different p_{T} and $|\eta|$ distributions, as well as the effect of different correlations between shower shapes and the limited size of the MC samples available. As shown in section 5.6.1, the effect is found to be at most $O(1\%)$ for converted photons and $O(2.5\%)$ for unconverted photons.

- An additional set of Smirnov transformations is calculated using a set of MC samples which are simulated with the inclusion of additional material in front of the EMC. The difference in efficiency between data electrons transformed according to Smirnov transformations derived from MC samples with the nominal and distorted geometries is taken as a measure of the method's sensitivity to inaccuracies in the MC simulation. As the Smirnov transformation method is highly sensitive to the low statistics of the distorted material MC sample, the value of this uncertainty is assigned by taking a weighted average of each bin with its immediately neighbouring p_{T} bins. This is discussed in section 5.6.3. An effect is found of up to $O(1.5\%)$ for converted photons and $O(3\%)$ for unconverted photons.

- A data-driven, template-based method is used to estimate the background contamination in the selected electron sample, and the effect of the background contamination on the measured efficiency. For each $p_{\mathrm{T}}, |\eta|$ bin, the background-subtracted efficiency is used as the central value of the quoted efficiency, and an uncertainty is assigned which is equal to the difference between measurements with and without background subtraction. This effect is found to be smaller than 0.5% in all $p_{\mathrm{T}}, |\eta|$ bins for both converted and unconverted photons.

5.7.1 Identification Efficiency

The efficiency curves resulting from the electron extrapolation study are compared to those obtained from a Monte Carlo sample in which the shower shapes are tuned by the application of so-called *fudge factors* so that they better resemble those seen in data. As with the other MC samples used in this study, this fudge-factor Monte Carlo (*FFMC*) sample is reweighted based on the average number of interactions per bunch crossing, so that the distribution in the FFMC matches that in the data sample.

Figures 5.19 and 5.21 show these comparisons for converted and unconverted photons respectively. The FFMC efficiency is indicated by the red points. The data-driven efficiency measurement is shown by the black points, with error bars indicating the statistical and systematic uncertainties (added in quadrature) on the data-driven measurement.

For converted photons (figures 5.19 and 5.20), the difference between the central values of the data-driven and FFMC efficiency measurements is typically of $O(1\%)$ or less. The combined statistical and systematic uncertainty is typically around $\pm 3\%$, and at maximum approximately $\pm 6\%$. The efficiency observed in the FFMC

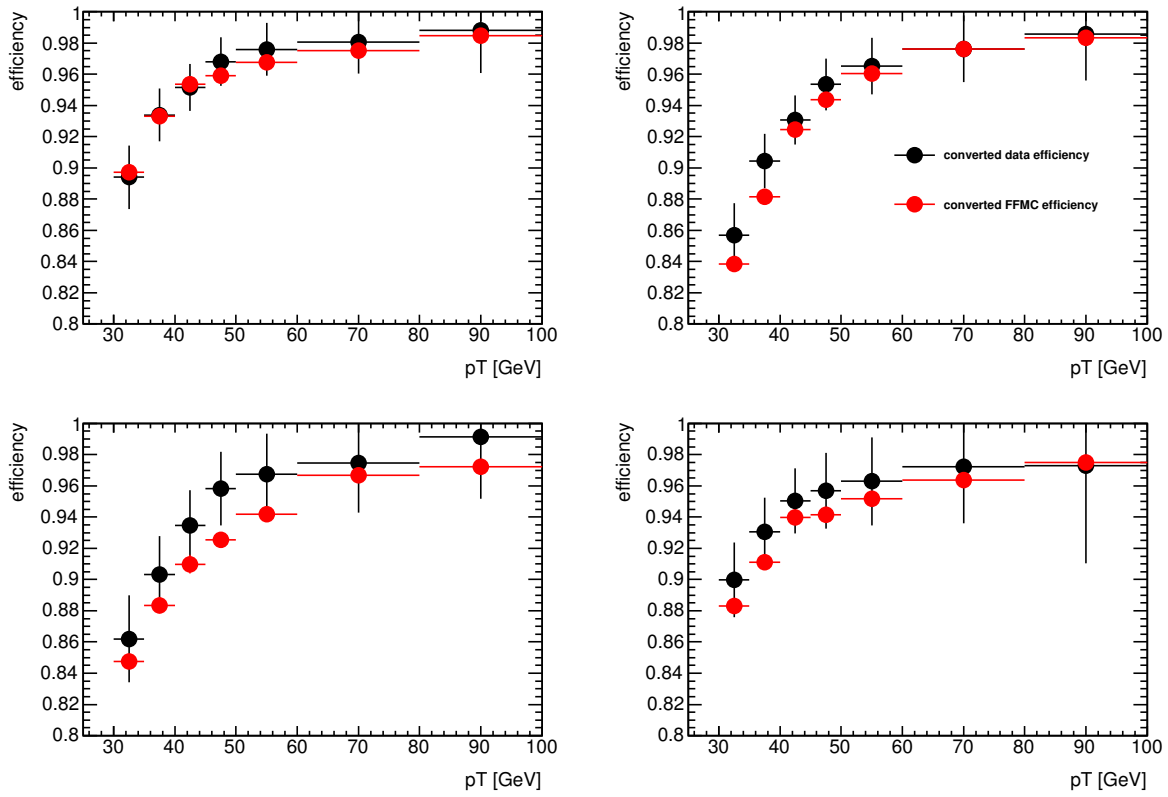

FIGURE 5.19: A comparison of the efficiency measurement obtained from data electrons after applying Smirnov transformations to those obtained from an MC photon sample with fudge factors applied. The efficiency curves in this figure are for converted photons. The error bars indicate the statistical and systematic uncertainty on the data measurement, combined by addition in quadrature.

sample agrees with the data-driven measurement to within the uncertainty band throughout the $|\eta|$ and p_{T} range of the study.

For unconverted photons (figures 5.21 and 5.22), the difference is slightly larger, but still below 2% in most cases. The combined uncertainty is mostly similar to the converted case, with typical values of around 3%, with a larger maximum than for converted photons (around $\pm 7\%$). The agreement between data-driven and FFMC measurements is good across most of the $|\eta|$ and p_{T} range, with typical differences of 2% or less. Most points agree within the uncertainty band, though there is a small disagreement at low p_{T} in the range $1.52 < |\eta| < 1.81$. As discussed in section 5.6.3, material within the detector has an impact upon the measurement. It is therefore not entirely surprising that this $|\eta|$ region displays

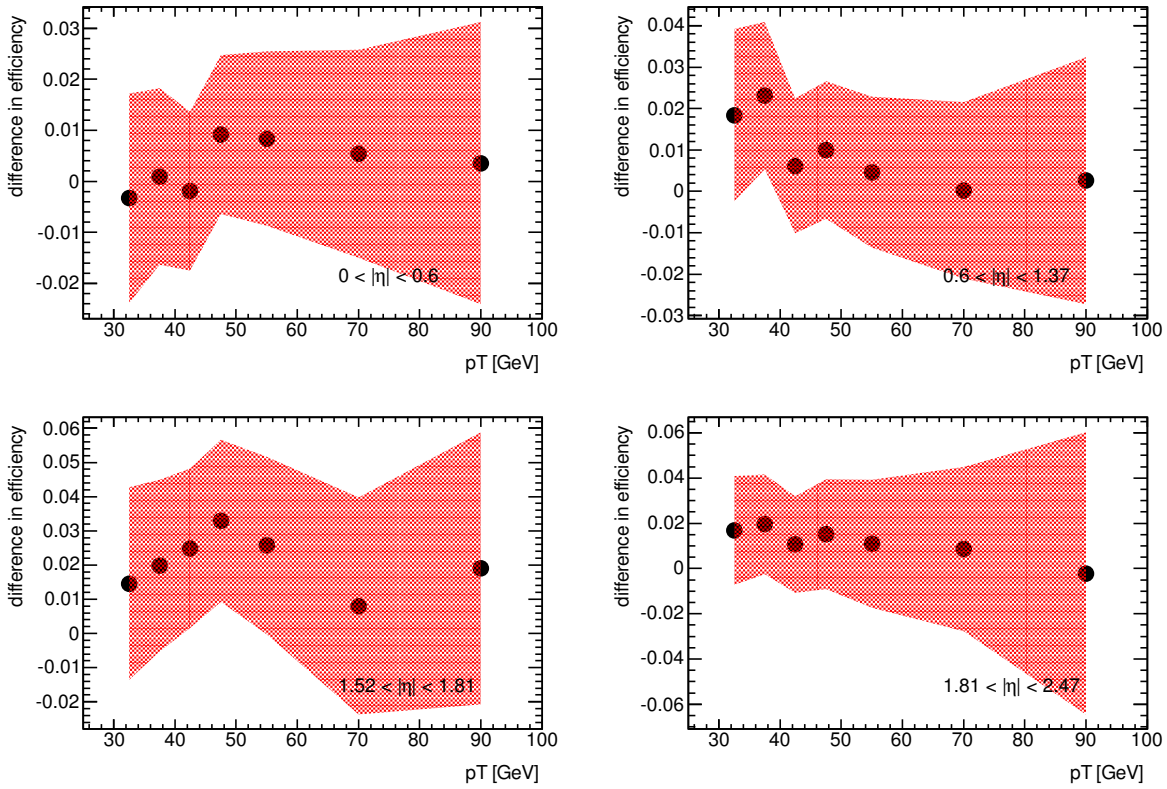

FIGURE 5.20: A comparison between data and FFMC efficiency measurements in the form of the absolute efficiency difference for converted photons ($\varepsilon_{data} - \varepsilon_{MC}$).

worse performance, as there is much material contained within this region of the detector (as illustrated in figure 5.23).

For both converted and unconverted photons, it is observed that in all $|\eta|$ regions the efficiency is lowest at low p_{T}, and increases rapidly with p_{T} before levelling off typically at around 50 GeV. The lower efficiency at low p_{T} is a result of the fact that the cut values used for photon identification do not vary with the p_{T} of the reconstructed photon candidate, and so low-p_{T} photons are less likely to pass the identification requirements due to their broader showers. The increased uncertainty on unconverted photons results from the fact that the differences from electron shower shapes are larger than for converted photons, and so there is a stronger dependence on the Smirnov transforms. Efficiencies are lower for unconverted photons than for converted photons, which results from the fact that the

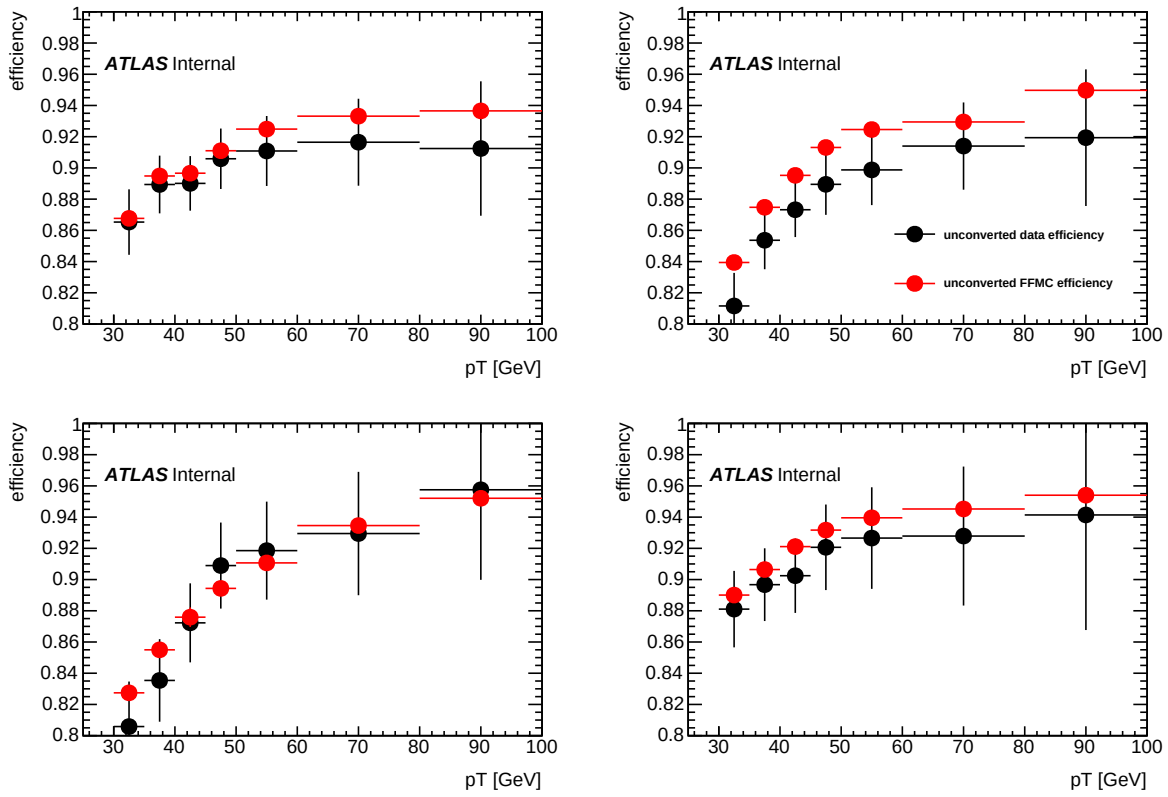

FIGURE 5.21: A comparison of the efficiency measurement obtained from data electrons after applying Smirnov transformations to those obtained from an MC photon sample with fudge factors applied. The efficiency curves in this figure are for unconverted photons. The error bars indicate the statistical and systematic uncertainty on the data measurement, combined by addition in quadrature.

cuts placed on shower shape variables are tighter for unconverted photon identification than for identification of converted photons. The full results are shown in tables 5.5 and 5.6, for converted and unconverted photons respectively.

5.7.2 Fragmentation Photons

The Monte Carlo photon samples used in this analysis are *prompt photon* samples. The definition of *prompt photon* used here includes both direct photons, which originate directly from the hard process, and *fragmentation photons*, which originate from the fragmentation of high-p_{T} coloured partons [75][76]. Fragmentation photons, as a result of the differing production kinematics, tend to be less isolated than direct photons. Shower shape distributions differ between isolated

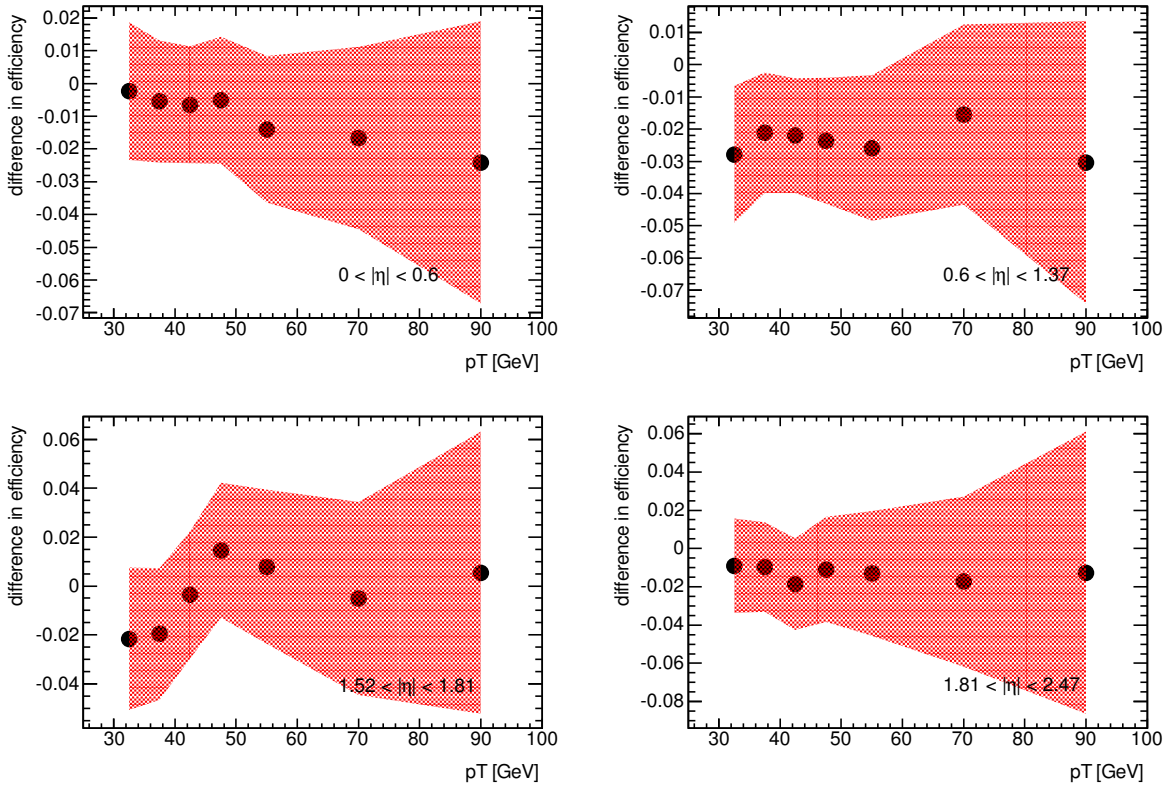

FIGURE 5.22: A comparison between data and FFMC efficiency measurements in the form of the absolute efficiency difference for unconverted photons ($\varepsilon_{data} - \varepsilon_{MC}$).

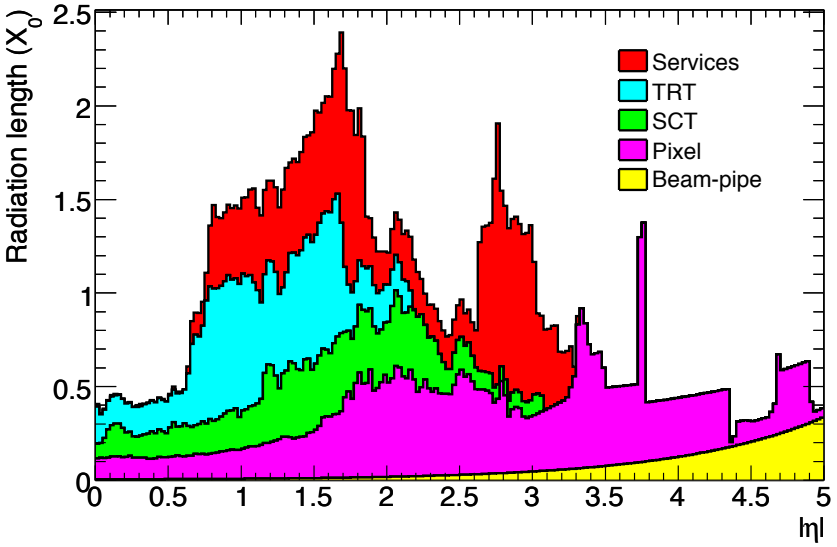

FIGURE 5.23: The material budget of the ATLAS detector[41], displayed in units of radiation length, X_0, against the absolute value of pseudorapidity, $|\eta|$.

and isolated photons and as such a difference exists between the efficiencies of fragmentation and direct photons. Any mis-modelling of the fragmentation fraction in the MC sample used in the derivation of the Smirnov transforms could therefore introduce a bias into the measured efficiency, especially as the fraction of fragmentation photons selected in a data analysis will vary depending on the physics processes being studied.

In this section, a study is performed to evaluate the extent of this effect by varying the fragmentation fraction in the MC sample. Two variations are used. In one, all fragmentation photons are removed from the MC sample. In the other, the weight applied to the fragmentation photons is doubled. Smirnov transformations are re-derived with the varied MC samples, and applied to data. In this way an estimate is made of the photon identification efficiency with no fragmentation photons and the efficiency with twice the number of fragmentation photons present in the nominal MC sample.

Figures 5.24 and 5.25 show the efficiencies measured from data after applying the Smirnov transforms from each fragmentation variation for converted photons. The measurements for unconverted photons are shown in figures 5.26 and 5.27. With the exception of one p_{T}, η bin when studying unconverted photons with no fragmentation component, the difference between the nominal MC sample and the MC samples with a varied fragmentation photon component is observed to be consistently at the level of 1% or below for both converted and unconverted photons. The outlying bin displays a difference in efficiency of around 1.5%. This measurement of the effect of fragmentation photons on the photon identification efficiency is presented as a cross-check. It is not included in the final uncertainties of the photon identification efficiency measurement via electron extrapolation as it is measured for the final ATLAS photon identification efficiency recommendation using a separate method, as will be described in section 5.8.4.2.

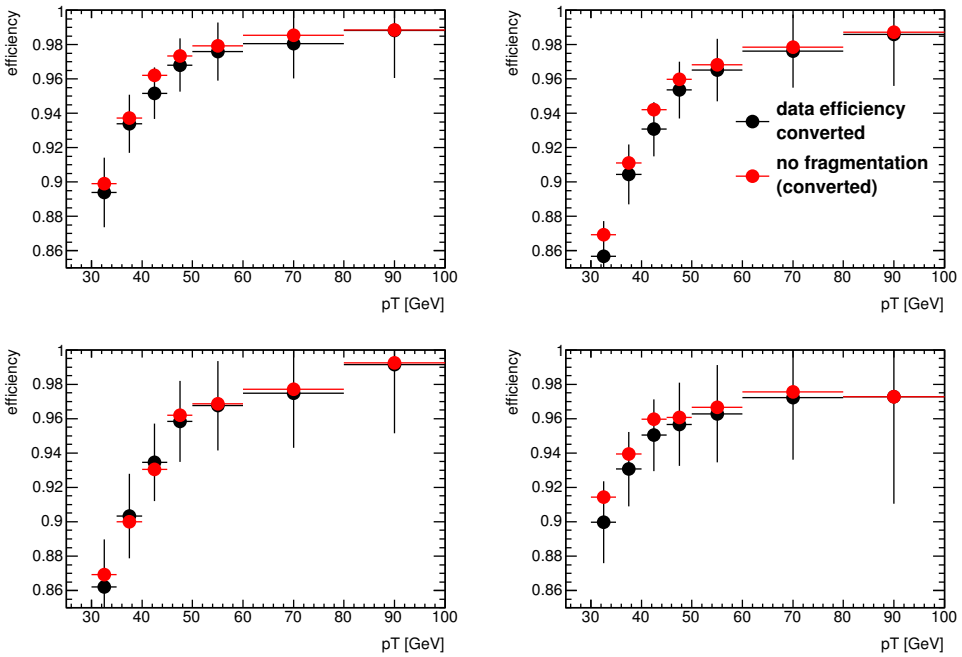

FIGURE 5.24: Converted photon efficiency (red) measured when using Smirnov transformations derived from photon MC with the fragmentation fraction removed. The efficiency using nominal fragmentation fraction is shown in black for comparison.

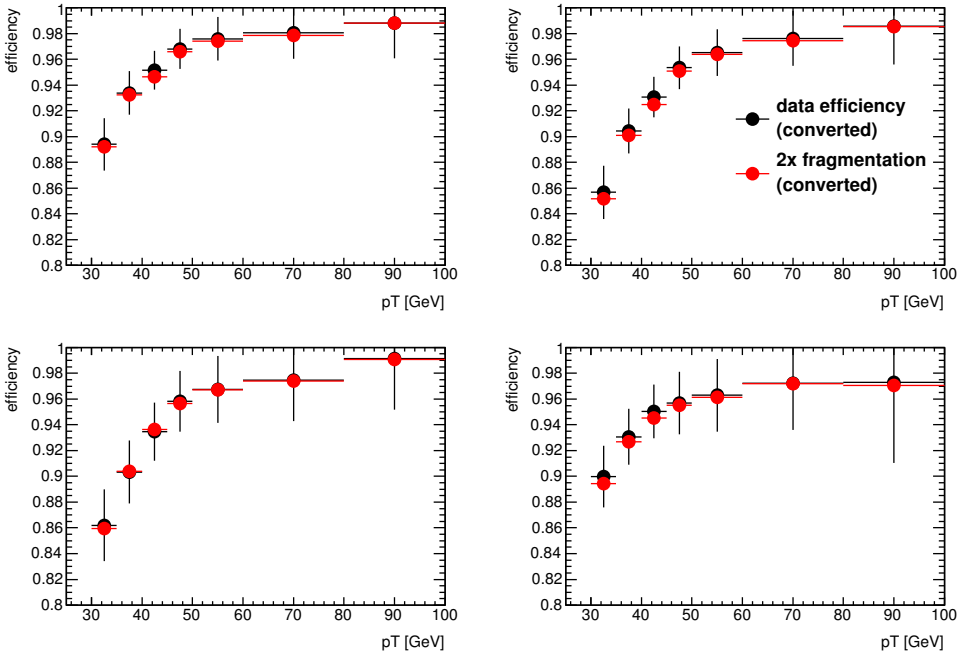

FIGURE 5.25: Converted photon efficiency (red) measured when using Smirnov transformations derived from photon MC with double weight applied to the fragmentation fraction. The efficiency using nominal fragmentation fraction is shown in black for comparison.

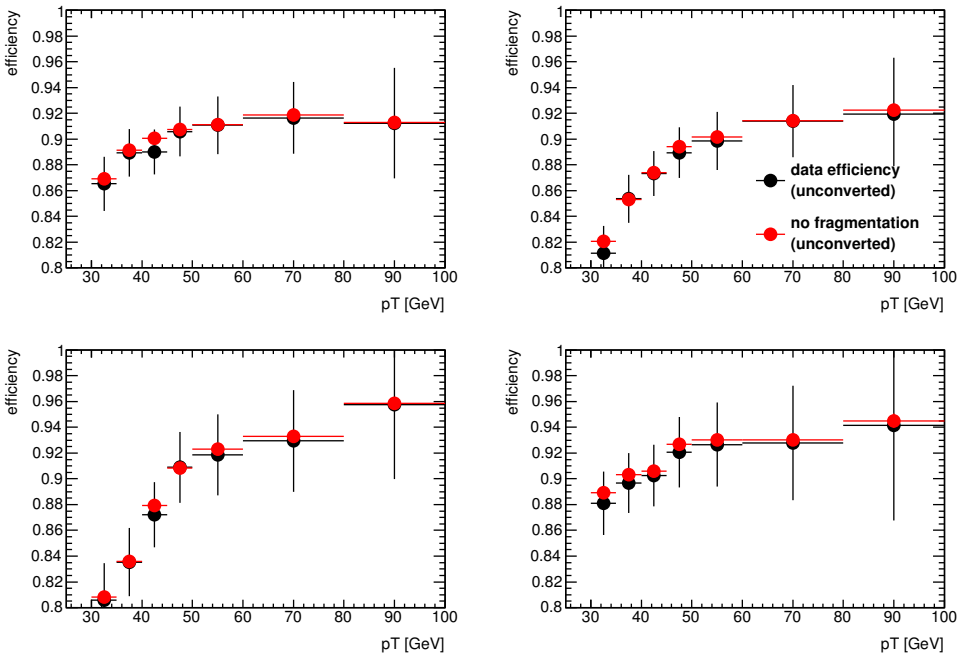

FIGURE 5.26: Unconverted photon efficiency (red) measured when using Smirnov transformations derived from photon MC with the fragmentation fraction removed. The efficiency using nominal fragmentation fraction is shown in black for comparison.

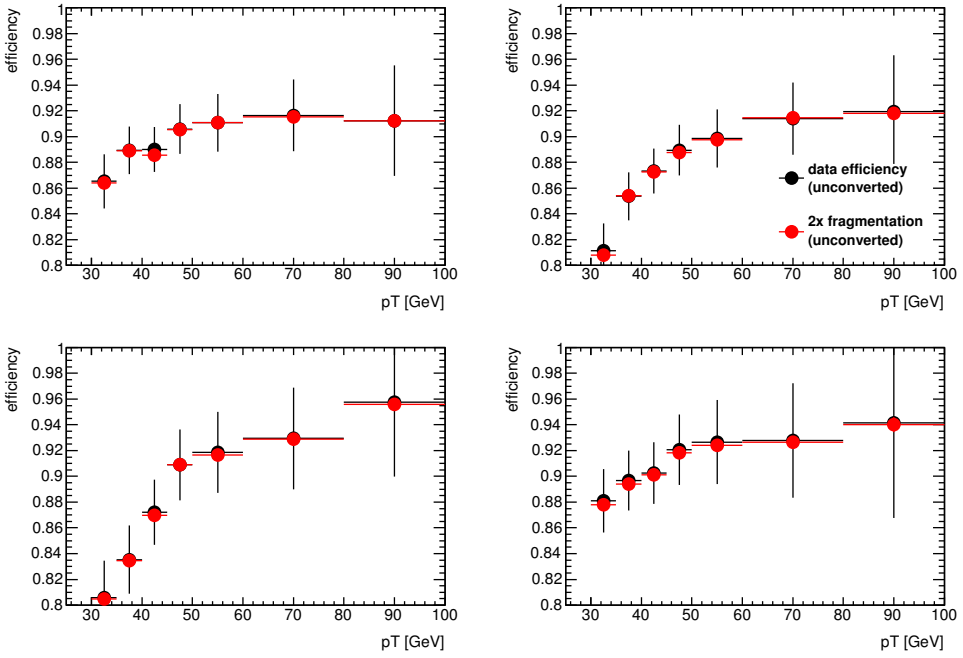

FIGURE 5.27: Unconverted photon efficiency (red) measured when using Smirnov transformations derived from photon MC with double weight applied to the fragmentation fraction. The efficiency using nominal fragmentation fraction is shown in black for comparison.

5.7.3 Pileup Dependence

Pileup can affect the shower shapes of photons due to the additional energy deposited in the calorimeter by particles from additional interactions. This predominantly includes As such, there may also be an impact on the photon identification efficiency. The MC samples used in this measurement of photon identification efficiency are re-weighted to match the pileup distribution of the data sample, but some systematic uncertainty may result if the effect of pileup is not correctly simulated. For this reason, the ratio of efficiency measured in data to efficiency measured in MC is studied as a function of the number of reconstructed primary vertices (N_{PV}) per event. For this study, an alternative binning is used during the calculation of Smirnov transformations. Rather than the two-dimensional $p_{\mathrm{T}}, |\eta|$ binning used in the rest of this note, a three-dimensional $p_{\mathrm{T}}, |\eta|, N_{\mathrm{PV}}$ binning is used. For the calculation of Smirnov transformations, the data is separated into two N_{PV} bins, $N_{\mathrm{PV}} \leq 17$ and $N_{\mathrm{PV}} > 17$. Due to the statistics dependence of Smirnov transforms, it is not possible to retain the fine p_{T} binning used elsewhere in this note, instead Smirnov transformations are calculated with a much coarser p_{T} granularity which contains only two bins, $p_{\mathrm{T}} < 45\,\mathrm{GeV}$ and $p_{\mathrm{T}} \geq 45\,\mathrm{GeV}$. Binning in $|\eta|$ is not altered.

Figures 5.28 and 5.29 show the data/MC identification efficiency ratio as a function of N_{PV} for converted photons in the p_{T} ranges $30\,\mathrm{GeV} < p_{\mathrm{T}} < 45\,\mathrm{GeV}$ and $p_{\mathrm{T}} > 45\,\mathrm{GeV}$ respectively. Figures 5.30 and 5.31 show the data/MC identification efficiency ratios for unconverted photons in the same p_{T} ranges. The plots also show the results of fitting the data to a straight-line, in each case the slope is consistent with zero to within the uncertainties. The pileup dependence of the data/MC efficiency ratio is therefore considered negligible.

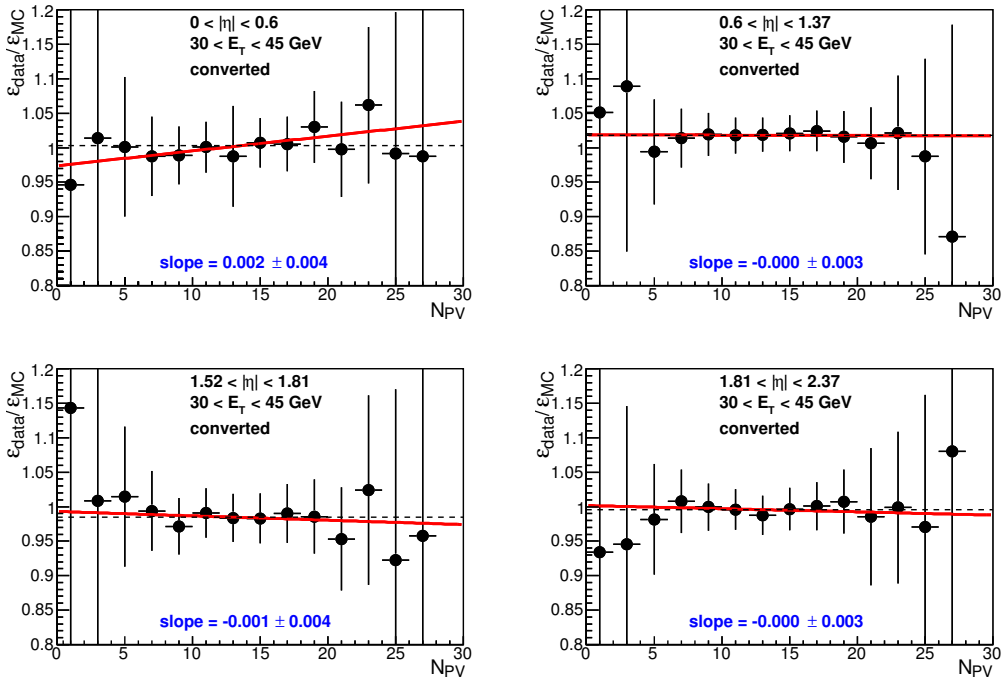

FIGURE 5.28: The measured ratio $\varepsilon_{\text{data}}/\varepsilon_{\text{MC}}$ as a function of N_{PV} for converted photons with p_{T} in the range $30\,\text{GeV} < p_{\text{T}} < 45\,\text{GeV}$

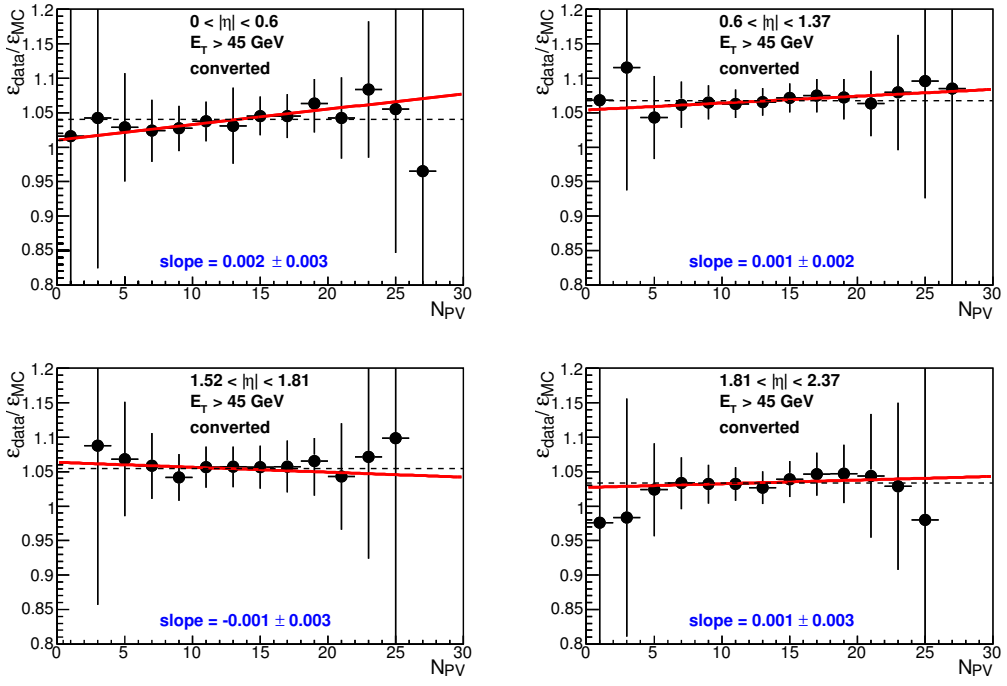

FIGURE 5.29: The measured ratio $\varepsilon_{\text{data}}/\varepsilon_{\text{MC}}$ as a function of N_{PV} for converted photons with p_{T} in the range $p_{\text{T}} > 45\,\text{GeV}$

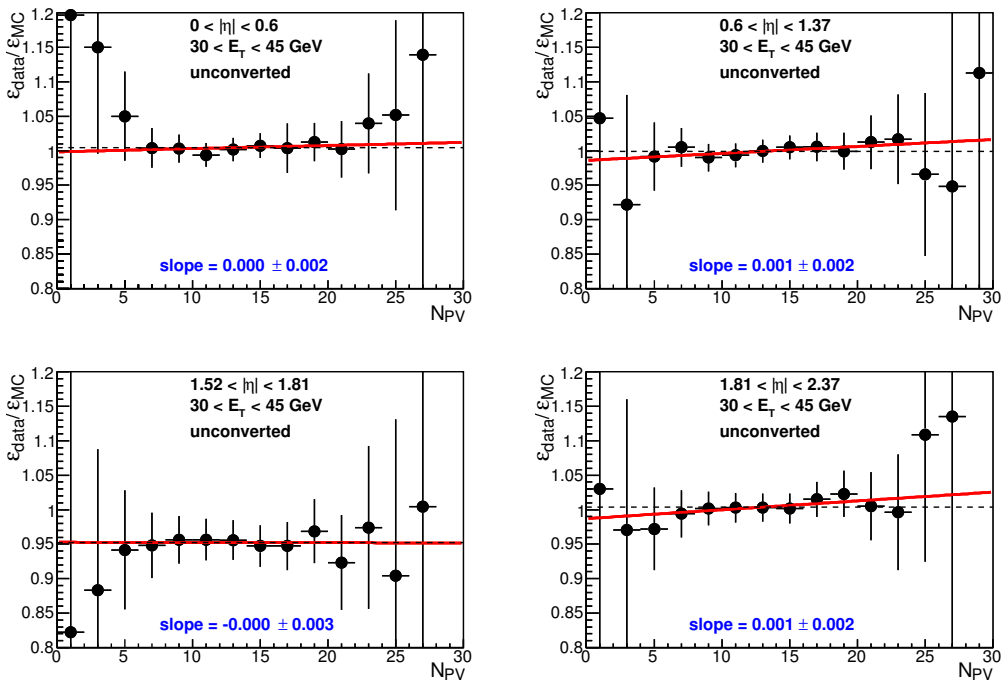

FIGURE 5.30: The measured ratio $\varepsilon_{\text{data}}/\varepsilon_{\text{MC}}$ as a function of N_{PV} for unconverted photons with p_{T} in the range $30\,\text{GeV} < p_{\text{T}} < 45\,\text{GeV}$

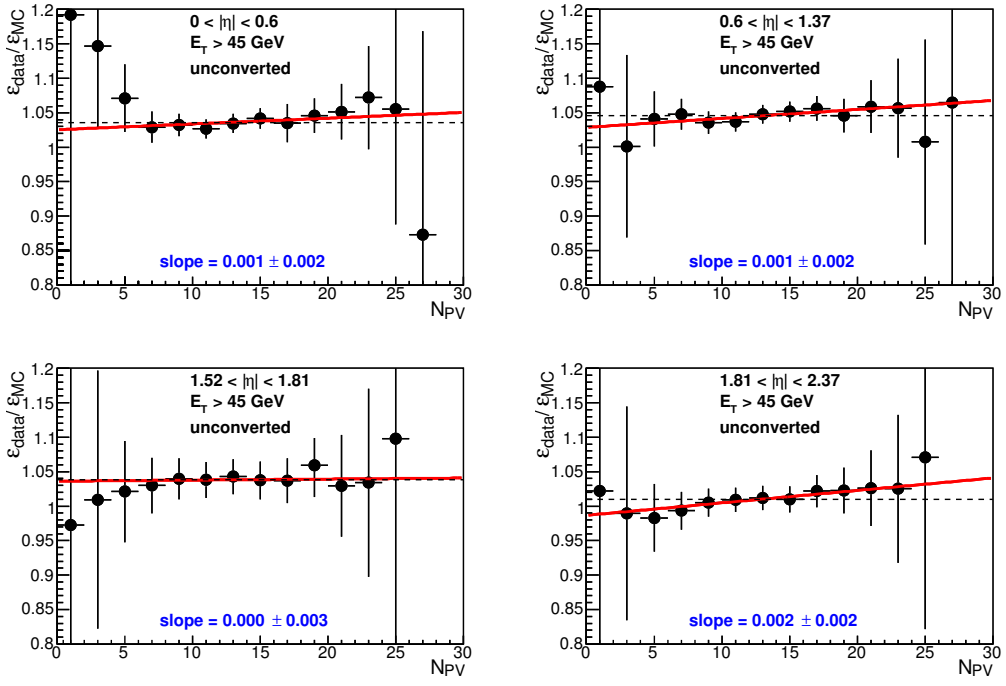

FIGURE 5.31: The measured ratio $\varepsilon_{\text{data}}/\varepsilon_{\text{MC}}$ as a function of N_{PV} for unconverted photons with p_{T} in the range $p_{\text{T}} > 45\,\text{GeV}$

5.8 Combined Measurement of Photon Identification Efficiency

The results presented in section 5.7 are derived entirely from the electron extrapolation study described within this chapter. The final recommendation for how photon identiciation efficiency and its associated uncertainties should be treated by teams working on analyses using the ATLAS detector is dependent not only upon this method, but derives from a combination of the electron extrapolation method and two others (the *Radiative Z* analysis and the *Matrix Method* analysis).

5.8.1 The Radiative Z Analysis

The Radiative Z analysis[77] uses a sample of photons selected from radiative Z boson decays to measure the photon efficiency within the range 10 GeV$< p_T <$80 GeV. The $Z \to e^+e^-$ channel and the $Z \to \mu^+\mu^-$ channel are both used, and are treated independently. To avoid biasing the shower shape distributions of the selected photon sample, the selection does not place tight cuts on the photon candidates. Photon candidates are required to have a reconstructed transverse energy of at least 10 GeV, and a pseudorapidity within the region $|\eta| < 2.37$, excluding the crack region $1.37 < |\eta| < 1.52$. An isolation cut of 4 GeV within a radius $\Delta R = 0.4$ is applied, as in the electron extrapolation study. To ensure a high purity, tighter requirements are placed upon the properties of the leptons, and the invariant masses of the di-lepton and $\ell\ell\gamma$ system.

The efficiency is determined as

$$\varepsilon_{\text{tight}} = \frac{N_{\text{probes,tight}}}{N_{\text{probes}}}, \tag{5.2}$$

where $N_{\text{probes,tight}}$ is the number of selected photons which pass the tight identification criteria, and N_{probes} is the total number of all selected photons. This is a valid approximation if the background contamination in the photon sample is negligible. The background contamination contained within the selected photon sample varies with transverse energy, but is estimated to be approximately 2% in the high-p_T region and as much as 10% in the lowest p_T region for which the method used. This background contamination is dominated by $Z+\text{jets}$ events in which a jet is misidentified as a photon. The effect of the background contamination on the photon identification efficiency measurement is corrected for with a background subtraction method based on template fis to the $m_{\ell\ell\gamma}$ distribution using signal and $Z+\text{jets}$ templates from simulated data. For each p_T, η point, a systematic uncertainty is assigned equal to the difference between the identification efficiencies measured with and without background subtraction. Another possible source of systematic uncertainty is the choice of ΔR_{min} (the minimum permitted ΔR between the photon candidate and the leptons in the event). A check is performed by varying the value of ΔR_{min} used in the event selection, and the measured photon identification efficiency is found to be independent of the chosen ΔR_{min} requirement.

5.8.2 The Matrix Method

The Matrix Method analysis[78] uses track isolation as a discriminating variable to determine the purity of a selected photon sample both before and after applying tight photon identification cuts. Track isolation is defined as the sum of p_T of tracks within a cone $\Delta R < 0.4$ surrounding the photon, subtracting the energy deposits within a cone $\Delta R < 0.1$. The study uses an inclusive photon sample selected with single photon triggers. Like the other photon identification efficiency measurements, a calorimeter isolation cut is placed at 4 GeV. The Matrix Method

provides photon identification efficiency measurement over the transverse energy in the range $20\,\mathrm{GeV} < p_T < 1500\,\mathrm{GeV}$.

The number of selected photon candidates which pass (or fail) the tight photon identification requirements can be expressed in terms of the signal and background fraction among the photon candidates which pass (or fail) those requirements. The total number N^T_{all} of selected photon candidates consists of N^S_{all} true prompt photons and N^B_{all} photon candidates resulting from background events. The number N^T_{pass} of selected photon candidates which pass the tight photon identification requirements likewise consists of N^S_{pass} true prompt photons which pass the identification requirements and N^B_{pass} photon candidates resulting from background events, which nevertheless pass the tight identification requirements. The tight identification efficiency for photons can be written:

$$\varepsilon_{\mathrm{tight}} = \frac{N^S_{\mathrm{pass}}}{N^S_{\mathrm{all}}}\,. \tag{5.3}$$

The signal purity of the inclusive photon sample is given by:

$$P_{\mathrm{all}} \equiv \frac{N^S_{\mathrm{all}}}{N^T_{\mathrm{all}}}\,, \tag{5.4}$$

and the purity of the photon candidates passing the tight photon identification requirements by:

$$P_{\mathrm{pass}} \equiv \frac{N^S_{\mathrm{pass}}}{N^T_{\mathrm{pass}}}\,. \tag{5.5}$$

From equations 5.3–5.5, another expression for the tight identification efficiency for photons can be derived:

$$\varepsilon_{\text{tight}} = \frac{P_{\text{pass}}\, N^T_{\text{pass}}}{P_{\text{all}}\, N^T_{\text{all}}}\,. \tag{5.6}$$

The quantities $N^S_{\text{all}}, N^S_{\text{pass}}, N^B_{\text{all}}$, and N^B_{pass} (and thus the purities P_{pass} and P_{all}) are estimated using the track isolation as a discriminating variable. If $\varepsilon^S_{\text{pass}}$ and $\varepsilon^B_{\text{pass}}$ respectively denote the track isolation efficiencies for prompt photons which pass the tight photon identification requirements and for background photon candidates which pass the tight photon identification requirements, and $\varepsilon^S_{\text{all}}$ and $\varepsilon^B_{\text{all}}$ denote respectively the track isolation efficiency for all prompt photons and the track isolation efficiency for all photon candidates resulting from background events, then the relations:

$$N^{\text{Iso}}_{\text{pass}} = \varepsilon^S_{\text{pass}} N^S_{\text{pass}} + \varepsilon^B_{\text{pass}} N^B_{\text{pass}}\,, \tag{5.7}$$

$$N^{\text{Iso}}_{\text{all}} = \varepsilon^S_{\text{all}} N^S_{\text{all}} + \varepsilon^B_{\text{all}} N^B_{\text{all}} \tag{5.8}$$

can be deduced, where $N^{\text{Iso}}_{\text{pass}}$ denotes the number of selected photon candidates which pass both the tight photon identification requirements and the track isolation requirement, and $N^{\text{Iso}}_{\text{all}}$ denotes the total number of selected photon candidates which pass the track isolation requirement. If the efficiency terms in equations (5.7) and (5.8) are known, then N^S_{pass} and N^S_{all} may be determined from data using the observable quantites $N^T_{\text{all}}, N^{\text{Iso}}_{\text{all}}, N^T_{\text{pass}}$, and $N^{\text{Iso}}_{\text{pass}}$:

$$N^S_{\text{pass}} = \frac{N^{\text{Iso}}_{\text{pass}} - \varepsilon^B_{\text{pass}} N^T_{\text{pass}}}{\varepsilon^S_{\text{pass}} - \varepsilon^B_{\text{pass}}}\,, \tag{5.9}$$

$$N^S_{\text{all}} = \frac{N^{\text{Iso}}_{\text{all}} - \varepsilon^B_{\text{all}} N^T_{\text{all}}}{\varepsilon^S_{\text{all}} - \varepsilon^B_{\text{all}}}\,. \tag{5.10}$$

By introducing the identities $\varepsilon_{\text{pass}} \equiv \frac{N^{\text{Iso}}_{\text{pass}}}{N^{T}_{\text{pass}}}$ and $\varepsilon_{\text{all}} \equiv \frac{N^{\text{Iso}}_{\text{all}}}{N^{T}_{\text{all}}}$, it is possible to deduce new expressions for P_{pass} and P_{all}:

$$P_{\text{pass}} = \frac{\varepsilon_{\text{pass}} - \varepsilon^{B}_{\text{pass}}}{\varepsilon^{S}_{\text{pass}} - \varepsilon^{B}_{\text{pass}}}\,, \tag{5.11}$$

$$P_{\text{all}} = \frac{\varepsilon_{\text{all}} - \varepsilon^{B}_{\text{all}}}{\varepsilon^{S}_{\text{all}} - \varepsilon^{B}_{\text{all}}}\,, \tag{5.12}$$

and so to rewrite equation (5.6):

$$\varepsilon_{\text{tight}} = \frac{\left(\frac{\varepsilon_{\text{pass}} - \varepsilon^{B}_{\text{pass}}}{\varepsilon^{S}_{\text{pass}} - \varepsilon^{B}_{\text{pass}}}\right) N^{T}_{\text{pass}}}{\left(\frac{\varepsilon_{\text{all}} - \varepsilon^{B}_{\text{all}}}{\varepsilon^{S}_{\text{all}} - \varepsilon^{B}_{\text{all}}}\right) N^{T}_{\text{all}}} \tag{5.13}$$

The quantities $\varepsilon_{\text{pass}}$, ε_{all}, N^{T}_{pass}, and N^{T}_{all} can be directed measured from data. The track isolation efficiencies for true prompt photons ($\varepsilon^{S}_{\text{all}}$ and $\varepsilon^{S}_{\text{pass}}$) are estimated from MC data. The accuracy of this estimation is validated by comparing the track isolation efficiency for electrons selected with a tag-and-probe $Z \to e^{+}e^{-}$ study on both real and simulated data. The average difference between data and MC is applied as a systematic uncertainty on each value. The track isolation efficiencies ($\varepsilon^{B}_{\text{all}}$ and $\varepsilon^{B}_{\text{pass}}$) for photon candidates resulting from background events are estimated from data, using a background-enriched sample selected by reversing selection cuts on some shower shape variables. The variables $F_{\text{side}}, w_{s,3}, \Delta E$, and E_{ratio} are chosen as they are not strongly correlated with track isolation. As no photon candidate can pass the tight photon identification requirements while also passing the reversed cuts on these selected variables, the selected variables are removed from the tight identification criteria. Due to the lack of any strong correlation between the selected variables and track identification, this is not believed to bias the estimate of track isolation efficiency.

5.8.3 Scale Factors

In addition to the direct measurement of photon identification efficiency, each of the three analyses produces a set of *scale factors* which can be applied to MC samples to correct for the difference between efficiencies measured in data and in MC. These scale factors are computed in the same p_{T}, η binning as used for the efficiency measurement, and are defined as:

$$\mathrm{SF} = \frac{\varepsilon_{\mathrm{data}}}{\varepsilon_{\mathrm{MC}}}\,, \tag{5.14}$$

where $\varepsilon_{\mathrm{data}}$ and $\varepsilon_{\mathrm{MC}}$ denote the identification efficiencies measured in data and MC respectively.

For each analysis, the statistical uncertainty is calculated as:

$$\frac{\sigma_{\mathrm{SF,stat}}}{SF} = \sqrt{\left(\frac{\sigma_{\varepsilon_{\mathrm{data,stat}}}}{\varepsilon_{\mathrm{data}}}\right)^2 + \left(\frac{\sigma_{\varepsilon_{\mathrm{MC,stat}}}}{\varepsilon_{\mathrm{MC}}}\right)^2}\,, \tag{5.15}$$

and the systematic uncertainty as:

$$\frac{\sigma_{\mathrm{SF,syst,i}}}{\mathrm{SF}} = \frac{\sigma_{\varepsilon_{\mathrm{data,syst,i}}}}{\varepsilon_{\mathrm{data}}}\,, \tag{5.16}$$

where i denotes each source of systematic uncertainty considered for the analysis.

5.8.4 Combination Method

The results of all analyses are combined[1] into a final measurement using the Best Linear Unbiased Estimate (*BLUE*) method[79]. In BLUE, the combined measurement is determined as the linear combination of the contributing measurements,

weighting with coefficients which are determined by minimising the total uncertainty on the combined measurement. The method allows for a combination of N measurements of a quantity, accounting for correlations between uncertainties. All uncertainties are assumed to be distributed according to a Gaussian probability function. The combination of n measurements of some quantity, x_i, begins by defining the covariance matrix, V_x:

$$(V_x)_{ij} = \langle \delta x_i \delta x_j \rangle \,, \tag{5.17}$$

where $\delta x_i = x_i - \bar{x}_i$. The correlation coefficients between the uncertainties, σ_i, on the measurements of x_i are written:

$$\rho_{ij} = \frac{(V_x)_{ij}}{\sigma_i \sigma_j} \,. \tag{5.18}$$

The best linear estimator is defined:

$$\bar{x} = \sum_i \omega_i x_i \,, \tag{5.19}$$

where

$$\omega_i = \frac{\sum_k (V_x^{-1})_{ik}}{\sum_{jk} (V_x^{-1})_{jk}} \,, \tag{5.20}$$

and the uncertainty on $\bar{x}$ is thus defined as:

$$\sigma_{\bar{x}}^2 = \sum_{ij} \omega_i \omega_j \, (V_x)_{ij} \tag{5.21}$$

In the photon identification efficiency measurement, four sources of uncertainty are considered. Some exist for all measurements, while others exist only on a subset of the available measurements. The sources, and measurements for which each source is considered, are:

- Statistical uncertainty (all measurements),
- Background-related uncertainty (all measurements),
- Material-related uncertainty (Electron Extrapolation and Matrix Method), and
- Closure test (Electron extrapolation only).

At each η, p_{T} point, the χ^2 value is calculated as $\chi^2 = \Sigma\omega_i \left(\bar{\mathrm{SF}} - \mathrm{SF}_i\right)^2$. The expected value of χ^2 for any given point is $N-1$, where N is the number of measurements combined for that point. Where $\chi^2/(N-1) \leq 1$, the uncertainty remains as calculated above. Where $\chi^2/(N-1) > 1$, the uncertainty on the combined value is increased by a factor of $\sqrt{\chi^2/(N-1)}$.

5.8.4.1 Correlations between measurements

The measurements of photon identification efficiency produced by different methods are all considered to be uncorrelated, with the exception of the electron and muon channels of the Radiative Z method. The background-related uncertainties of the two Radiative Z analysis channels are considered to be 100% correlated with each other. Initially the material-related uncertainties from the Electron Extrapolation and Matrix Method analyses were considered to be 100% correlated with each other, but this was treatment was rejected as it produced unphysical effects when combining the measurements. These effects resulted from a large discrepancy in the size of the uncertainty on each analysis, which led to the BLUE combination method determining large, negative weights for the Electron Extrapolation measurement in some data points. This ultimately resulted in combined efficiency measurements for some p_{T}, η bins which were smaller than any individual measurement. As such, this treatment was considered unsatisfactory. Ultimately, the two sources of uncertainty were considered to be uncorrelated in the final

measurement. Though both studies use the same MC samples to measure this uncertainty, the effect comes from different sources (in the Electron Extrapolation study, the source of the uncertainty is dominated by the distortion of shower shapes and the resultant effect on Smirnov transformations; in the Matrix Method study the uncertainty is dominated by the change to track isolation). As the two material-related uncertainties result from different effects, and also contain some statistical component, it is considered safe to assume they are not correlated.

5.8.4.2 Effect of fragmentation photons

As discussed in section 5.7.2, if the fraction of so-called *fragmentation photons* is not correctly modelled in MC samples then a bias may be introduced into the measured photon identification efficiency. This was evaluated section 5.7.2 using the Electron Extrapolation method and found to be a small effect, but was not applied as a systematic uncertainty. The combined measurement does include a systematic uncertainty to account for this effect, based on an evaluation using the Matrix Method. The extent is estimated by varying the fraction of fragmentation photons within MC samples, and observing the effect on the efficiency. The method is similar to that described in section 5.7.2. Two variations on the MC sample are used. In one, the fragmentation photons are either removed entirely. In the other, they are weighted more heavily so as to double the fraction of fragmentation photons in the sample. For each $p_{\mathrm{T}}, |\eta|$ bin, the difference between the nominal efficiency measurement and the efficiency measurement using the MC sample with each fragmentation fraction variation is measured. The assigned uncertainty is based on whichever variation produces the largest difference. As the convention within ATLAS Standard Model analysis groups is to vary the fragmentation fraction by factors of 0.5 and 1.5 (rather than the 0 and 2 used here), the uncertainty is then divided by a factor of 2.

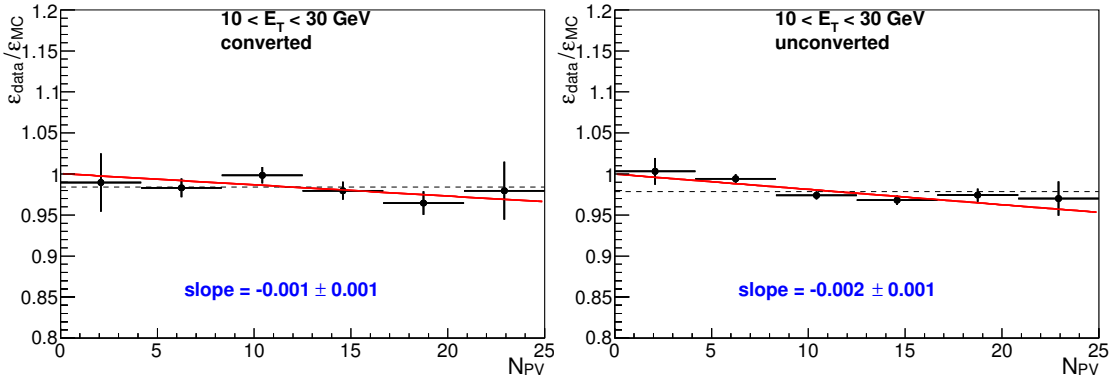

(a) (b)

FIGURE 5.32: The measured ratio $\varepsilon_{\text{data}}/\varepsilon_{\text{MC}}$ as a function of N_{PV} for converted ((a)) and unconverted ((b)) photons with p_{T} in the range $10\,\text{GeV} < p_{\text{T}} < 30\,\text{GeV}$

Due to the limitated statistics of the MC sample, some non-negligible statistical variation is expected between p_{T} bins. To reduce this and avoid undesirable fluctuations, a smoothing is applied to each $p_{\text{T}}, |\eta|$ bin by taking a weighted average with the immediately higher and immediately lower p_{T} bins in that same $|\eta|$ region, weighted by their statistical uncertainty.

5.8.4.3 PILEUP DEPENDENCE

The effect of pileup on photon identification efficiency was discussed in section 5.7.3 in the context of the Electron Extrapolation measurement. The Electron Extrapolation measurement provided an estimate of the extent of this effect for two p_{T} regions ($30\,\text{GeV} < p_{\text{T}} < 45\,\text{GeV}, p_{\text{T}} > 45\,\text{GeV}$) in four pseudorapidity bins, finding no statistically significant dependence of photon identification efficiency on pileup. This effect is also studied in the low p_{T} region $10\,\text{GeV} < p_{\text{T}} < 30\,\text{GeV}$, using Radiative Z events, integrated in η due to low statistics. The results are shown in figure 5.32 for both converted and unconverted photons. No statistically significant dependence of photon identification efficiency on pileup is observed.

5.8.4.4 Results of Combination

The inputs to the combined measurement are shown in the form of efficiencies in figures 5.33 and 5.34 for converted and unconverted photons respectively, and in the form of scale factors in figures 5.35 and 5.36, alongside the results of the combination. The results of the combination are shown individually in figures 5.37 and 5.38. The error bars in these plots indicate the quadratic sum of statistical and systematic errors, and are not necessarily equivalent to the uncertainties on the final combination result. As described in section 5.8.4, a χ^2 test is applied to the result of the combination, and uncertainties are inflated on points where $\chi^2/(N-1) > 1$. This test is shown for converted and unconverted photons in figures 5.39 and 5.40. The final fractional uncertainty on the scale factor in each $p_{\mathrm{T}}, |\eta|$ bin of the combined measurement is shown in figures 5.41 and 5.42 for converted and unconverted photons respectively, along with a comparison to the uncertainties on the previous preliminary recommendation presented at the 2013 Moriond conference.

5.9 Conclusions

The majority of this chapter presents a data-driven determination of photon ID efficiency using $21\,\mathrm{fb}^{-1}$ of data at $\sqrt{s} = 8\,\mathrm{TeV}$. The efficiency measurement uses Smirnov transformations to extract a photon ID efficiency measurement from electrons in data, selected in a tag and probe $Z \to e^+e^-$ analysis. The study is performed in the range $30\,\mathrm{GeV} < p_{\mathrm{T}} < 100\,\mathrm{GeV}$ for $|\eta| < 2.37$, excluding the region $1.37 < |\eta| < 2.37$.

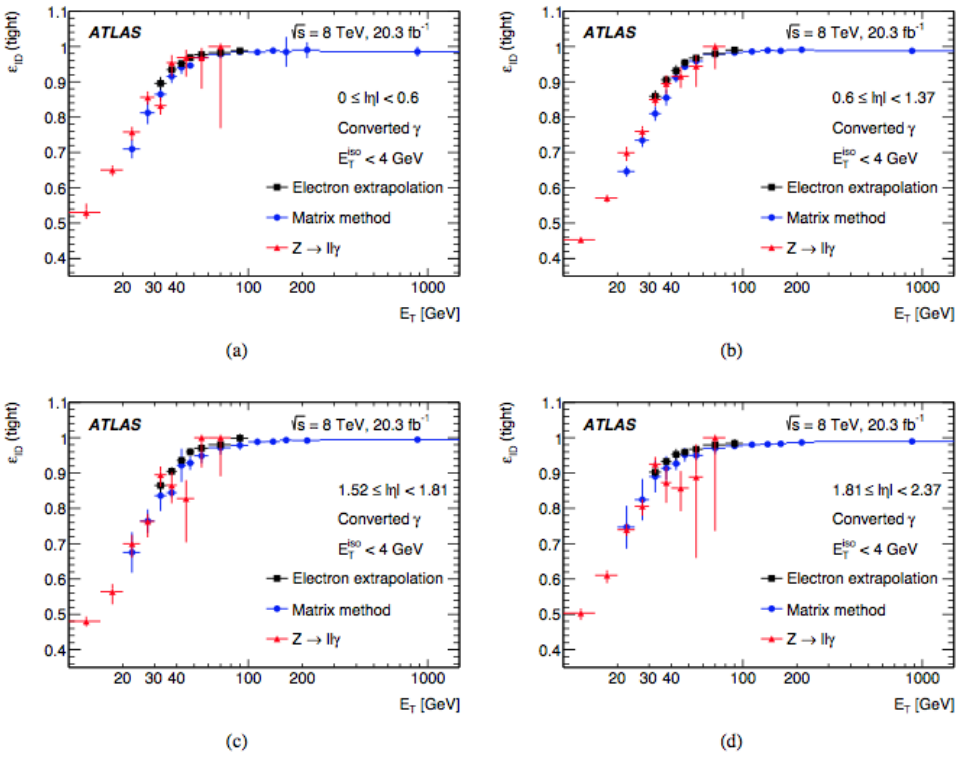

FIGURE 5.33: Converted photon identification efficiency as measured by each of the analyses used as input for the combination, across the p_{T} range $10\,\mathrm{GeV} < p_{\mathrm{T}} < 1 \times 10^{3}\,\mathrm{GeV}$ in four $|\eta|$ regions. The error bars indicate the quadratic sum of the statistical and systematic uncertainties.

Systematic unertainties are assigned to account for uncertainty inherent in the Smirnov transform method, and for possible inaccuracies of the Monte Carlo samples used in the study. For converted photons, the total uncertainty on the efficiency measurement is typically around 3% or below, and in all cases is below 5%. Uncertainties for unconverted photons are slightly larger, but do not exceed 6% within the $p_{\mathrm{T}}, |\eta|$ range studied.

The data-driven efficiency measurement is compared to the efficiency observed in Monte Carlo samples with *fudge factors* applied to the simulated shower shapes. The efficiencies from this corrected simulation generally agree with the data-driven measurement to within 2%, though some larger discrepancy is seen in a low p_{T} region for unconverted photons, where the maximum difference is approximately 6%. The simulation of pileup effects on photon identification efficiency appears

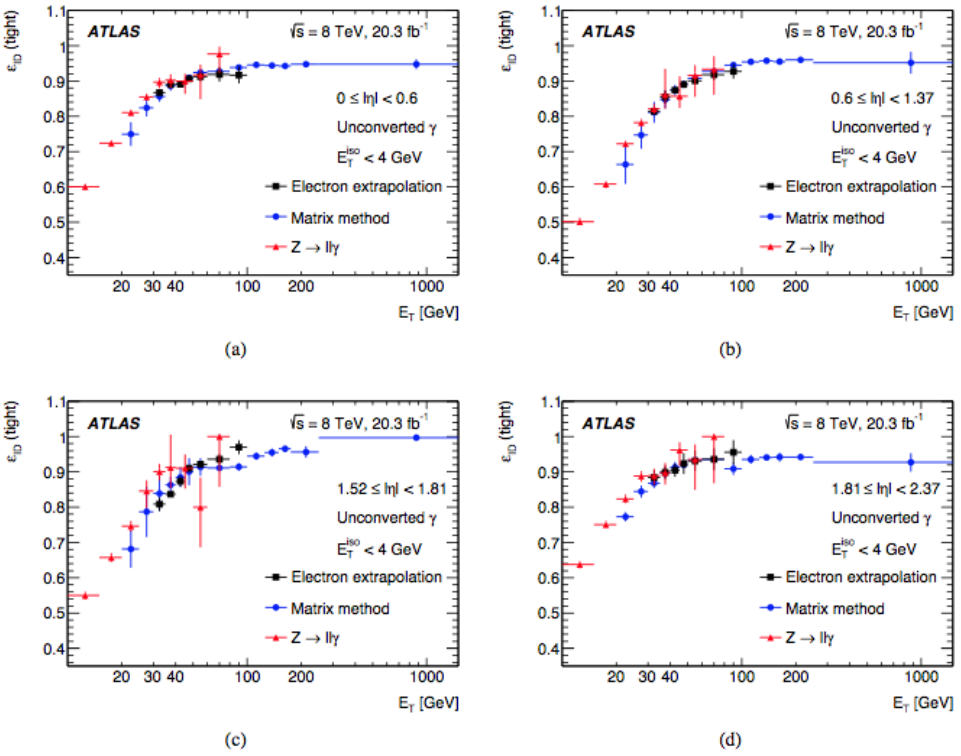

FIGURE 5.34: Unconverted photon identification efficiency as measured by each of the analyses used as input for the combination, across the p_{T} range $10\,\mathrm{GeV} < p_{\mathrm{T}} < 1 \times 10^3\,\mathrm{GeV}$ in four $|\eta|$ regions. The error bars indicate the quadratic sum of the statistical and systematic uncertainties.

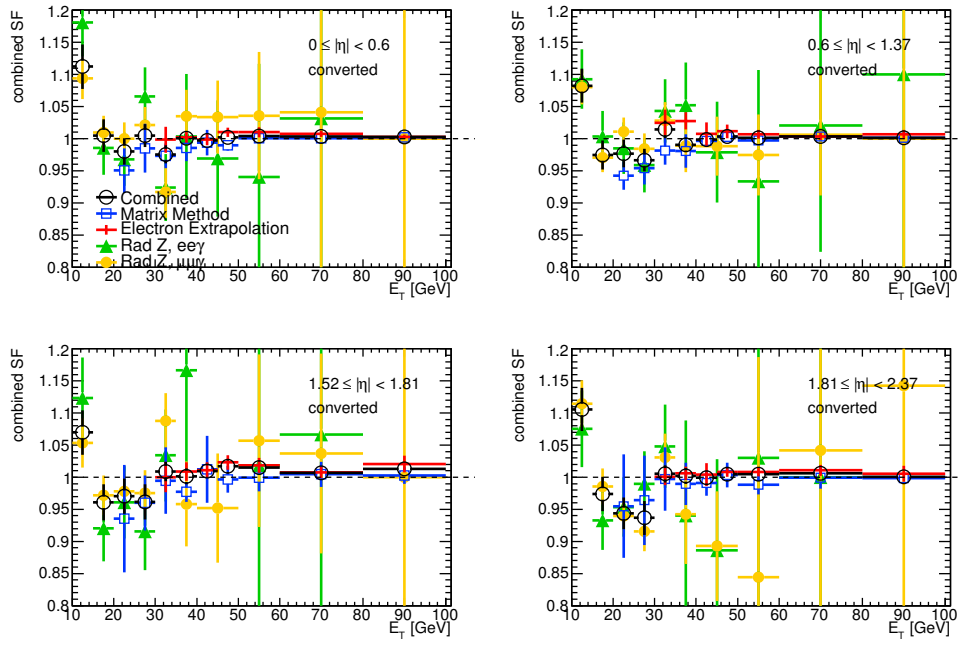

FIGURE 5.35: Converted photon identification efficiency scale factors calculated by each analysis, and the results of the combination, across the p_{T} range $10\,\mathrm{GeV} < p_{\mathrm{T}} < 100\,\mathrm{GeV}$. The error bars indicate the quadratic sum of the statistical and systematic uncertainties.

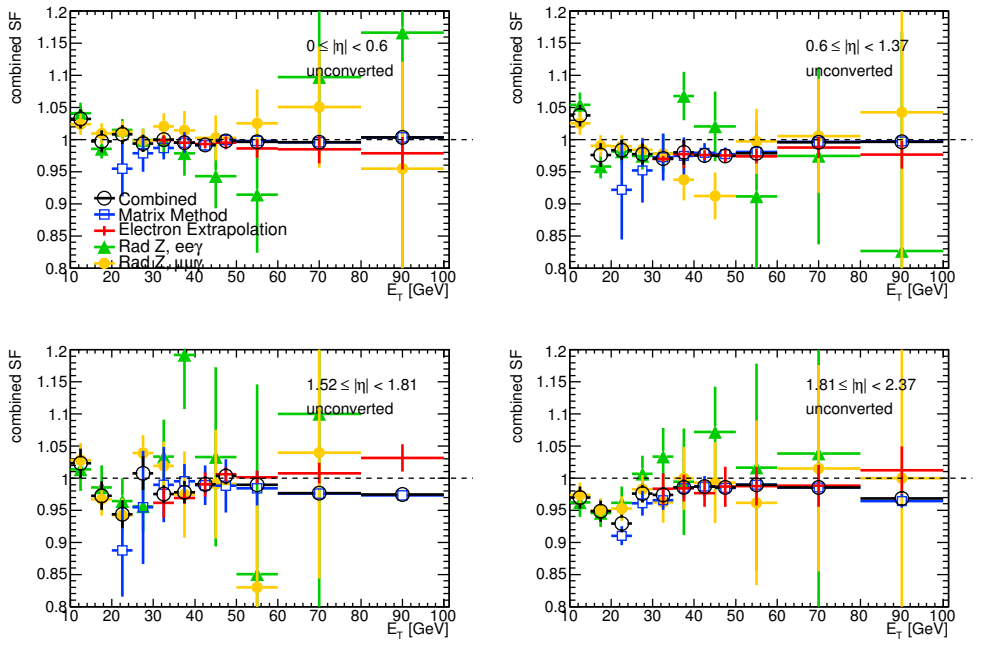

FIGURE 5.36: Unconverted photon identification efficiency scale factors calculated by each analysis, and the results of the combination, across the p_{T} range $10\,\mathrm{GeV} < p_{\mathrm{T}} < 100\,\mathrm{GeV}$ in 4 $|\eta|$ bins. The error bars indicate the quadratic sum of the statistical and systematic uncertainties.

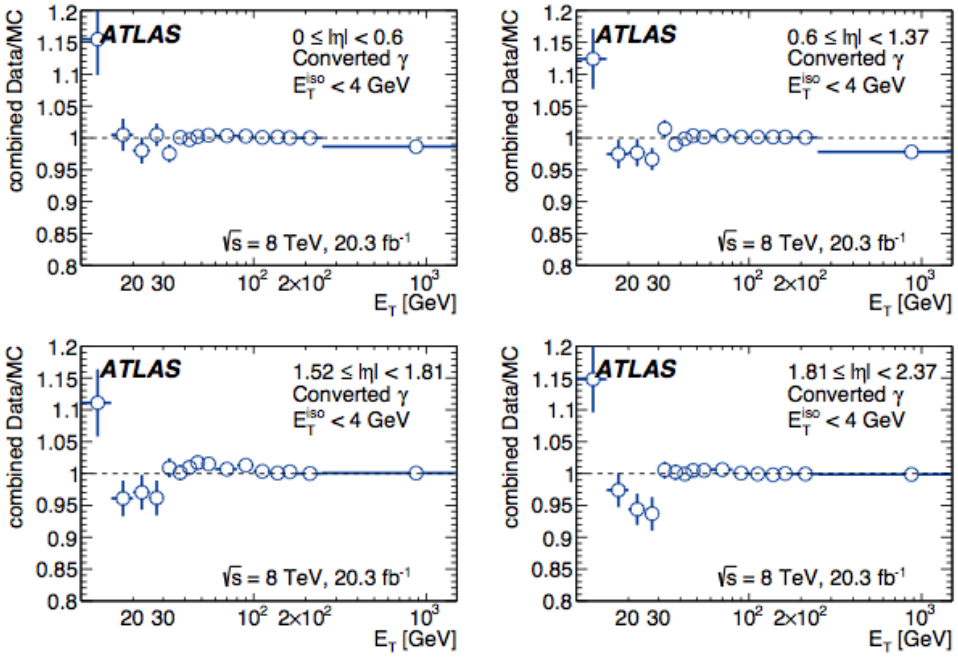

FIGURE 5.37: Photon efficiency scale factors for converted photons resulting from the combination of all analyses in the p_{T} region $10\,\mathrm{GeV} < p_{\mathrm{T}} < 1 \times 10^3\,\mathrm{GeV}$ in four $|\eta|$ regions. The error bars represent the quadratic sum of the statistical and systematic uncertainties.

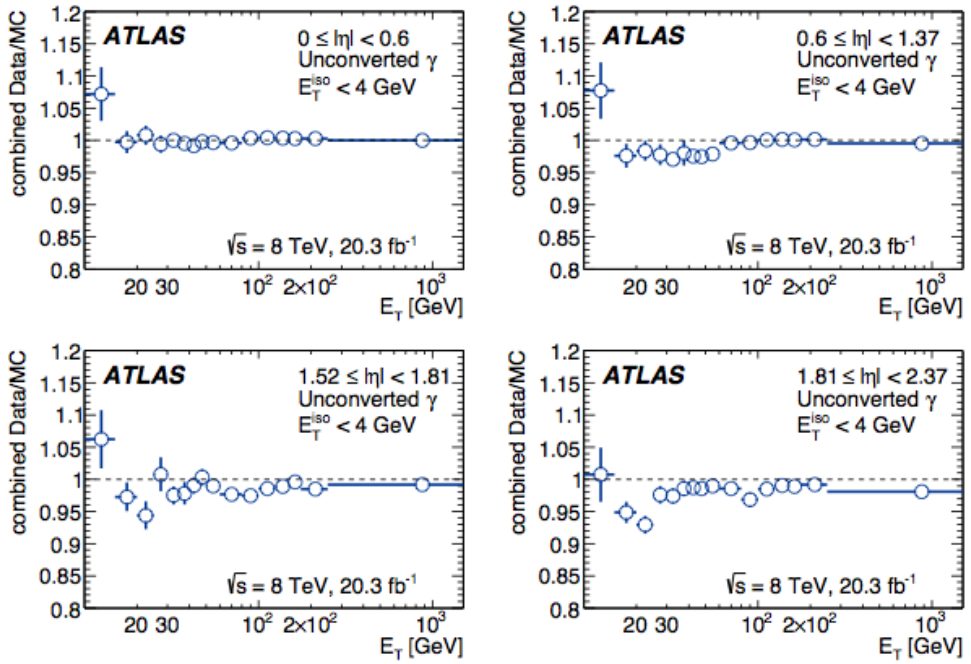

FIGURE 5.38: Photon efficiency scale factors for unconverted photons resulting from the combination of all analyses in the p_{T} region $10\,\mathrm{GeV} < p_{\mathrm{T}} < 1 \times 10^3\,\mathrm{GeV}$ in four $|\eta|$ regions. The error bars represent the quadratic sum of the statistical and systematic uncertainties.

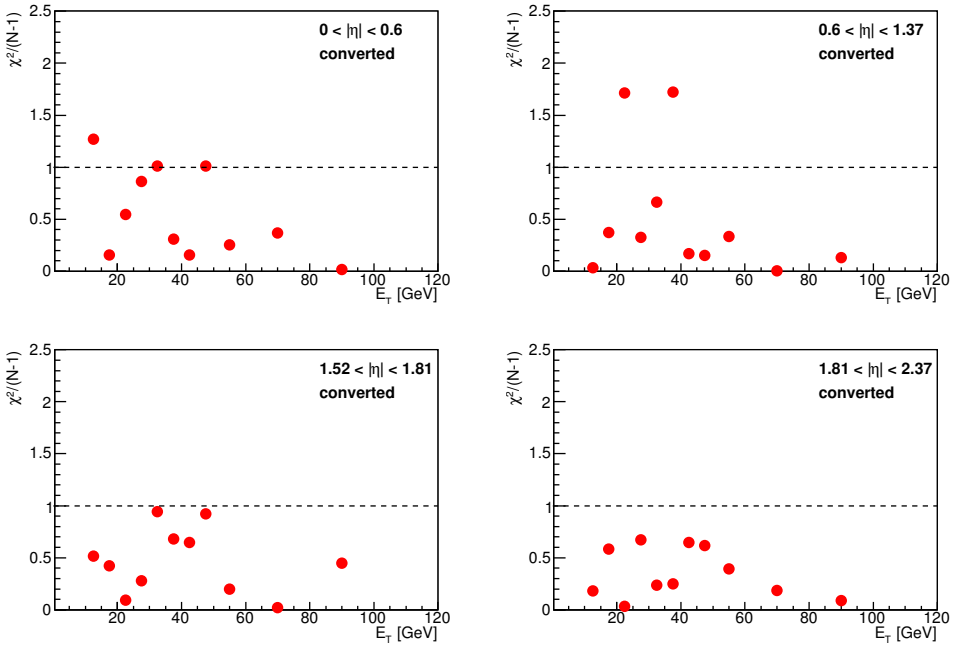

FIGURE 5.39: These plots show the value of $\chi^2\,(N-1)$ calculated as a compatiblity test for the combined photon identification efficiency study for converted photons in four $|\eta|$ regions.

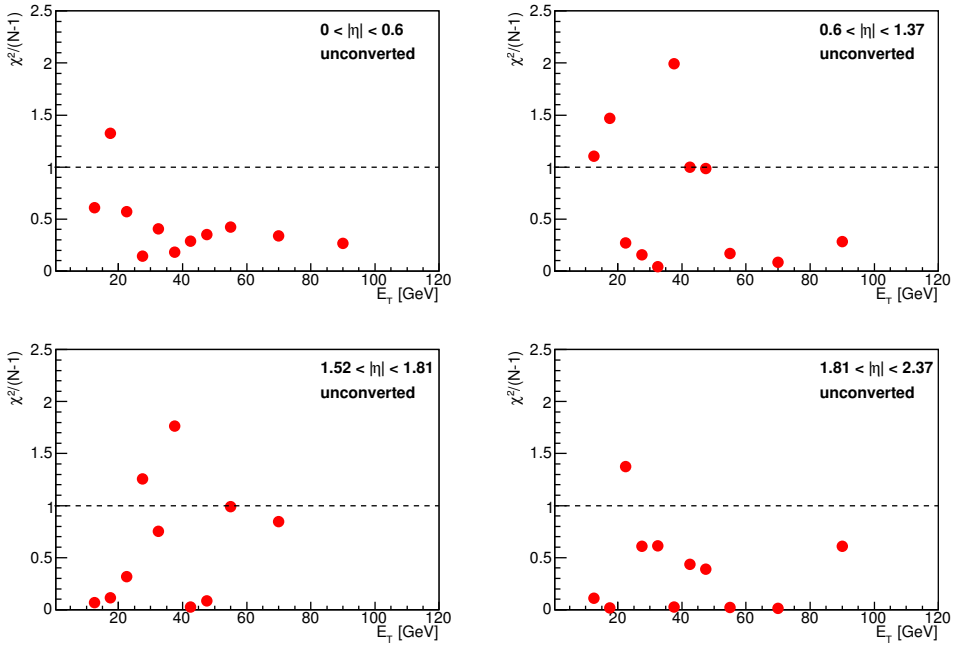

FIGURE 5.40: These plots show the value of $\chi^2\,(N-1)$ calculated as a compatiblity test for the combined photon identification efficiency study for unconverted photons in four $|\eta|$ regions.

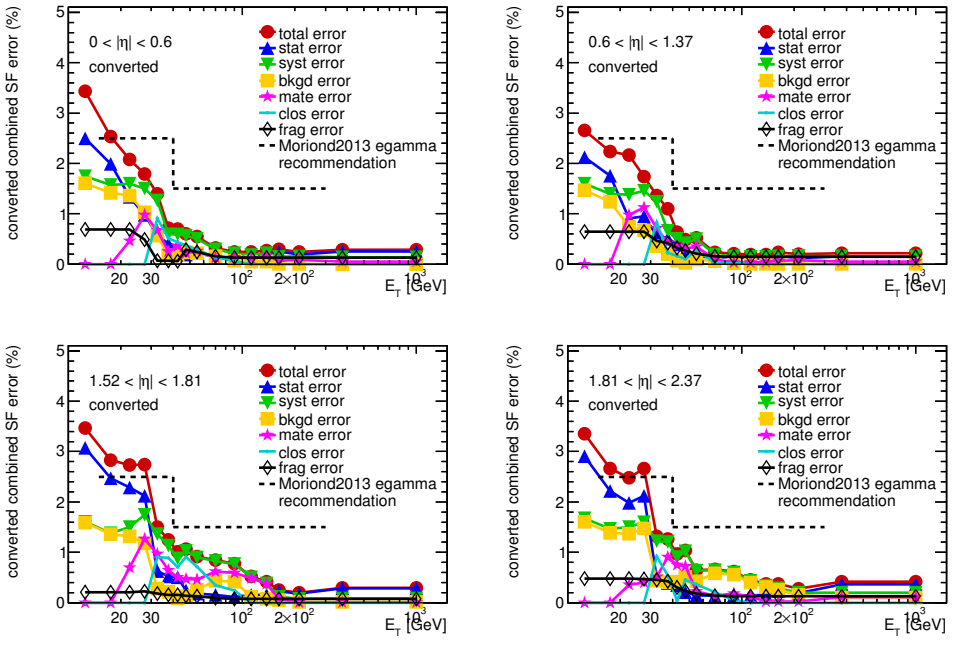

FIGURE 5.41: These plots show the final uncertainties on the combined scale factors for converted photons in four $|\eta|$ regions. Also shown is the contribution from each individual source of uncertainty. For comparison purposes, the plots also show the uncertainties from the previous preliminary recommendation.

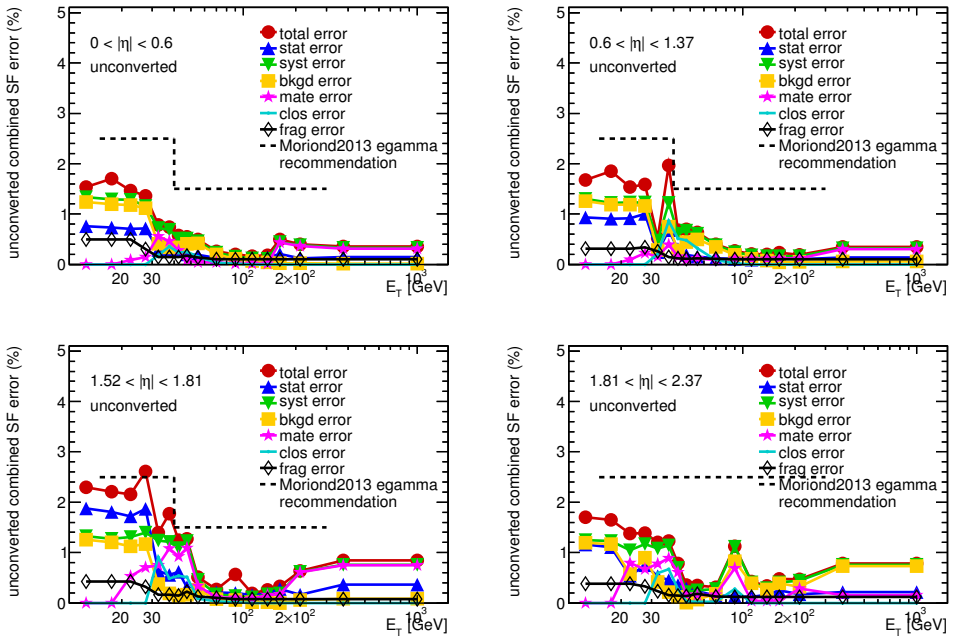

FIGURE 5.42: These plots show the final uncertainties on the combined scale factors for unconverted photons in four $|\eta|$ regions. Also shown is the contribution from each individual source of uncertainty. For comparison purposes, the plots also show the uncertainties from the previous preliminary recommendation.

to reproduce well what is observed in data. Tables 5.5 and 5.6 show the identification efficiency (as measured by the Electron Extrapolation method), with combined statistical and systematic errors, for converted and unconverted photons respectively.

The final section of this chapter also presents an overview of two other methods which are used to provide data-driven measurements of photon identification efficiency at p_{T} ranges higher and lower than accessible via the Electron Extrapolation method, and the process by which the three methods are combined to produce a final recommendation for the treatment of photon identification efficiency and related uncertainties by analysis groups within the ATLAS experiment.

$\lvert\eta\rvert, p_{\mathrm{T}}$ (GeV)	efficiency (%)	$\pm$	$\sqrt{\sigma^2_{stat} + \sigma^2_{syst.}}$
$0.00 \leq \lvert\eta\rvert < 0.60$			
$30 \leq p_{\mathrm{T}} < 35$	89.4	$\pm$	2.0
$35 \leq p_{\mathrm{T}} < 40$	93.4	$\pm$	1.7
$40 \leq p_{\mathrm{T}} < 45$	95.2	$\pm$	1.5
$45 \leq p_{\mathrm{T}} < 50$	96.8	$\pm$	1.6
$50 \leq p_{\mathrm{T}} < 60$	97.6	$\pm$	1.7
$60 \leq p_{\mathrm{T}} < 80$	98.1	$\pm$	2.0
$80 \leq p_{\mathrm{T}} < 1000$	98.8	$\pm$	2.8
$0.60 \leq \lvert\eta\rvert < 1.37$			
$30 \leq p_{\mathrm{T}} < 35$	85.7	$\pm$	2.1
$35 \leq p_{\mathrm{T}} < 40$	90.4	$\pm$	1.7
$40 \leq p_{\mathrm{T}} < 45$	93.1	$\pm$	1.6
$45 \leq p_{\mathrm{T}} < 50$	95.4	$\pm$	1.7
$50 \leq p_{\mathrm{T}} < 60$	96.5	$\pm$	1.8
$60 \leq p_{\mathrm{T}} < 80$	97.6	$\pm$	2.1
$80 \leq p_{\mathrm{T}} < 100$	98.6	$\pm$	3.0
$1.52 \leq \lvert\eta\rvert < 1.81$			
$30 \leq p_{\mathrm{T}} < 35$	86.2	$\pm$	2.8
$35 \leq p_{\mathrm{T}} < 40$	90.3	$\pm$	2.5
$40 \leq p_{\mathrm{T}} < 45$	93.5	$\pm$	2.3
$45 \leq p_{\mathrm{T}} < 50$	95.8	$\pm$	2.4
$50 \leq p_{\mathrm{T}} < 60$	96.8	$\pm$	2.6
$60 \leq p_{\mathrm{T}} < 80$	97.5	$\pm$	3.2
$80 \leq p_{\mathrm{T}} < 100$	99.1	$\pm$	4.0
$1.81 \leq \lvert\eta\rvert < 2.37$			
$30 \leq p_{\mathrm{T}} < 35$	90.0	$\pm$	2.4
$35 \leq p_{\mathrm{T}} < 40$	93.1	$\pm$	2.2
$40 \leq p_{\mathrm{T}} < 45$	95.0	$\pm$	2.1
$45 \leq p_{\mathrm{T}} < 50$	95.7	$\pm$	2.4
$50 \leq p_{\mathrm{T}} < 60$	96.3	$\pm$	2.8
$60 \leq p_{\mathrm{T}} < 80$	97.2	$\pm$	3.6
$80 \leq p_{\mathrm{T}} < 100$	97.3	$\pm$	6.2

TABLE 5.5: The measured photon identification efficiency for converted photons in each p_{T}, η bin. The combined statistical and systematic uncertainties are also shown.

$\lvert\eta\rvert, p_{\mathrm{T}}$ (GeV)	efficiency (%)	$\pm$	$\sqrt{\sigma^2_{stat} + \sigma^2_{syst.}}$
$0.00 \leq \lvert\eta\rvert < 0.60$			
$30 \leq p_{\mathrm{T}} < 35$	86.5	$\pm$	2.1
$35 \leq p_{\mathrm{T}} < 40$	88.9	$\pm$	1.8
$40 \leq p_{\mathrm{T}} < 45$	89.0	$\pm$	1.7
$45 \leq p_{\mathrm{T}} < 50$	90.6	$\pm$	1.9
$50 \leq p_{\mathrm{T}} < 60$	91.1	$\pm$	2.2
$60 \leq p_{\mathrm{T}} < 80$	91.6	$\pm$	2.8
$80 \leq p_{\mathrm{T}} < 100$	91.2	$\pm$	4.3
$0.60 \leq \lvert\eta\rvert < 1.37$			
$30 \leq p_{\mathrm{T}} < 35$	81.2	$\pm$	2.1
$35 \leq p_{\mathrm{T}} < 40$	85.4	$\pm$	1.9
$40 \leq p_{\mathrm{T}} < 45$	87.3	$\pm$	1.8
$45 \leq p_{\mathrm{T}} < 50$	88.9	$\pm$	2.0
$50 \leq p_{\mathrm{T}} < 60$	89.9	$\pm$	2.3
$60 \leq p_{\mathrm{T}} < 80$	91.4	$\pm$	2.8
$80 \leq p_{\mathrm{T}} < 100$	91.9	$\pm$	4.4
$1.52 \leq \lvert\eta\rvert < 1.81$			
$30 \leq p_{\mathrm{T}} < 35$	80.6	$\pm$	2.9
$35 \leq p_{\mathrm{T}} < 40$	83.5	$\pm$	2.6
$40 \leq p_{\mathrm{T}} < 45$	87.2	$\pm$	2.5
$45 \leq p_{\mathrm{T}} < 50$	90.9	$\pm$	2.8
$50 \leq p_{\mathrm{T}} < 60$	91.9	$\pm$	3.1
$60 \leq p_{\mathrm{T}} < 80$	92.9	$\pm$	4.0
$80 \leq p_{\mathrm{T}} < 100$	95.8	$\pm$	5.8
$1.81 \leq \lvert\eta\rvert < 2.37$			
$30 \leq p_{\mathrm{T}} < 35$	88.1	$\pm$	2.4
$35 \leq p_{\mathrm{T}} < 40$	89.7	$\pm$	2.3
$40 \leq p_{\mathrm{T}} < 45$	90.2	$\pm$	2.4
$45 \leq p_{\mathrm{T}} < 50$	92.1	$\pm$	2.7
$50 \leq p_{\mathrm{T}} < 60$	92.7	$\pm$	3.3
$60 \leq p_{\mathrm{T}} < 80$	92.8	$\pm$	4.5
$80 \leq p_{\mathrm{T}} < 100$	94.1	$\pm$	7.4

TABLE 5.6: The measured photon identification efficiency for unconverted photons in each p_{T}, η bin. The combined statistical and systematic uncertainties are also shown.

Chapter 6

Higgs p_{T} Spectrum in the $H \to \gamma\gamma$ Channel

The main topic of the chapter is a presentation of a measurement of the Higgs boson differential cross-section in transverse momentum, p_{T}. To provide some context for this measurement, the introductory section of the chapter discusses the initial observation of the Higgs boson by the ATLAS and CMS experiments in 2012, some subsequent measurements and observations of the particle's properties, and the motivation for a measurement of the differential cross-section in p_{T}. A description of the data and simulated data samples used in the analysis is provided, and theoretical expectations are presented. The chapter then presents a description of the methods used in performing the analysis, including event selection, reconstruction, signal and background modelling, and the assessment of systematic uncertainties. The measured differential cross-section in p_{T} is presented. A study is performed to evaluate, based on the measured differential cross-section in p_{T}, the contribution of gluon-gluon fusion to the total Higgs boson production cross-section. This analysis was conducted alongside a similar analysis in another ATLAS study[2], and the evaluation of the effects of many systematic uncertainties

is shared with that study. These shared elements are explicitly noted when discussed through the chapter. Finally, a further study is carried out to estimate the extent to which the uncertainties on this measurement may decrease with larger data samples.

6.1 Observation of the Higgs Boson

On July 4th, 2012, both the ATLAS and CMS experiments announced the observation of a particle with properties consistent with those expected of a Higgs boson[80]. The initial ATLAS observation[13] was based on searches in the $H \to ZZ^{(*)} \to 4\ell$, $H \to \gamma\gamma$, and $H \to WW^{(*)} \to e\nu\mu\nu$ decay channels, using 4.6–4.8 fb^{-1} of $\sqrt{s} = 7\,\mathrm{TeV}$ data recorded in 2011, and 5.8–5.9 fb^{-1} of $\sqrt{s} = 8\,\mathrm{TeV}$ data recorded in 2012. The combined analysis of these channels found an excess of events above the expected background with a local significance of 5.9σ in the mass region 122–131 GeV and a global significance of 5.1σ for the entire 110–600 GeV mass region considered in the search. The first CMS observation[14] was similarly based on a combined Higgs search in multiple decay channels (in this case, the $H \to \gamma\gamma$, $H \to ZZ$, $H \to WW$, $H \to \tau^+\tau^-$, and $H \to b\bar{b}$ channels), using data samples including up to 5.1 fb^{-1} of data taken at $\sqrt{s} = 7\,\mathrm{TeV}$ and 5.3 fb^{-1} of $\sqrt{s} = 8\,\mathrm{TeV}$ data. The combined analysis observed an excess above the expected background with a local significance of 5.0σ for $m_H = 125.5\,\mathrm{GeV}$ (with a global significance for the 110–145 GeV mass range of 4.5σ).

Since these earliest observations, improvements to analyses and additional data have allowed for the mass of the particles to be more precisely measured. A combined analysis of both ATLAS and CMS data in the $H \to \gamma\gamma$ and $H \to ZZ \to 4\ell$ decay channels measured a mass of $125.09 \pm 0.21(\mathrm{stat.}) \pm 0.11(\mathrm{syst.})\,\mathrm{GeV}$. The additional data taken since the first observations has also enabled the first studies of properties of the particle, such as its spin[81, 82] and the strengths of its couplings

to other particles[83, 84]. Many of these early measurements suffer from large uncertainties, but so far such measurements have not produced any surprising results and the observed properties of the particle are consistent with those expected of a Standard Model Higgs boson. Future analyses based on larger datasets, including data taken during 'run 2' of the LHC with an increased centre-of-mass energy, will allow for even more precise measurements of this particle's properties and to better ascertain its compatibility with the predictions of the Standard Model.

6.2 The $H \to \gamma\gamma$ Decay Channel

As described in section 2.2.2, the decay of the Higgs boson to two photons occurs indirectly via particle loops, with contributions from W bosons and fermions. Decays via fermion loops occur predominantly via top quark loops, with comparatively negligible contributions from light fermions due to the proportionality of the Higgs coupling to fermion mass. For an SM Higgs Boson with a mass $m_H = 125\,\mathrm{GeV}$, the total branching fraction of the $H \to \gamma\gamma$ decay channel is approximately 0.3%. Despite its small branching fraction, this channel was one of the most important for the initial observation of the Higgs boson, and continues to be very valuable for studies of particle properties due to its clean detector signature, which allows for events to be reconstructed with high efficiency. The decay width of a Standard Model Higgs boson with $m_H = 125\,\mathrm{GeV}$ is calculated from theory to be $4.07\,^{+3.97\%}_{-3.93\%}\,\mathrm{MeV}$. This intrinsic width of the decay is much narrower than the energy resolution achievable with the ATLAS detector. The observed width of the mass peak is therefore entirely dominated by detector effects.

The main sources of irreducible background events (i.e. background events with true $\gamma\gamma$ pair in the final state) are quark-antiquark annihilation ($q\bar{q} \to \gamma\gamma$), gluon fusion ($gg \to \gamma\gamma$), and parton fragmentation processes. These processes are illustrated in the form of Feynman diagrams in figure 6.1. In addition to these

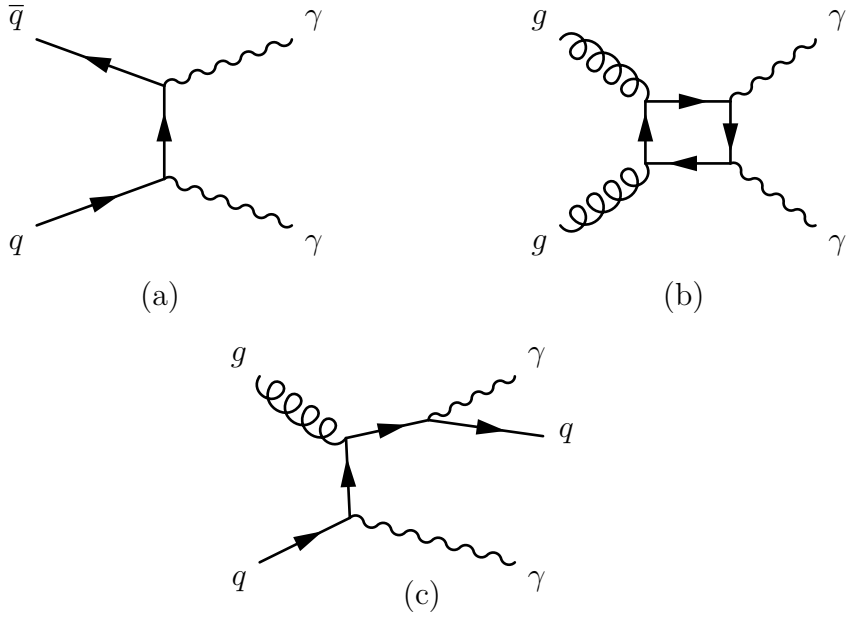

FIGURE 6.1: Feynman diagrams of the major sources of irreducible background to the $H \to \gamma\gamma$ process.

irreducible backgrounds, a number of reducible background processes also exist. These backgrounds consist predominantly of γ-jet and jet-jet events, in which jets are misidentified as photons. The total cross-section of such reducible backgrounds is significantly larger than that of irreducible backgrounds, but these processes are highly suppressed by the photon identification and isolation requirements.

6.3 $H \to \gamma\gamma$ p_{T} SPECTRUM

Some studies have already been performed to evaluate the compatibility of the particle discovered in 2012 with the Standard Model Higgs boson, as was discussed in section 6.1. Such studies may be performed, as in the case of the spin, parity, and coupling strength studies, by measuring directly intrinsic properties of the particle or its interactions. Another method is the measurement of inclusive or differential cross-sections. One advantage of cross-section measurements is that they are not strongly model-dependent. In the case of a differential cross-section analysis, conclusions are drawn not from the measurement of one given property, but from the distribution of some observable across many events. One observable

which of interest for such studies is the transverse momentum with which Higgs bosons are produced.

An inclusive measurement of the differential p_{T} cross-section in the $H \to \gamma\gamma$ decay channel may be compared to theoretical predictions for an SM Higgs boson (or indeed predictions based on other models). The term "inclusive measurement" here refers to the fact that the measurement does not attempt to preferentially select any subset of events, but to fully reconstruct all $H \to \gamma\gamma$ decays.

Comparison of the measured inclusive differential cross-section to SM predictions will provide a basis for a first level of comparison between observed data and theoretical predictions, but the measured differential cross-section can also be used for more in-depth study. The Higgs boson production modes described in section 2.2 each have different expected p_{T} spectra. In the case of gluon-gluon fusion, which is expected to be the dominant Higgs production mode in the ATLAS experiment, the transverse momentum of the Higgs boson tends to be low, as it is balanced only by the emission of soft gluons and quarks. In other production modes the system may be balanced by higher energy particles, and so Higgs bosons produced by these modes tend to have a higher p_{T}.

By taking advantage of these differences between the p_{T} spectra of production modes, the measurement of the Higgs p_{T} spectrum offers an opportunity to evaluate the relative production cross-sections of different production modes. The cross-section of any given production mode is sensitive to the coupling strength between the Higgs boson and other particles involved in the production mode, a measurement of the relative cross-sections of various production modes may therefore function as a test of Standard Model predictions. Due to limited statistics, it is impractical at this time to estimate the relative contributions of all production modes individually. Comparing the expected distributions of the various production modes (as illustrated in figure 6.2) reveals that the expected p_{T} distributions

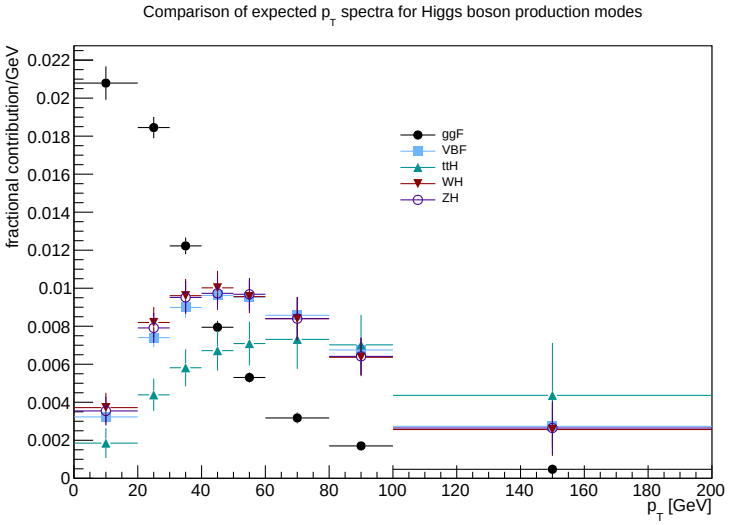

FIGURE 6.2: The expected p_{T} spectra of Higgs boson production modes are compared. All spectra are normalised to 1 allow for easier comparison of their shapes. The error bars reflect the statistical uncertainty resulting from the size of the MC samples.

of most production modes are relatively similar, but the expected p_{T} distribution resulting from the dominant gluon-gluon fusion production mode differs significantly from the others. As such, a study can be performed in which the relative production contribution of gluon-gluon fusion is evaluated with respect to the contribution all other production modes. The method by which this is performed will be described in section 6.11.

6.4 Data and Monte Carlo Samples

6.4.1 Dataset

This analysis uses approximately $20.3\,\mathrm{fb}^{-1}$ of data taken at $\sqrt{s} = 8\,\mathrm{TeV}$ during the year 2012. Events are selected only from data-taking periods in which the ATLAS detector was fully operational. The exact central value of the integrated luminosity for the dataset is $20\,276.9\,\mathrm{pb}^{-1}$, and the uncertainty on this value is 2.8%.

6.4.2 Monte Carlo Samples

Several MC samples are used, simulating Higgs boson production and decay for each production mode separately. For each production mode, samples are produced with Higgs boson mass m_H varying across the range 105–150 GeV in 5 GeV steps.

Higgs boson production through the gluon-gluon fusion production mode is simulated with the Powheg Box[85–87], with the Powheg generator[88] interfaced to Pythia8[89] for parton showering, hadronisation, and multiple parton interactions. The CT10[90] parton distribution function (*PDF*) set is used. These samples are normalised to calculations at next-to-next-to-leading-order (NNLO) in QCD[16–21], and next-to-leading-order (NLO) electroweak corrections[22, 91] are applied.

The same combination of Powheg and Pythia8 is used to produce samples for Higgs production via vector boson fusion, using the CT10 PDF set. These samples are normalised to cross-sections calculated with NLO electroweak corrections, and NLO QCD corrections with an additional approximate NNLO QCD correction[27].

Samples of simulated data with Higgs bosons produced in association with a W boson, Z boson, or $t\bar{t}$ pair are generated fully with Pythia8, using the CTEQ6L1[92] PDF set. For production in association with an electroweak boson, predictions are normalised to cross-sections calculated at NLO[29] and NNLO[28] with NLO radiative corrections[30]. The samples of Higgs boson production with a $t\bar{t}$ pair are normalised to calculations with full NLO QCD corrections[31–34]

Background samples of simulated prompt diphoton ($\gamma\gamma$), photon+jet (γj), and dijet (jj) events are also produced. The $\gamma\gamma$ and γj samples are simulated with final states including up to three additional partons, using the Sherpa[93] event generator with the CT10 PDF set. The jj samples are produced with Pythia8, using the CTEQ6L1 PDF set.

6.5 Theoretical Predictions

When measuring a differential cross-section, it is desirable to have a theoretical prediction to which a comparison may be made. For the gluon-gluon contribution, theoretical predictions are made with HRES[94, 95], with a $H \to \gamma\gamma$ branching ratio of $0.228 \pm 0.011\%$ applied. HRES provides NNLO+NNLL QCD accuracy, but has no electroweak corrections. The uncertainty resulting from the missing higher-order electroweak corrections is determined by producing cross-section predictions with the renormalisation, factorisation, and resummation scale factors simultaneously varied simultaneously by factors of 0.5 and 2, and taking the envelope of the predictions obtained from all combinations of scales except those where the renormalisation and factorisation scales differ by a factor of four. The calculation uses the CT10[90] PDF set. The uncertainty associated to the choice of parton distribution is estimated by a procedure which takes into account the central values and uncertainties of two other PDF sets, MSTW2008NLO[95] and NNPDF2.3[96]. For each PDF set, the uncertainties are calculated according to the procedure recommended by the collaboration. The overall uncertainty is then determined by taking the envelope of the individual uncertainties from each PDF set. Corrections are applied to account for photon isolation, using isolation and non-perturbative correction factors which are determined independently for each bin of the p_{T} differential cross-section. The total uncertainty is calculated by summing in quadrature the scale, PDF, branching ratio, photon isolation, and non-perturbative correction uncertainties.

Theoretical productions for the VBF, Higgsstrahlung, and $t\bar{t}H$ production modes are based on particle-level samples produced with the Powheg-Pythia and Powheg8 event generators. These samples are normalised to theoretical calculations as described in section 6.4.2, and the uncertainties associated with scale and PDF variations are taken from these calculations. For the VBF component, an additional

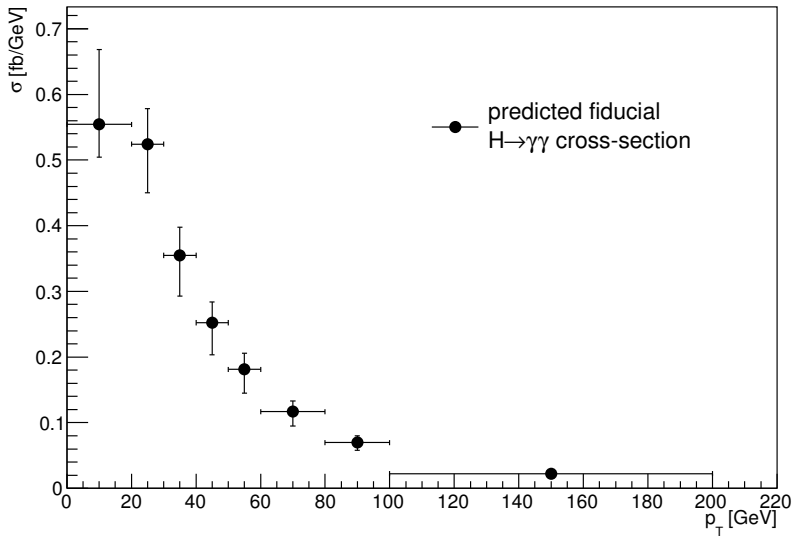

FIGURE 6.3: The fiducial $H \to \gamma\gamma$ differential cross-section in p_{T}, derived by the methods described in section 6.5. The vertical error bars indicate the total theoretical uncertainty (also as described in section 6.5). The predictions are normalised to the total cross-section recommendations of the LHC Higgs Cross Section Working Group[35].

shape-dependent scale uncertainty is derived from simultaneous variation of the event generator renormalisation and factorisation scales by factors of 0.5 and 2.

6.6 Event Selection and Reconstruction

Events are required to pass a diphoton trigger which requires that the event contain two electromagnetic clusters with p_{T} greater than 35 GeV and 25 GeV for the most and second-most energetic cluster respectively. The efficiency of this trigger for events which pass all other selection requirements is greater than 99%. In addition to the trigger requirement, selected events are required to have at least one reconstructed collision vertex, where a collision vertex is defined as a vertex to which at least three Inner Detector tracks with $p_{\mathrm{T}} > 400$ MeV are associated.

Photon candidates are reconstructed as described in section 4.2. For an event to pass the selection, it must contain at least two photons within the pseudorapidity range $|\eta| < 2.37$, excluding the crack region ($1.37 < |\eta| < 1.56$). The invariant

mass of the diphoton system is required to fall within the range $105\,\mathrm{GeV} < m_{\gamma\gamma} < 160\,\mathrm{GeV}$. Transverse momentum requirements are placed on the photons relative to this invariant mass: for the leading photon the ratio $p_{\mathrm{T}}/m_{\gamma\gamma}$ is required to be at least 0.35, and the subleading photon is required to have $p_{\mathrm{T}}/m_{\gamma\gamma} > 0.25$. Both photons are required to pass the tight photon identification criteria.

The impact of jets misidentified as photons is reduced further by requiring that all photons be isolated both in the Inner Detector and in the EM Calorimeter. The scalar sum of all Inner Detector tracks with $p_{\mathrm{T}} > 1\,\mathrm{GeV}$ which fall within a cone of radius $\Delta R = 0.2$ around the photon and originate from the primary vertex must be less than 2.6 GeV. In the case of a converted photon, the tracks matched to the photon itself are excluded from this summation. The EM Calorimeter isolation is calculated in a cone of $\Delta R = 0.4$, following the method described in section 4.2.5, with a threshold of 6 GeV. The combined photon isolation efficiency is around 95% per photon.

The invariant mass of the diphoton system is reconstructed according to equation (6.1).

$$m_{\gamma\gamma} = \sqrt{2p_{\mathrm{T},1}p_{\mathrm{T},2}\left(\cosh\Delta\eta - \cos\Delta\phi\right)}\,, \tag{6.1}$$

where $p_{\mathrm{T},1}$ and $p_{\mathrm{T},2}$ indicate the transverse momenta of the leading and subleading photon respectively, $\Delta\phi$ is the difference between the azimuthal angles of the two photons and $\Delta\eta$ represents the difference in pseudorapidity between the two photons. The resolution of the reconstructed mass is thus dependent upon the accuracy with which the primary vertex is reconstructed, along with the resolution of photon energy measurements. As such, the accurate reconstruction of the primary vertex position is especially crucial to studies in the $H \to \gamma\gamma$ channel. The primary vertex is selected by a neural network algorithm[97] which takes the following inputs:

- The z-position of the intersections of the photon trajectories extrapolated from the position of the shower in successive layers of the calorimeter with the beam axis.
- The sum of the squared transverse momenta (Σp_{T}^2) of tracks associated with the vertex.
- The scalar sum of the transverse momenta (Σp_{T}) of tracks associated with the vertex.
- The difference in azimuthal angle ($\Delta\phi$) between the direction of the diphoton system and that of the vector sum of all tracks associated to the vertex.
- The position of the conversion vertex, for any converted photons.

The direction (and therefore also the transverse momentum) of the photons is determined with respect to this reconstructed primary vertex. According to studies on simulated data[13], the efficiency of the primary vertex identification algorithm to reconstruct a point within $\Delta z = 0.3\,\mathrm{mm}$ of the true hard interaction vertex ranges from approximately 70% at high pile-up to near 100% at low pile-up, as illustrated in figure 6.4.

6.7 Signal and Background Modelling

To measure a differential p_{T} cross-section, rather than just an inclusive measurement of the total yield, the dataset is split into a number of p_{T} bins. The choice of p_{T} binning is described in section 6.7.1. The differential cross-section is extracted via a simultaneous signal and background fit to the $m_{\gamma\gamma}$ spectrum of each p_{T} bin, from which the signal yield in each bin is extracted. The signal shapes used for this fit are determined from studies of simulated data, this process is described in section 6.7.2. Studies on simulated data are also performed to determine the

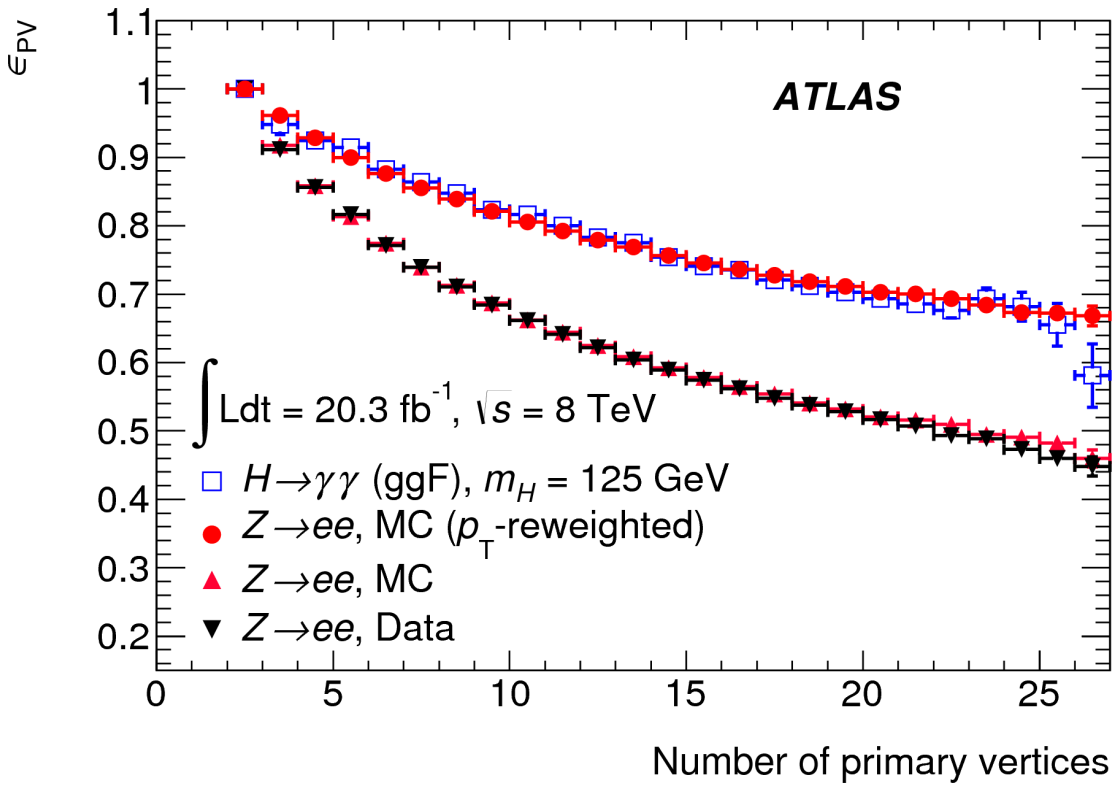

FIGURE 6.4: This figure[97] shows the efficiency, $\varepsilon_{\mathrm{PV}}$, of the neural network algorithm determining a primary vertex within 0.3 mm of the true primary vertex, as determined from studies performed on MC data. The unfilled blue squares show $\varepsilon_{\mathrm{PV}}$ for simulated gluon-gluon fusion events with a Higgs boson of mass $m_H = 125\,\mathrm{GeV}$ decaying to two unconverted photons. The performance of the algorithm on $Z \to e^+e^-$ events, with electron tracks removed, is shown for both data and MC as black and red triangles respectively. The red circles illustrate the performance on the same simulated $Z \to e^+e^-$ sample with reweighting applied to reproduce the harder p_{T} distribution of the simulated $H \to \gamma\gamma$ events.

appropriate parameterisation for the background shape within each p_{T} bin, this process is described in section 6.7.3. In the final fit, the value of m_H is fixed to 125.36 GeV, the value measured by the ATLAS Collaboration from $25\,\mathrm{fb}^{-1}$ of pp collision data using the $H \to \gamma\gamma$ and $H \to ZZ \to 4\ell$ decay channels[98].

6.7.1 Choice of p_{T} Binning

The p_{T} binning used in this measurement follows that used in previous ATLAS studies[2, 99]. The bins have non-uniform widths, and are optimised based on studies of simulated data. These studies evaluate the significance ($s/\sqrt{b}$) expected in each bin, assuming a Standard Model Higgs boson with mass $m_H = 125\,\mathrm{GeV}$,

p_{T} bin	Lower p_{T} bound (GeV)	Upper p_{T} bound (GeV)
1	0	20
2	20	30
3	30	40
4	40	50
5	50	60
6	60	80
7	80	100
8	100	200
9	200	

TABLE 6.1: The binning used in producing the Higgs boson production differential p_{T} cross-section. No upper limit is placed on the final bin, which accepts all events for which the reconstructed Higgs boson candidate diphoton system has a $p_{\mathrm{T}} > 200\,\mathrm{GeV}$.

with the significance evaluted within a diphoton invariant mass window of 121–129 GeV. The number of bins, and their respective bin boundaries, are chosen such that statistical fluctuations are unlikely to produce very small yields (which may cause difficulty in the fitting procedure) or negative yields (an unphysical result for a cross-section measurement). The bin boundaries are varied so that the expected significance is approximately the same in each bin. With 8 bins, a significance per bin of around 2σ is achieved within the invariant mass range 0–200 GeV. An additional overflow bin is added, with no upper limit, which accepts all events falling outside this range. The final binning is shown in table 6.1.

6.7.2 Signal Shape

The shape of the signal peak is modelled as the sum of a Crystal Ball function[100] and a Gaussian. The Crystal Ball and Gaussian components are combined by a weighted summation as shown in equation (6.4).

The Crystal Ball function is defined as

$$F_{\mathrm{CB}}(t_{\mathrm{CB}}, \alpha_{\mathrm{CB}}, \sigma_{\mathrm{CB}}, n_{\mathrm{CB}}, N_{\mathrm{CB}}) = N_{\mathrm{CB}} \begin{cases} e^{-t_{\mathrm{CB}}/2}, & \text{if } t_{\mathrm{CB}} > -\alpha_{\mathrm{CB}} \\ \frac{\left(\frac{n_{\mathrm{CB}}}{|\alpha_{\mathrm{CB}}|}\right)^{n_{\mathrm{CB}}} e^{-|\alpha_{\mathrm{CB}}|^2/2}}{\left(\frac{n_{\mathrm{CB}}}{|\alpha_{\mathrm{CB}}|} - |\alpha_{\mathrm{CB}}| - t_{\mathrm{CB}}\right)^{n_{\mathrm{CB}}}}, & \text{if } t_{\mathrm{CB}} \leq -\alpha_C B \end{cases} \tag{6.2}$$

where $t_{\mathrm{CB}} = \frac{m_{\gamma\gamma} - \mu_{\mathrm{CB}}}{\sigma_{\mathrm{CB}}}$ (with μ_{CB} denoting the position of the peak and σ_{CB} its width), α_{CB} denotes the position at which the Crystal Ball function switches between its Gaussian core and a power-law tail, and N_{CB} is a normalisation factor.

The Gaussian function is defined as

$$F_{\mathrm{G}}(t_{\mathrm{G}}, N_{\mathrm{G}}) = N_{\mathrm{G}} e^{-t_{\mathrm{G}}^2/2}, \tag{6.3}$$

where $t_{\mathrm{G}} = \frac{m_{\gamma\gamma} - \mu_{\mathrm{G}}}{\sigma_{\mathrm{G}}}$ (with μ_{G} denoting the position of the peak and σ_{G} its width) and N_{G} is a normalisation factor.

The combined fit function is defined as

$$F_{\mathrm{peak}}(F_{\mathrm{CB}}, F_{\mathrm{G}}, f_{\mathrm{CB}}) = f_{\mathrm{CB}} F_{\mathrm{CB}} + (1 - f_{\mathrm{CB}}) F_{\mathrm{G}}, \tag{6.4}$$

where f_{CB} characterises the relative contribution of the Crystal Ball and Gaussian function components.

The parameters of these functions are determined based on studies of simulated data. A number of simulated datasets are used, in which the value of m_H is varied in 5 GeV increments from 105 GeV to 150 GeV. The parameter values are determined, as a function of the mass of the Higgs boson, by a simultaneous fit to all mass points. The peak widths (σ_{CB} and σ_G) of the Crystal Ball and Gaussian components are related by a factor, a_k, which is held constant with respect to m_H. The parameters α_{CB} and f_{CB} are also constant with respect to m_H. All other

parameters are fitted with a linear dependence on m_H, and the fitting procedure therefore fits the signal shape as a function of m_H. The parameters used in the final fits are those corresponding to an m_H of $125.36 \pm 0.37(\text{stat.}) \pm 0.18(\text{syst.})\,\text{GeV}$, the value measured by the most recent ATLAS measurement of the Higgs boson mass from the $H \to ZZ \to 4\ell$ and $H \to \gamma\gamma$ channels[98]. This fitting process is performed independently for each p_{T} bin, and the results are shown in figure 6.5.

6.7.3 Background Treatment

The background distribution in most p_{T} bins are modelled with either an exponential of a second order polynomial (*exp2*) or an exponential of a third order polynomial (*exp3*). Table 6.2 shows the choice of background parameterisation for each of the p_{T} bins. The choice of functional form for background modelling in each bin follows that used in references [2, 101]. The choice of fit has an impact upon the expected systematic and statistical uncertainties on the final measurement, with more degrees of freedom offering the possibility of a better description of the true mass distribution, at the cost of increased statistical uncertainty.

A key factor in the decision is the level of *spurious signal*, the signal yield measured in a pure background sample, expected for each possible choice of background form. The evaluation of the spurious signal is shared with the analysis in [2]. The evaluation is based on fits to high-statistics simulated $\gamma\gamma$,γ-jet, and jet-jet events. Data-driven studies are performed to estimate the relative contributions of each component to the background composition. In these background composition studies, events are selected which contain pairs of photon candidates, passing a loosened identification requirement in which the requirements on the shower shapes w_{s3}, F_{side}, ΔE, and E_{ratio} are relaxed with respect to the standard tight identification requirements. The signal region is defined by requiring tight identification and the 6 GeV isolation requirement which is also applied in

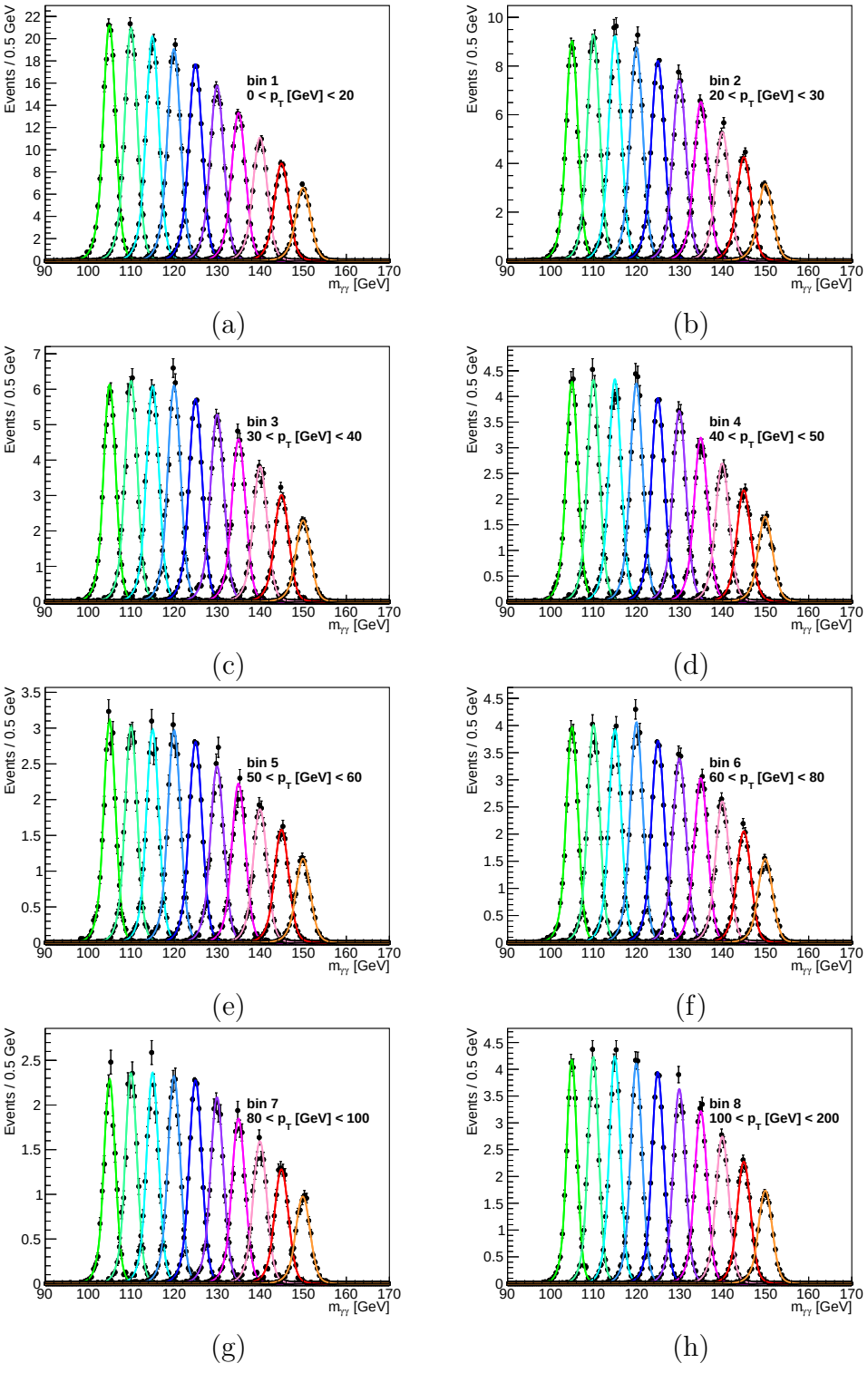

FIGURE 6.5: Subfigures 6.5(a) to 6.5(h) show the signal shapes fitted in the simulated data samples for each Higgs boson mass point in each of the p_{T} bins 1–8. The black points show the reconstructed $m_{\gamma\gamma}$ distributions of the MC samples, with error bars indicating the statistical uncertainties, and the fitted signal shapes are shown as coloured lines.

the analysis selection. The background control regions are defined by requiring photon candidates to pass the loosened identification requirement and fail one or both of the tight identification requirement and the isolation requirement. The leading and sub-leading photon candidates in each event are simultaneously and independently classified into their appropriate categories. In total, this provides $4 \times 4 = 16$ possible photon candidate categorisation combinations by which events may be categorised, which correspond to a set of 16 simultaneous equations.

These equations require the efficiencies of both tight photon identification and the photon isolation requirement, when applied to photon candidates from the sample, and with corrections for signal leakage. Some of these efficiencies cannot be directly measured from data, and so are estimated from $\gamma\gamma$ MC samples with full corrections applied for photon identification efficiency scale factors, energy correction, pileup reweighting, and z-vertex corrections. The set of equations can then be solved for the yields and fake rates of the $\gamma\gamma$, γ-jet, jet-γ, and jet-jet background components.

The full simulated dataset is normalised such that it corresponds to the real 2012 dataset. The signal model used in the spurious signal studies is the same as that used in the data analysis. For any parameterisation under consideration to be accepted for a given bin, the spurious signal measured is required to be either less than 10% of the expected Higgs signal yield (assuming a Standard Model Higgs boson) or less than 20% of the expected background uncertainty. If more than one parameterisation fulfills the requirements, the parameterisation with fewer degrees of freedom is preferred.

p_{T} bin	Background form
1	exp2
2	exp3
3	exp2
4	exp3
5	exp2
6	exp2
7	exp2
8	exp2

TABLE 6.2: The functional form chosen to describe the background $m_{\gamma\gamma}$ distribution in each p_{T} bin.

6.8 Systematic Uncertainties

6.8.1 Luminosity

The analysis uses the full 2012 ATLAS proton-proton collision dataset. The total integrated luminosity of this dataset is measured as $20.3\,\mathrm{fb}^{-1}$, with an uncertainty of $\pm 2.8\%$.

6.8.2 Signal Shape Uncertainties

The predicted mean value and the width of the signal peak are affected by systematic uncertainties relating to the photon energy scale and resolution (shared between all p_{T} bins). The photon energy scale and resolution are measured using $Z \to e^+e^-$ events[70], using the procedure described in section 4.2.6. Many systematic uncertainties are evaluated, corresponding to physics effects (such as mismodelling of the photon conversion rate) and uncertainties relating to detector property measurements and detector calibration (such as cell energy response, and the energy leakage between neighbouring calorimeter cells), as well as uncertainties associated to the method used for the measurement itself. These uncertainties are shared with the analysis in reference [2].

A total of 29 uncorrelated systematic uncertainties on the photon energy scale are considered, and four uncertainties on the photon energy resolution. To simplify the treatment of these uncertainties, some components of the photon energy scale and energy resolution uncertainties are merged by addition in quadrature.

6.8.2.1 Photon Energy Scale

The impacts of the photon energy scale uncertainties are evaluated by measurement of the *mass bias* on simulated $H \to \gamma\gamma$ events[102]. For each energy scale uncertainty, a signal-only MC sample is produced to which the energy scale variation is applied. The standard analysis selection process is then applied, and a fit performed using the standard signal model to measure the estimated Higgs boson mass $m_H^{'}$ with that variation applied. The obtained $m_H^{'}$ is compared to the Higgs boson mass m_H estimated by applying the same selection and fitting process to a nominal MC sample with no energy scale variation applied. The mass bias is then calculated as:

$$\text{mass bias} = \frac{m_H^{'} - m_H}{m_H} \,. \tag{6.5}$$

This process is repeated individually for each of the 29 photon energy scale uncertainties. The four uncertainties with the most significant impacts are:

L2 LAr gain relating to differences observed between electrons reconstructed from clusters with and without at least one cell the second layer of the ATLAS liquid argon calorimeter measured in medium gain,

LeakageConv relating to lateral leakage (in η and ϕ) of deposited energy into regions outside the cluster used for reconstruction,

Photon energy scale	p_{T} bin								
	1	2	3	4	5	6	7	8	9
L2 LAr gain (%)	0.10	0.11	0.11	0.12	0.13	0.14	0.16	0.20	0.28
Leakage conv (%)	0.07	0.07	0.07	0.07	0.07	0.07	0.07	0.07	0.07
LAr calib barrel (%)	0.07	0.07	0.07	0.08	0.08	0.08	0.08	0.09	0.13
LAr elec unconv barrel (%)	0.08	0.08	0.08	0.08	0.08	0.08	0.08	0.08	0.09
Rest (%)	0.11	0.12	0.12	0.12	0.11	0.12	0.12	0.12	0.12

TABLE 6.3: The uncertainty per p_{T} bin (in %) corresponding to each of the four main contributions to the photon energy scale systematic uncertainty. The line labelled "Rest" gives the value of the combination (by addition in quadrature) of the remaining contributions.

LAr calib barrel measurement of the intercalibration between the first and second layer of the liquid argon calorimeter is dependent upon muons, this uncertainty relates to the impact on the overall calibration of the liquid argon calorimeter resulting from response differences between muons and electrons or photons in the barrel region of the liquid argon calorimeter, and

LAr elec unconv barrel relating to differences in calibration of the liquid argon calorimeter between electrons and unconverted photons, within the barrel region.

These four uncertainties are retained as separate sources of uncertainty. The remaining 25 sources of uncertainty on the photon energy scale are combined by addition in quadrature, and this combination is treated as one systematic uncertainty. The uncertainty per p_{T} bin of the four main contributions and the combined value of the remaining contributions are shown in table 6.3.

6.8.2.2 Diphoton Invariant Mass Resolution

The systematic uncertainties on the resolution of the diphoton invariant mass are propagated from the energy resolution measured for single photons[102]. There are four contributions to this uncertainty:

- Constant term: the uncertainty on the extraction of the smearing applied on the MC sample. The constant term is measured in a study of $Z \to e^+e^-$ data, and the uncertainty on that measurement varies from approximately 0.002 (on a constant term of approximately 0.007) in the central barrel region to around 0.006 (on a constant term of around 0.025) in the endcap region, and is used directly (*ZSmear*).

- Intrinsic resolution: the intrinsic resolution of the calorimeter. This effect is evaluated based on studies of calorimeter module behaviour in simulation and in test-beam studies. The sampling term on the energy resolution extracted from simulated data agrees with the test-beam analysis to within 10%, and this value is assigned as the uncertainty (*Sampling term*).

- Material mismodelling effects: the energy resolution is affected by changes in the material present upstream of the calorimeter. This effect can introduce a bias into the effective constant term which is measured in the calibration procedure and applied in MC samples. Estimation of the size of this systematic uses MC samples produced with a simulated detector geometry which includes additional material before the calorimeter. The resolution extracted from MC samples with the nominal material distribution is convoluted with the resolution extracted from these samples with additional material placed before the calorimeter. A comparison is then made between the resolution observed in the MC samples with additional material and the result of the convolution of this result with that in the nominal MC sample. The difference of these two resolutions is then taken as the uncertainty on the final energy resolution (*Material*).

- Electronics and pileup noise: contributions from electronic noise scale like $1/E$ or $1/E_{\mathrm{T}}$, and so matter primarily at low energy. The digitiser in the MC simulation is known to model the true electronic noise of the EM calorimeter

Diphoton invariant mass	p_{T} bin								
	1	2	3	4	5	6	7	8	9
ZSmear (%)	8.38	8.70	8.65	8.84	8.84	9.44	9.60	9.04	13.10
Sampling Term (%)	2.36	2.17	2.70	2.21	2.76	3.06	3.39	2.41	8.28
Material (%)	3.93	4.35	3.78	4.42	4.14	4.44	4.52	3.61	6.21
PileUp (%)	1.31	0.81	1.35	0.83	1.11	1.11	1.51	1.20	1.38
Combination (%)	9.64	9.99	9.91	10.15	10.21	10.93	11.23	10.10	16.75

TABLE 6.4: The systematic uncertainty per p_{T} bin (in %) corresponding to the resolution of the diphoton invariant mass.

to significantly better than 10%. The electric noise level within the presampler layer is known less accurately due to changes to the voltage during the 2012 data-taking period which are not reflected in the MC digitisation parameters, but these changes account for only a few percent of the total electronics noise in a full cluster. Pileup noise is accounted for by the inclusion in MC samples of inelastic pp events. Estimation of pileup noise is sensitive to uncertainties in the modelling of these events, and to the modelling of the EM calorimeter pulse shape and signal digitisation (*PileUp*).

These four sources of resolution uncertainty are merged by addition in quadrature, and treated as one single systematic uncertainty on the energy resolution. The value per p_{T} bin is shown in table 6.4.

6.8.3 Background Uncertainties

A major consideration when evaluating systematic uncertainties related to the background $m_{\gamma\gamma}$ distribution is the spurious signal effect described in section 6.7.3. The choice of functional form used within each p_{T} bin is intended to ensure the spurious signal bias is not large, but the effect cannot be entirely prevented. The extent of the spurious signal effect observed in a given sample of simulated data is susceptible to statistical fluctuations within that sample. As the ratio between background and spurious signal can be expected to behave smoothly across p_{T}

bins, the value of this uncertainty is assigned based on a sliding window average of the measured spurious signal in a window including the p_{T} bin under study and its immediately neighbouring p_{T} bins. This is applied on three Higgs boson mass points, 120 GeV, 126.5 GeV, and 130 GeV. The value for bin i is determined as

$$\langle b \rangle_i = \frac{B_i}{3} \Sigma_{j=i-1}^{i+1} \frac{b_j}{B_j} \,, \tag{6.6}$$

where b_j is the spurious signal in bin j and B_j is the number of background events within the signal region in bin j, as estimated from the background component of the full signal plus background fit to data. The formula aims to keep b_j/B_j constant, as the spurious signal is expected to scale with the number of background events. In the first and last bins, which each have only one neighbour, the average is calculated from two bins rather than three. Finally, the largest of the spurious signal estimates from the three mass points is assigned as the corresponding uncertainty in each bin.

6.9 Signal Extraction

The signal yield within each p_{T} bin is extracted by performing a simultaneous maximum likelihood fit to all bins. The fit maximises an expression of the form

$$\begin{aligned} \mathcal{L}\left(v, n^{\mathrm{sig}}, n^{\mathrm{bkg}}, \theta^{\mathrm{sig}}, \theta^{\mathrm{bkg}}, m_H\right) = & \prod_i \left\{ \frac{e^{-v_i}}{n_i!} \prod_j^{n_i} \left[n_i^{\mathrm{sig}} \mathcal{S}_i\left(x_j; \theta^{\mathrm{sig}}, m_H\right) + n_i^{\mathrm{bkg}} \mathcal{B}_i\left(x_j; \theta^{\mathrm{bkg}}\right) \right] \right\} \\ & \times \prod_k G\left(\alpha_k^{\mathrm{sig}}, \theta_k^{\mathrm{sig}}, \delta_k^{\mathrm{sig}}\right) \,, \end{aligned} \tag{6.7}$$

where $n_i = n_i^{\mathrm{sig}} + n_i^{\mathrm{bkg}}$, which indicate respectively the number of signal and background events in bin i, v_i denotes the mean value of the underlying Poisson distribution of those n_i events, which is treated in the fit as an independent parameter. The signal PDF, $\mathcal{S}_i\left(x_j; \theta^{\mathrm{sig}}, m_H\right)$, depends upon the Higgs mass, m_H, and a vector of nuisance parameters, θ^{sig}, which account for the systematic uncertainties on the signal shape (as described in section 6.8.2). The background PDF, $\mathcal{B}_i\left(x_j; \theta^{\mathrm{bkg}}\right)$ similarly depends upon a vector of nuisance parameters, denoted θ^{bkg}, accounting for the systematic uncertainties affecting the background distribution (these uncertainties are described in section 6.8.3). The index k in the final term denotes the detector-related uncertainties on the signal shape. Gaussian constraints are introduced to control these nuisance parameters, where the width of the Gaussian is 1 and the mean 0. In the Gaussian function, α^{sig} indicates the values of auxiliary measurements and δ^{sig} the systematic uncertainty.

The fitting procedure does not allow for trivial extraction of the systematic uncertainty on the signal yield resulting from the fitting procedure itself. To evaluate the impact of the fitting procedure on the signal yield, an *Asimov dataset*[103], in which the distribution of any variable corresponds to exactly the expected distribution for that variable, is constructed from the fitted signal plus background function. Two fits of the signal plus background probability function are then performed. In one of these fits, the nuisance parameters are forced to remain equal to the values determined by the initial fit to data; in the other, the nuisance parameters are allowed to vary as part of the fitting process. The uncertainty on the signal yield obtained with fixed nuisance parameters is then subtracted in quadrature from the uncertainty on the signal yield obtained when the nuisance parameters are allowed to vary, and this is taken as a measurement of the systematic uncertainty on the signal yield resulting from the fitting procedure. The uncertainty on the signal yield resulting from background modelling is estimated

p_{T} bin	1	2	3	4	5	6	7	8
Systematic uncertainty (%)	9.5	5.5	5.6	5.6	6.1	6.3	6.2	6.3

TABLE 6.5: The value per bin of the systematic uncertainty on the signal yield which is assigned to account for the background modelling and signal fitting procedure.

from fits of the chosen background function to simulated data samples containing only background ($\gamma\gamma$, γj, jj) events. Table 6.5 gives the total value of these uncertainties per bin, combined by addition in quadrature.

6.10 Fiducial Differential Cross-section

The fiducial differential cross-section is defined as:

$$\sigma_i^{\mathrm{fid}} = \frac{N_i^{sig}}{C_i \mathcal{L}_{\mathrm{int}}}\,, \tag{6.8}$$

where N^{sig_i} denotes the number of signal events measured in bin i, $\mathcal{L}_{\mathrm{int}}$ denotes the total integrated luminosity of the analysed dataset, and C_i is a bin-specific correction factor accounting for experimental effects.

The fiducial volume is defined to be the region $|\eta| < 2.37$, with energy requirements on the leading and sub-leading photons of $p_{\mathrm{T}}/m_{\gamma\gamma} > 0.35$ and $p_{\mathrm{T}}/m_{\gamma\gamma} > 0.25$ respectively, and an isolation requirement applied to both photons. The isolation requirement applied to data and to detector-level MC samples is based on energy deposits in the calorimeter within a cone $\Delta R < 0.4$ of the photon, which must not be greater than 6 GeV. In particle-level MC samples the sum of p_{T} of all stable particles within a cone $\Delta R < 0.4$ of the photon is required to be less than 14 GeV. This was found to be approximately equivalent to the 6 GeV calorimetric isolation requirement applied at reconstruction level. The isolation requirement reduces the number of non-signal photons passing the selection requirements. It also reduces

the model dependence of the unfolding procedure, and thus reduces the associated uncertainties.

The values of the correction factors are determined from MC samples, as:

$$C_i = \frac{n_i^{\mathrm{det}}}{n_i^{\mathrm{part}}}\,, \tag{6.9}$$

where n_i^{part} is the number of events measured in bin i in the MC sample at particle level, and n_i^{det} the number of events measured in bin i in the MC sample at detector level. Detector-level and particle-level distributions are produced by combining the predicted yield of each production channel. These correction factors account for the effects of reconstruction and identification efficiencies, migration between bins, and migration into or out of the fiducial region due to the effects of detector resolution or miscalibration. To illustrate how these effects impact on the measured distribution, it is useful to consider the efficiency and purity of each bin. The efficiency of bin i is defined as:

$$\varepsilon_i = \frac{n_i^{\mathrm{det,part}}}{n_i^{\mathrm{part}}}\,, \tag{6.10}$$

where n_i^{part} is the number of events in bin i at particle level, and $n_i^{\mathrm{det,part}}$ is the number of events which are both present in bin i at particle level and selected in bin i at detector level. The efficiency is therefore a measure of the likelihood of an even which exists in bin i at particle level being selected in that same bin at detector level. It is reduced both when events are lost during reconstruction or identification and when events migrate into other bins due to detector resolution effects.

The bin purity is defined as:

$$P_i = \frac{n_i^{\mathrm{det,part}}}{n_i^{\mathrm{det}}}\,, \tag{6.11}$$

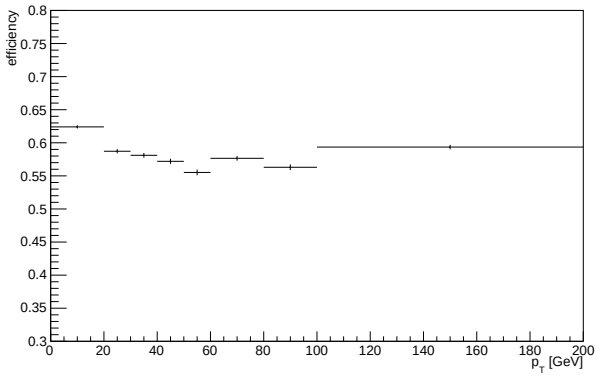

FIGURE 6.6: The efficiency of each p_{T} bin. The error bars indicate the statistical uncertainty resulting from the size of the MC sample.

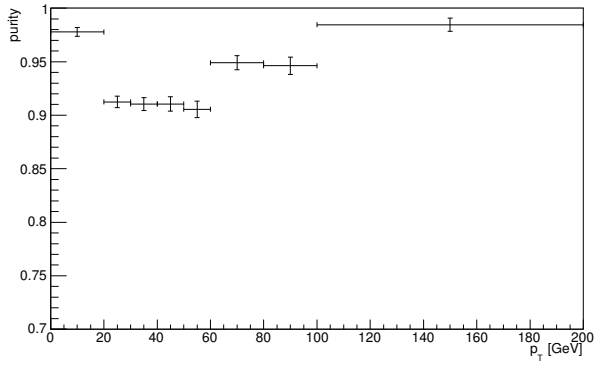

FIGURE 6.7: The purity of each p_{T} bin. The error bars indicate the statistical uncertainty resulting from the size of the MC sample.

where $n_i^{\mathrm{det,part}}$ again denotes the number of events which are present in bin i at both particle level and detector level, and n_i^{det} is the total number of events selected in bin i at particle level. It functions as measure of the likelihood that an event reconstructed and selected in bin i is a true event in bin i at particle level. The purity is reduced both when events belonging to other bins at particle level migrate into bin i at detector level due to resolution effects, and when a reconstructed event is a fake event with no particle-level counterpart.

The efficiency and purity of each bin are shown in figure 6.6 and figure 6.7, and the level of migration between bins is illustrated in figure 6.8.

Due to the high statistics of the MC samples, the statistical uncertainty on the

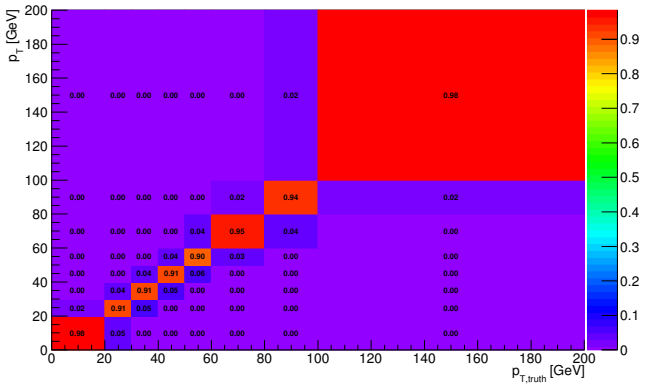

FIGURE 6.8: The migration matrix for the chosen p_{T} bins, normalised by row.

correction factors defined above is very small (below 0.1% in all bins). The nominal correction factors are determined using the MC samples described in section 6.4.2, which were produced with Pythia8 (ttH, WH, ZH production modes) and POWHEG+Pythia8 (gluon-gluon fusion and vector boson fusion production modes). The correction factors measured from these samples are not independent of the choice of event generator, and so an uncertainty is assigned based on the differences in the correction factors observed in MC samples produced with different generators. This uncertainty is shared with the analysis in [2]. Alternate MC samples were produced using Sherpa [93], MiNLO HJ+Pythia8 [89, 104] and MiNLO HJJ+Pythia8 [89, 104] for the gluon-gluon fusion production mode, and by POWHEG+JIMMY[88, 105] for both the gluon-gluon fusion and the vector boson fusion production modes. The impact of differences in the underlying event is also estimated, by disabling multiple-parton interactions in Pythia8. The fractional difference between each considered variation and the nominal correction factors is shown in figure 6.9. The value of the uncertainty is assigned based on the envelope of the correction factors produced from these variations.

The correction factors are also sensitive to the trigger efficiency and photon identification efficiency, and the efficiency of the photon isolation requirements. These uncertainties are shared with [2]. The efficiency of the diphoton trigger is measured using a bootstrap method, with systematic uncertainties evaluated by comparing

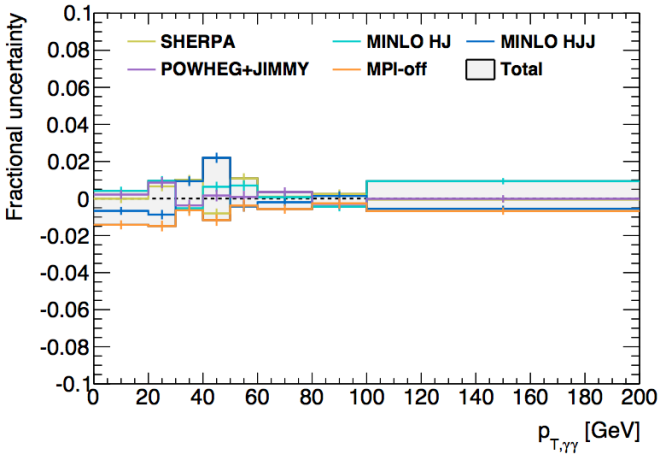

FIGURE 6.9: The fractional difference between the nominal correction factors and those obtained with alternate MC samples[2]. The envelope of these variations is assigned as a systematic uncertainty on the correction factors.

measurements in real data with those on a pure signal MC sample. A further data-driven study using photons from radiative decay of Z bosons is used as a cross-check. The trigger efficiency is found to be $99.61^{+0.06}_{-0.07}(\text{stat.}) \pm 0.5\%(\text{syst.})$[106]. As such, an uncertainty of 0.5% is applied.

A measurement of photon identification efficiency is made from the combination of three methods, as detailed in section 5.8. The uncertainties on the combined measurement are propagated through MC samples to determine the effect on the $H \to \gamma\gamma$ selection, and an event-level uncertainty of 1% is assigned.

The uncertainty on the efficiency of the photon isolation requirement is estimated from $Z \to e^+e^-$ events. The same isolation requirement as used in the $H \to \gamma\gamma$ selection is applied to the electrons, and the selection efficiency in data is compared to that observed on MC samples. The efficiency of the isolation selection is dependent upon jet multiplicity in the event. An uncertainty of $\pm 1\%$ is assigned for the isolation selection efficiency of the di-photon system in events with fewer than 2 jets, $\pm 2\%$ for events with exactly 2 jets, and $\pm 4\%$ for events with 3 or more jets.

While the analysis is targeted at the $H \to \gamma\gamma$ decay channel, some events from the

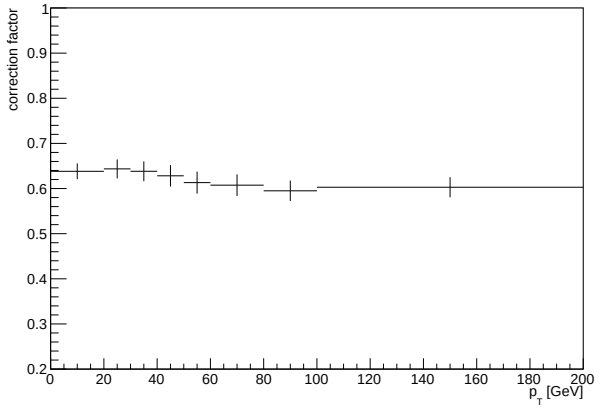

FIGURE 6.10: The correction factors of each p_{T} bin, with error bars indicating the combined statistical and systematic uncertainty.

Dalitz decay channel, $H \to \gamma f\overline{f}$ can pass the full event selection. This typically happens as a result of the $f\overline{f}$ pair being reconstructed as a photon (mostly when the final state is $\gamma e\overline{e}$, or when the fermion pair produced a high-p_{T} π^0). In this case, the invariant mass reconstructed from the system consisting of the real and fake photon is close to that of the Higgs boson, and the event will closely resemble a true $H \to \gamma\gamma$ event. These events are included in MC samples at reconstruction level, and the effect of their inclusion evaluated. Recent calculations estimate the total Dalitz cross-section as approximately 7% of the $H \to \gamma\gamma$ cross-section[107]. However, the Dalitz decay branching ratio is not well-known, and following the treatment in reference [2] a 100% uncertainty is applied on the contribution from this source.

These sources of systematic uncertainty are added in quadrature to produce the combined systematic uncertainty on the correction factors. Figure 6.10 shows the correction factors, along with the combined statistical and systematic uncertainty. The correction factors have little p_{T} dependence, and a typical combined uncertainty of around 0.02.

6.11 Higgs Boson Production Modes

As was mentioned in section 6.3, the measurement of the Higgs boson production differential cross-section in p_{T} not only provides an opportunity for direct comparison of the inclusive Higgs boson production p_{T} spectrum to theoretical predictions from the Standard Model or indeed other models, but also enables for a study of the relative contributions of different production modes. Due to statistical limitations, it is not practical to consider all production modes individually. However, as discussed in section 6.3, the distinctiveness of the Higgs production via gluon-gluon fusion (*ggF*) produces a p_{T} spectrum which differs significantly from those of all other production modes (*non-ggF* production), allowing for an assessment of the relative contributions of ggF and non-ggF Higgs production.

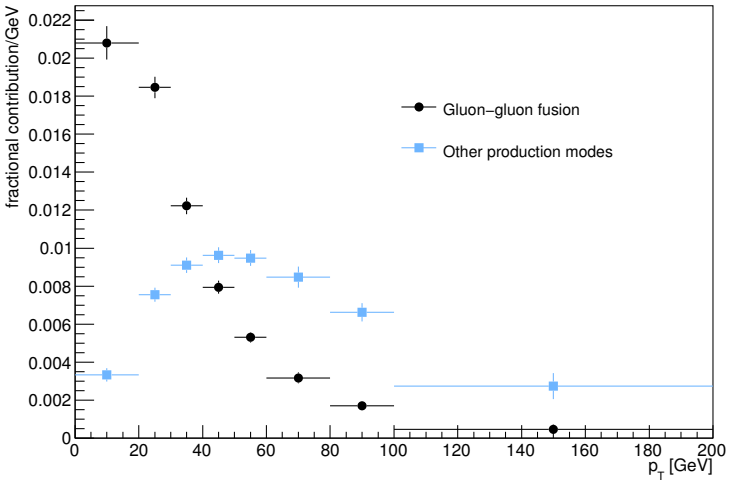

FIGURE 6.11: The expected p_{T} spectra of Higgs boson production via gluon-gluon fusion to the combination of all other production modes, combined according to Standard Model predictions. Both spectra are normalised to a total area of 1, to allow for easier comparison of their shapes.

The overall p_{T} spectrum is first derived, as described in sections 6.7.2 and 6.7.3. Templates for the expected p_{T} distributions of ggF and non-ggF Higgs production are determined using simulated data. The ggF template is produced by extracting the reconstructed p_{T} distribution of all true ggF events which pass the full analysis

selection. To extract the non-ggF template, this process is performed for each production mode other than gluon-gluon fusion, and the production modes are then weighted according to the Standard Model prediction of their cross-sections. The MC sample used in this process is produced with a Higgs boson mass m_H of 125 GeV, and the cross-sections used to determine the weights used for the production of the combined non-ggF template also correspond to a Standard Model Higgs boson of this mass.

Once the templates for ggF and non-ggF production are determined, the relative contribution of each to the measured p_{T} differential cross-sections is estimated by performing a template fit to the distribution observed in data. The contributions of the ggF and non-ggF templates are varied, and a χ^2 test is used to determine the ratio which best reproduces the data.

6.11.1 Projection to Larger Datasets

Due to the large statistical uncertainties on the measurement of a p_{T} spectrum measurement with the 2012 dataset, the results of the study described in section 6.11 necessarily also have large uncertainties. These large uncertainties place some constraints upon the conclusions able to be drawn at this time. As more data is taken and analysed, the precision with which the Higgs boson p_{T} spectrum can be measured will improve. An improvement to the precision with which the relative contributions of different production modes can be measured will also result. Here, an attempt is made to estimate how the uncertainties on this study may evolve as more data is taken.

In estimating future evolution of uncertainties, some assumptions must be made as to how different types of uncertainty depend upon both the size of the data sample and other factors such as the increased instantaneous luminosity and centre of mass energy of future ATLAS datasets.

Most of the systematic uncertainties considered in this analysis are determined as a fractional uncertainty on the observed signal yield and do not have a strong statistical dependence. Uncertainties resulting from the performance of the ATLAS detector and from the performance of trigger, reconstruction, or identication algorithms may be sensitive both to the size of the dataset and the different conditions in which new data will be taken. It is difficult to evaluate at this time how such uncertainties will be affected, and here they are tentatively assumed to retain their current fractional values. Statistical uncertainties are assumed to scale proportionally to $\sqrt{N}$ (for a dataset of size N). To avoid confounding the effects of improved statistics with the effects of the energy dependence of both signal and background cross-sections, the study retains the centre-of-mass energy of the 2012 dataset, $\sqrt{s} = 8\,\mathrm{TeV}$, and event selection efficiency and energy resolution are assumed to remain the same.

6.11.2 Projected Measurements

The possible evolution of uncertainties for studies of this kind is evaluated at three total luminosity working points:

- $203\,\mathrm{fb}^{-1}$,
- $300\,\mathrm{fb}^{-1}$,
- $2030\,\mathrm{fb}^{-1}$.

The first and third working points are chosen as they correspond to the integrated luminosity of the 2012 dataset multiplied by factors of 10 and 100, respectively, while the second working point corresponds to the combined total integrated luminosity projected for *Run 2* and *Run 3* at the time of performing this study.

For each of these luminosity working points, pseudodata $m_{\gamma\gamma}$ distributions are generated using a template-based method. The background component of the pseudodata is derived from a data-driven template, where the template is based upon the background component of the simultaneous signal plus background shape fit which is performed in the analysis of the 2012 ATLAS dataset. As this study is to be performed under the assumption of a Standard Model Higgs boson, the template for the signal component is based on the $m_{\gamma\gamma}$ distribution resulting from simulated $H \to \gamma\gamma$ events. These templates are derived from the same MC samples previously described in section 6.4.2.

The signal and background templates are added together to produce a combined signal and background template, which is then scaled appropriately to produce the expected yield per p_{T} bin at each luminosity working point. The sizes of the uncertainties on the scaled templates are determined according to the assumptions described in section 6.11.1. The expected yield produced in this process gives only a central value, with no statistical effects. To produce more realistic $m_{\gamma\gamma}$ distributions, the yield in each p_{T} bin is finally varied by the addition of a random value thrown from a Gaussian distribution centred on zero, with a width equal to the total uncertainty on the yield in that bin. This effectively simulates the fluctuations which are expected to arise in a real dataset. As a result, any observable studied or measurement made on such a dataset is subject to variation from the expected value. For this reason, 1000 projected datasets are produced for each luminosity working point, so that it is possible to observe the distribution of any interesting property at each of the chosen working points.

6.12 Results

6.12.1 Measurement of the $H \to \gamma\gamma$ Differential Cross-Section in p_{T} in the 2012 ATLAS Dataset

The results of performing the fitting procedure described in section 6.9 are illustrated for each p_{T} bin in subfigures 6.12(a) to 6.12(h). The signal yields fitted in each bin are collated to measure a p_{T} spectrum. The correction factors described in section 6.10 are applied and the result is then divided by the total integrated luminosity of the dataset to produce a fiducial differential cross-section. The measured cross-section is illustrated and compared to theoretical predictions in figure 6.13. The measured differential cross-section is somewhat higher than the theoretical predictions in several bins, but given the large uncertainties on the measurement the difference is not significant, and the measurement is broadly compatible with expectations. A summary of the measured cross-section is presented in table 6.6.

Bin	0	1	2	3	4	5	6	7
p_{T} (GeV)	0–20	20–30	30–40	40–50	50–60	60–80	80–100	100–200
Yield	34.53	184.06	88.41	99.60	53.46	62.88	48.19	23.52
$d\sigma_{fid}/dp_T$	0.09	0.91	0.44	0.49	0.26	0.16	0.12	0.01
Total uncertainty (%)	372.7	30.4	50.2	38.3	60.6	53.8	50.1	90.2
Fit systematic uncertainty (%)	9.6	10.0	9.9	10.2	10.2	10.9	11.2	10.1
Fit statistical uncertainty (%)	363.0	25.6	46.9	34.4	57.9	50.6	46.9	88.7
Spurious signal (%)	82.7	5.4	9.4	5.3	8.1	6.8	3.3	7.3
Luminosity (%)	2.8	2.8	2.8	2.8	2.8	2.8	2.8	2.8
Photon ID (%)	1.0	1.0	1.0	1.0	1.0	1.0	1.0	1.0

Table 6.6: Summary of differential cross-section measurement.

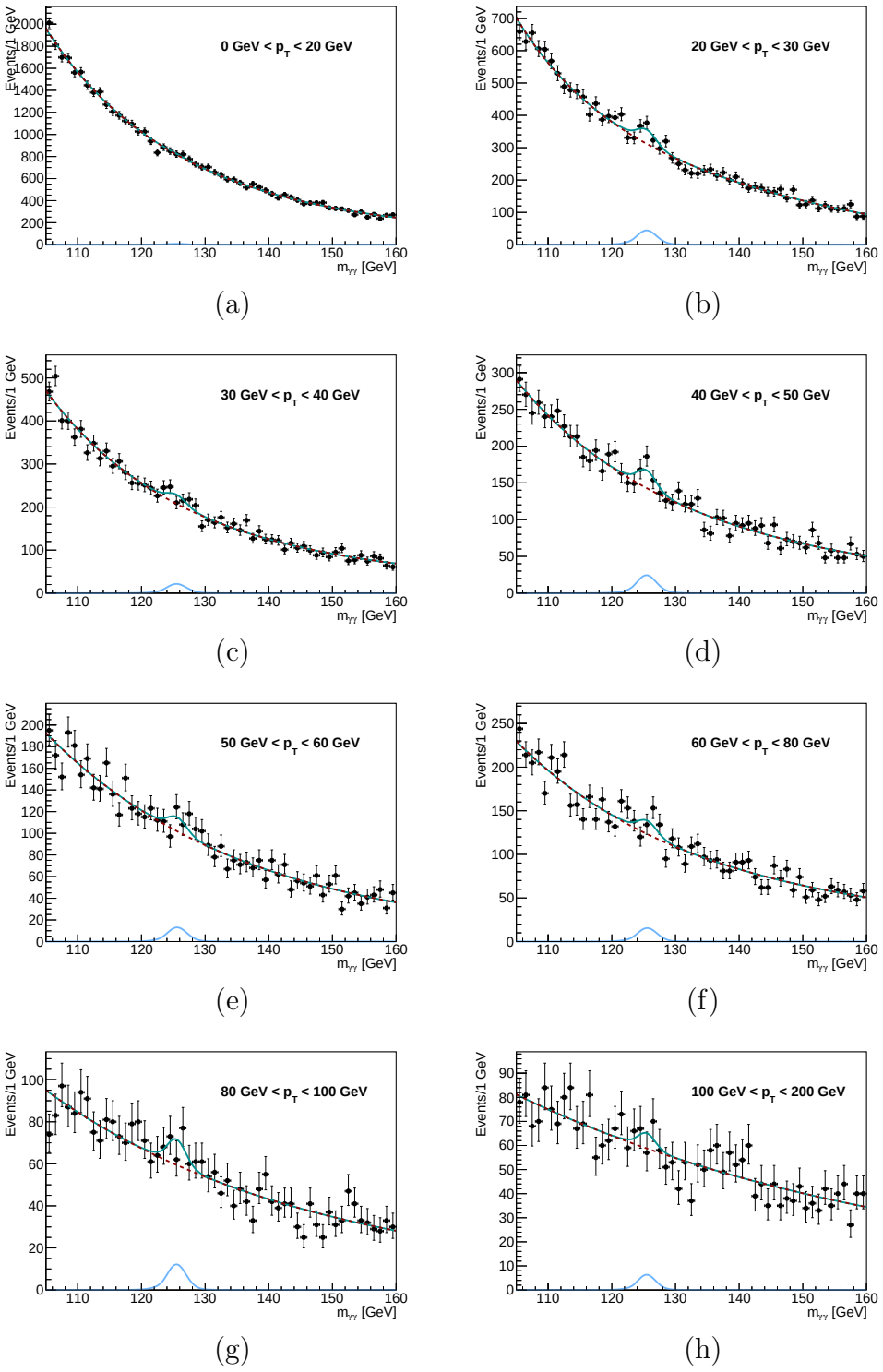

FIGURE 6.12: Subfigures 6.12(a) to 6.12(h) show the results for each p_{T} bin. In each bin, the reconstructed $m_{\gamma\gamma}$ distribution of recorded events is shown by the black points, and the combined signal plus background fit to this distribution is illustrated as a solid green line. The signal and background components of the fit are shown as a solid blue line and a dashed red line respectively.

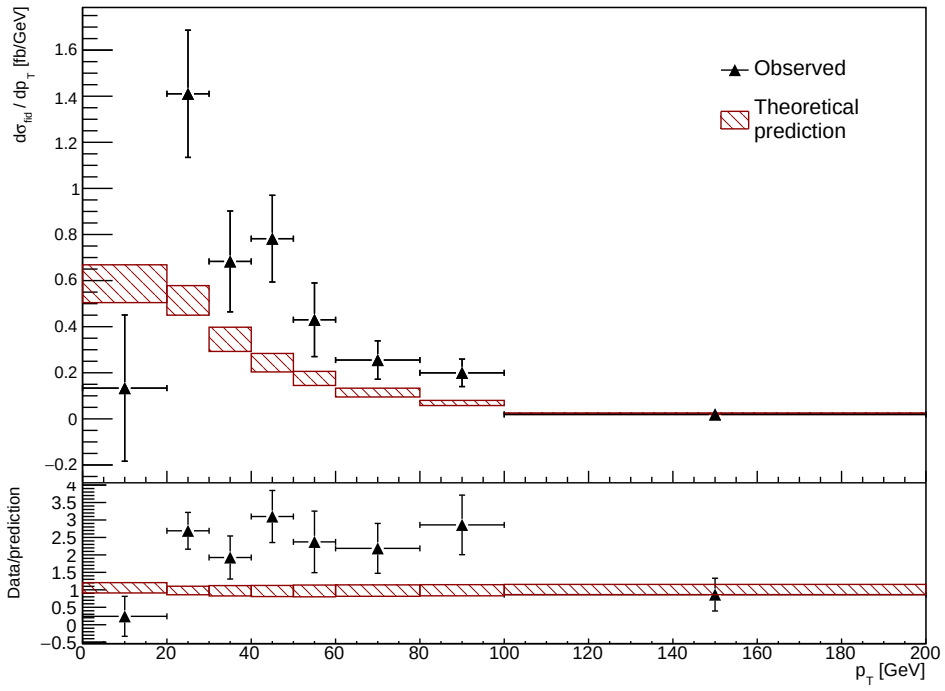

FIGURE 6.13: The measured differential cross-section in p_{T}, in the region 0–200 GeV. The measurement from data is shown by the black points, and the error bars on each point show the combined statistical and systematic uncertainty. The shaded red area indicates the theoretical prediction described in section 6.5. The uncertainty on the theoretical prediction is indicated by the shaded area.

6.12.2 Production Modes

The result of performing fitting procedure described in section 6.11 on the observed spectrum is shown in histogram form in figure 6.14 and in tabular form in table 6.7.

Component	Theoretical prediction ($\sigma_{\text{component}}/\sigma_{\text{SM}}$)	Fitted contribution ($\sigma_{\text{component}}/\sigma_{\text{SM}}$)
Gluon-gluon fusion	0.87	1.15 ± 0.32
Other production modes	0.13	0.06 ± 0.14

TABLE 6.7: This table shows the fitted contributions from gluon-gluon fusion and other production modes to the measured $H \to \gamma\gamma$ differential cross-section in p_{T}. The size of the fitted contribution is given in terms of σ_{SM}, the total cross-section predicted by the Standard Model for a Higgs boson with mass $m_H = 125\,\mathrm{GeV}$ in collisions at centre-of-mass energy $\sqrt{s} = 8\,\mathrm{GeV}$. The theoretical predictions[35] are also presented.

As an illustration of the relative contributions of the various sources of uncertainty on the measurement presented above, figure 6.15 presents the uncertainties for

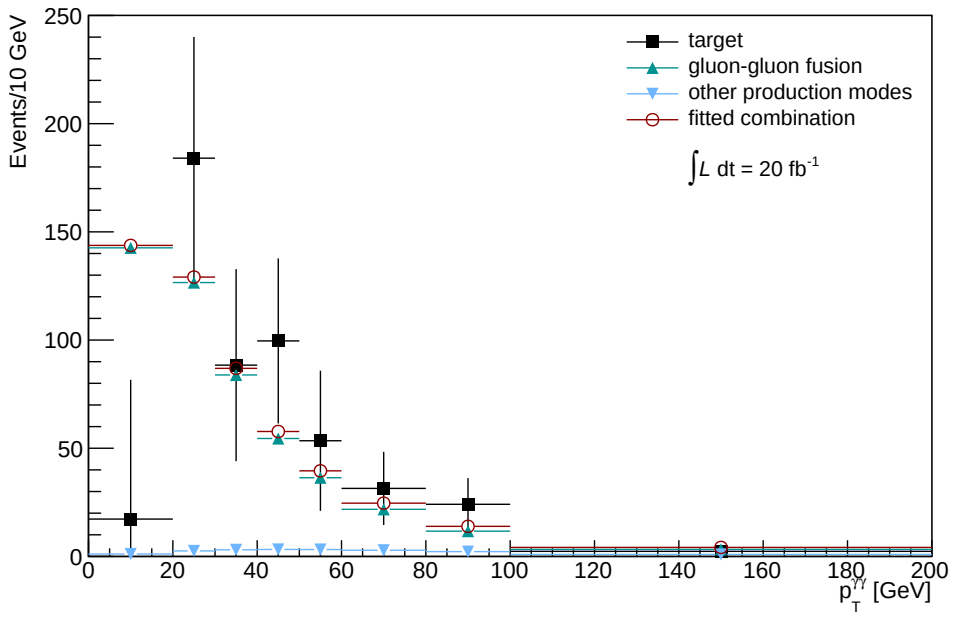

FIGURE 6.14: The above plot shows, in black, the observed Higgs p_{T} spectrum. The error bars correspond to the total systematic plus statistical uncertainty on the measured yield. The fitted gluon-gluon component is indicated by the green, up-wards-pointing triangles, and the contribution from other production modes is indicated by the blue, downwards-pointing triangles. The fitted combination is indicated by the hollow red circles. The uncertainties on the fitted components and the total fit are not shown here for reasons of legibility, but are quoted numerically in table 6.7.

each bin, broken down to show separately the uncertainties resulting from the fitting procedure. As expected, the largest contribution to the uncertainty on the measurement comes from the statistical component of the uncertainty resulting from the fitting procedure. The scale of this uncertainty is highly dependent upon the size of the dataset. As described in section 6.11.2, a study is performed into the effect increasing the size of the dataset may have on the precision with which the relative cross-sections of different Higgs boson production mechanisms may be measured from observations of the p_{T} spectrum.

In figure 6.16, example results are shown from individual instances of the procedure described in section 6.11. These individual instances, as explained in section 6.11.2, are prone to significant statistical fluctuations, and so the results of the procedure are evaluated on a larger sample of 10000 iterations at each of the three chosen luminosity working points.

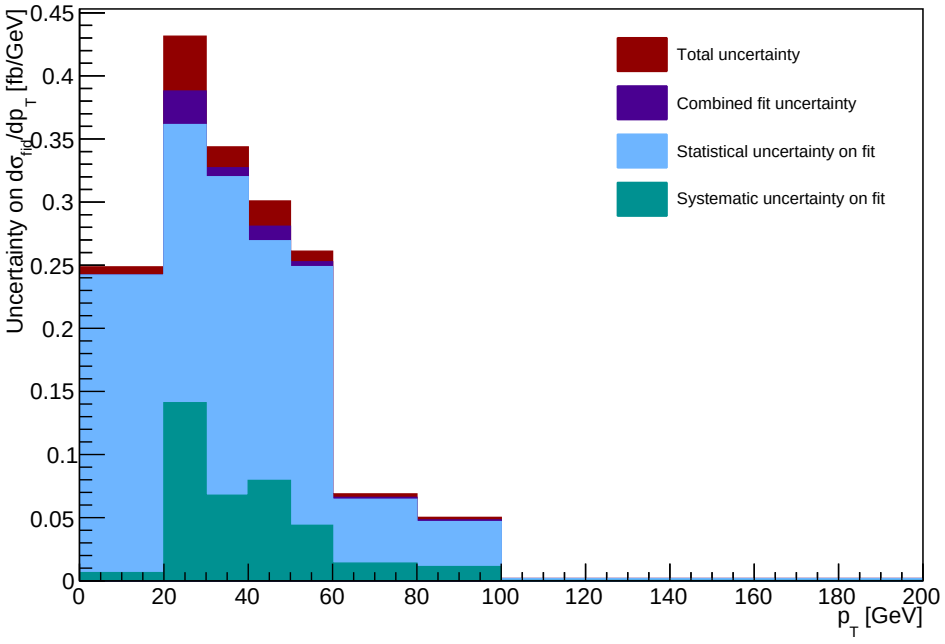

FIGURE 6.15: A breakdown of the uncertainties on the measured p_{T} spectrum in each bin. All of the displayed uncertainties are symmetrical, only the positive region of the y-axis is displayed.

Because each pseudodata set is generated from the theoretically predicted distributions plus simulated statistical fluctuations, it is expected that for each of working points, the distribution of fitted contributions from the ggF and non-ggF production categories will form approximately Gaussian distributions, centred on the values predicted by theory. Increasing the size of the dataset is not expected to improve the average value obtained over many iterations of this procedure. Increased sample size should, however, lead to a lower impact from statistical fluctuations on any individual measurement. As such, the average uncertainty is expected to decrease and the distribution of measured central values is expected to become narrower as the size of the pseudodata set increases. The distributions of the fitted ggF and non-ggF components are shown for each working point in subfigures 6.17(a) to 6.17(c), and the results correspond to these expectations. Section 6.12.2 shows the standard deviation of the measured value and the average uncertainty, for each component at each of the chosen luminosity working points. The expected reduction in these quantities at higher luminosity is observed. The

study suggests that with an integrated luminosity of $300\,\mathrm{fb}^{-1}$, it would be possible to measure the fractional contribution from gluon-gluon fusion production with an uncertainty of around 15 %, and the contribution from other production modes with an uncertainty on the order of 5 %. Such values would represent improvements by factors of approximately 2 and 3 respectively, in comparison to the uncertainties reached when performing this study on the current dataset.

Luminosity (fb^{-1})	$\sigma_{f\mathrm{ggF}}$	$\langle\delta f_{\mathrm{ggF}}\rangle$	$\sigma_{f\mathrm{other}}$	$\langle\delta f_{\mathrm{other}}\rangle$
203	0.06	0.15	0.05	0.06
300	0.06	0.13	0.06	0.06
2030	0.04	0.09	0.03	0.03

Projection of standard deviation and mean uncertainty of the fitted ggF and non-ggF components, at each of the chosen luminosity working points, as a fraction of the total $H \to \gamma\gamma$ cross-section for a Standard Model Higgs boson decaying in the with mass $m_H = 125\,\mathrm{GeV}$.

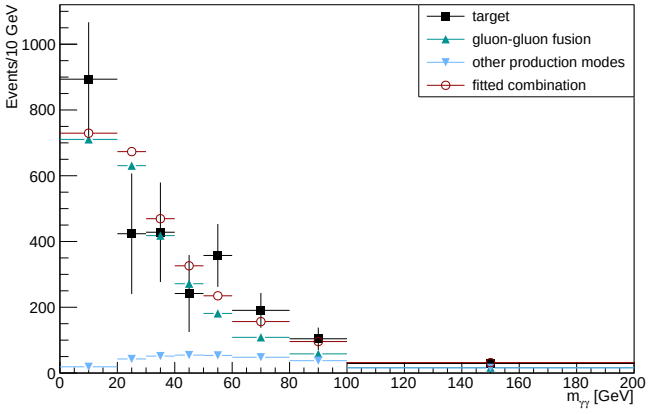

(a)

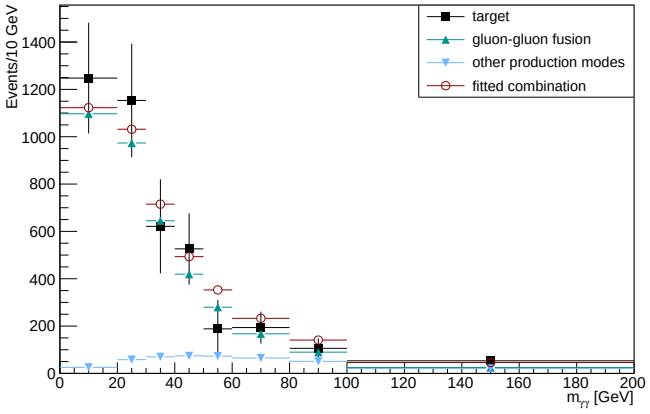

(b)

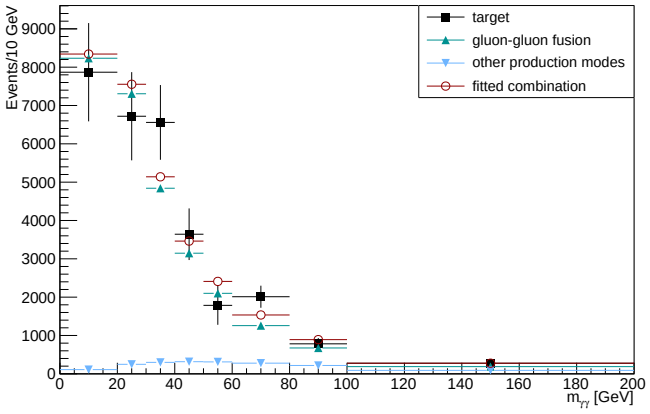

(c)

FIGURE 6.16: Subfigures 6.16(a) to 6.16(c) show examples of pseudodata $m_{\gamma\gamma}$ distributions at the 203 fb^{-1}, 300 fb^{-1}, and 2030 fb^{-1} luminosity working points, respectively. In each case, the pseudodata distribution is shown by the black points, with error bars indicating combined systematic and statistical uncertainty, the gluon-gluon fusion component of the template fit to this distribution is indicated by the green, upwards-pointing triangles, and the contribution from other production modes is indicated by the blue, downwards-pointing triangles. The fitted combination of all production modes is indicated by the hollow red circles.

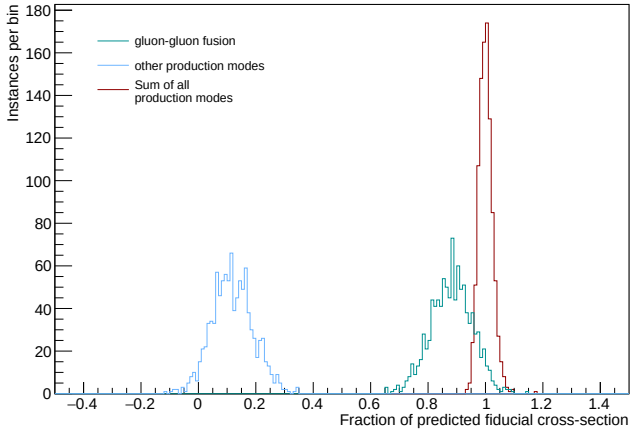

(a)

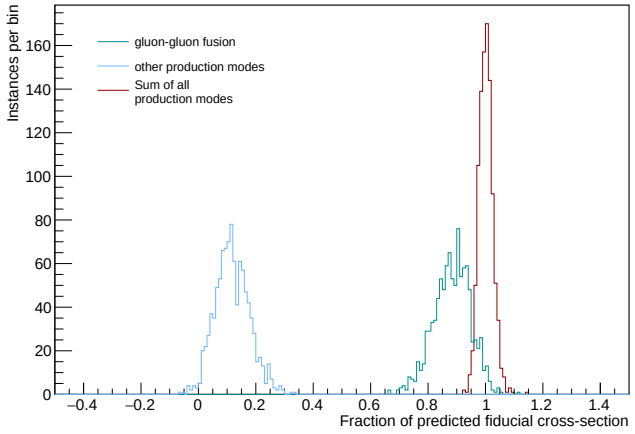

(b)

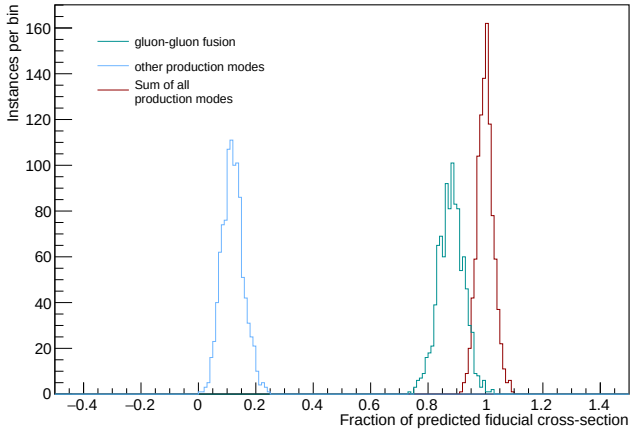

(c)

FIGURE 6.17: Subfigures 6.17(a) to 6.17(c) show the distribution of the contributions of various Higgs boson production modes, as fitted in pseudodatasets at various integrated luminosities. Subfigures 6.17(a) to 6.17(c) correspond to integrated luminosities of $203\,\mathrm{fb}^{-1}$, $300\,\mathrm{fb}^{-1}$, and $2030\,\mathrm{fb}^{-1}$, respectively. In each case, the distribution of fitted ggF contributions is indicated in green, the contribution from other production modes is indicated in blue, and the fitted combination of all production modes is indicated in red. Each distribution indicates the fitted contribution as a fraction of the total $H \to \gamma\gamma$ cross-section predicted by the Standard Model.

Chapter 7

Summary

A measurement is made of the identification efficiency for isolated photons with the ATLAS detector, using 20.3 fb^{-1} of proton-proton collision data taken in 2012. The efficiency is measured separately for converted photons and unconverted photons as a function of transverse momentum, p_{T}, over a p_{T} range of 30–100 GeV, in four η regions. The method used takes advantage of similarities between electrons and photons to provide a data-driven measurement in a p_{T} region for which it is impractical to obtain a large photon sample from data with high purity. Converted photons are found to be correctly identified with an efficiency of approximately 85–90 % in the lowest p_{T} bins, and greater than 97 % at the highest p_{T} bins. The identification efficiency for unconverted photons is found to range from 80–85 % in the lowest p_{T} bins to 90–95 % in the highest p_{T} bins, with some dependence on η. Several systematic uncertainties are evaluated to account for the extrapolation from electrons to photons, uncertainty in detector simulation in MC samples, and background contamination. The total uncertainty on the identification efficiency measurement varies from 1.5–6.0 % for converted photons and 1.7–7.4 % for unconverted photons.

A measurement of the differential $H \rightarrow \gamma\gamma$ cross-section as a function of p_{T}, has been performed using $20.3\,\mathrm{fb}^{-1}$ of proton-proton collision data taken by the ATLAS Experiment in 2012. The measured signal yield is very sensitive to the photon identification efficiency, and the analysis benefits from the precise photon identification efficiency measurement. The largest systematic uncertainties correspond to uncertainties on the measurement of the diphoton invariant mass resolution, and uncertainties resulting from the fitting procedure used to measure the signal yield in each p_{T} bin. In each p_{T} bin, the statistical uncertainty is significantly larger than the total systematic uncertainty. The measured distribution is compared to theoretical predictions, and is found to be broadly compatible with the predictions to within the uncertainties on the measurement.

Using the measured p_{T} distribution, an estimate is made of the fractional contributions to the total Higgs boson production which arise from gluon-gluon fusion, and from the combination of all other production modes. The results are compatible with theoretical predictions, within the uncertainties on the measurement. Due to the size of the dataset, the statistical uncertainties on this measurement are also large. A follow-up study is performed to evaluate how the power of this method to estimate the relative contributions of the different production modes is likely to evolve as further data is taken.

Bibliography

[1] ATLAS Collaboration, *Measurement of the photon identification efficiencies with the ATLAS detector using LHC Run-1 data*, Eur. Phys. J. **C76** (2016) no. 12, 666, arXiv:1606.01813 [hep-ex].

[2] ATLAS Collaboration, *Measurements of fiducial and differential cross sections for Higgs boson production in the diphoton decay channel at* $\sqrt{s} = 8\,\text{TeV}$ *with ATLAS*, Tech. Rep. arXiv:1407.4222. CERN-PH-EP-2014-148, Jul, 2014. https://cds.cern.ch/record/1743175.

[3] LHCb Collaboration, *Observation of the resonant character of the* $Z(4430)^-$ *state*, Tech. Rep. arXiv:1404.1903. LHCB-PAPER-2014-014. CERN-PH-EP-2014-061, CERN, Geneva, Apr, 2014.

[4] S. L. Glashow, *Partial-symmetries of weak interactions*, Nuclear Physics **22** (1961) no. 4, 579–588.

[5] S. Weinberg, *A Model of Leptons*, Phys. Rev. Lett. **19** (1967) 1264–1266.

[6] A. Salam, *Weak and electromagnetic interactions*. Stockholm, 1968.

[7] P. W. Higgs, *Broken symmetries, massless particles and gauge fields*, Physics Letters **12** (1964) no. 2, 132–133.

[8] F. Englert and H. R. Brout, *Broken symmetry and the mass of gauge vector mesons*, Physical review letters **13** (1964) no. 9, 321–323.

[9] G. S. Guralnik, C. R. Hagen, and T. W. B. Kibble, *Global Conservation Laws and Massless Particles*, Phys. Rev. Lett. **13** (1964) 585–587. http://link.aps.org/doi/10.1103/PhysRevLett.13.585.

[10] P. W. Higgs, *Spontaneous Symmetry Breakdown without Massless Bosons*, Phys. Rev. **145** (1966) 1156–1163. http://link.aps.org/doi/10.1103/PhysRev.145.1156.

[11] A. Djouadi, *The anatomy of electro-weak symmetry breaking. I: The Higgs boson in the standard model. Phys. Rept., 457: 1–216, 2008*, arXiv preprint hep-ph/0503172 .

[12] J. Goldstone, A. Salam, and S. Weinberg, *Broken symmetries*, Physical Review **127** (1962) 965–970.

[13] ATLAS Collaboration, *Observation of a new particle in the search for the Standard Model Higgs boson with the ATLAS detector at the LHC*, Physics Letters B **716** (2012) no. 1, 1–29.

[14] CMS Collaboration, *Observation of a new boson at a mass of* 125 GeV *with the CMS experiment at the LHC*, arXiv preprint arXiv:1207.7235 (2012) .

[15] LHC Higgs Cross Section Working Group, S. Dittmaier, C. Mariotti, G. Passarino, and R. Tanaka (Eds.), *Handbook of LHC Higgs Cross Sections: 1. Inclusive Observables*, CERN-2011-002 (CERN, Geneva, 2011) , arXiv:1101.0593 [hep-ph].

[16] S. Dawson, *Radiative corrections to Higgs boson production*, Nuclear Physics B **359** (1991) no. 2, 283–300.

[17] A. Djouadi, M. Spira, and P. M. Zerwas, *Production of Higgs bosons in proton colliders. QCD corrections*, Physics Letters B **264** (1991) no. 3, 440–446.

[18] M. Spira, A. Djouadi, D. Graudenz, and R. Zerwas, *Higgs boson production at the LHC*, Nuclear Physics B **453** (1995) no. 1, 17–82.

[19] R. V. Harlander and W. B. Kilgore, *Next-to-next-to-leading order Higgs production at hadron colliders*, Physical Review Letters **88** (2002) no. 20, 201801.

[20] C. Anastasiou and K. Melnikov, *Higgs boson production at hadron colliders in NNLO QCD*, Nuclear Physics B **646** (2002) no. 1, 220–256.

[21] V. Ravindran, J. Smith, and W. Van Neerven, *NNLO corrections to the total cross section for Higgs boson production in hadron–hadron collisions*, Nuclear Physics B **665** (2003) 325–366.

[22] U. Aglietti, R. Bonciani, G. Degrassi, and A. Vicini, *Two-loop light fermion contribution to Higgs production and decays*, Physics Letters B **595** (2004) no. 1, 432–441.

[23] G. Degrassi and F. Maltoni, *Two-loop electroweak corrections to Higgs production at hadron colliders*, Physics Letters B **600** (2004) no. 3, 255–260.

[24] U. Aglietti, R. Bonciani, G. Degrassi, and A. Vicini, *Two-loop electroweak corrections to Higgs production in proton-proton collisions*, arXiv preprint hep-ph/0610033 (2006) .

[25] M. Ciccolini, A. Denner, and S. Dittmaier, *Strong and electroweak corrections to the production of a higgs boson+ 2 jets via weak interactions at the large hadron collider*, Physical review letters **99** (2007) no. 16, 161803.

[26] M. Ciccolini, A. Denner, and S. Dittmaier, *Electroweak and QCD corrections to Higgs production via vector-boson fusion at the CERN LHC*, Physical Review D **77** (2008) no. 1, 013002.

[27] M. Zaro, P. Bolzoni, F. Maltoni, S.-O. Moch, et al., *Higgs production via vector-boson fusion at NNLO in QCD*, PoS DIS2010 **211** (2010) .

[28] O. Brein, A. Djouadi, and R. Harlander, *NNLO QCD corrections to the Higgs-strahlung processes at hadron colliders*, Physics Letters B **579** (2004) no. 1, 149–156.

[29] T. Han and S. Willenbrock, *QCD correction to the pp WH and ZH total cross sections*, Physics Letters B **273** (1991) no. 1, 167–172.

[30] M. Ciccolini, S. Dittmaier, and M. Krämer, *Electroweak radiative corrections to associated WH and ZH production at hadron colliders*, Physical Review D **68** (2003) no. 7, 073003.

[31] W. Beenakker, S. Dittmaier, M. Krämer, B. Plümper, M. Spira, and P. Zerwas, *NLO QCD corrections to ttH production in hadron collisions*, Nuclear Physics B **653** (2003) no. 1, 151–203.

[32] S. Dawson, L. Orr, L. Reina, and D. Wackeroth, *Next-to-leading order QCD corrections to p p t t⁻ h at the CERN Large Hadron Collider*, Physical Review D **67** (2003) no. 7, 071503.

[33] S. Dawson, C. Jackson, L. Orr, L. Reina, and D. Wackeroth, *Associated Higgs boson production with top quarks at the CERN Large Hadron Collider: NLO QCD corrections*, Physical Review D **68** (2003) no. 3, 034022.

[34] W. Beenakker, S. Dittmaier, M. Krämer, B. Plümper, M. Spira, and P. Zerwas, *Higgs radiation off top quarks at the Tevatron and the LHC*, Physical Review Letters **87** (2001) no. 20, 201805.

[35] S. Heinemeyer, C. Mariotti, G. Passarino, R. Tanaka, J. Andersen, P. Artoisenet, E. Bagnaschi, A. Banfi, T. Becher, F. Bernlochner, et al.,

Handbook of LHC Higgs cross sections: 3. Higgs properties, arXiv preprint arXiv:1307.1347 (2013) .

[36] M. Botje, J. Butterworth, A. Cooper-Sarkar, A. De Roeck, J. Feltesse, S. Forte, A. Glazov, J. Huston, R. McNulty, T. Sjostrand, et al., *The PDF4LHC working group interim recommendations*, arXiv preprint arXiv:1101.0538 (2011) .

[37] P. Lebrun, S. Myers, O. S. Brüning, R. Ostojic, P. Collier, P. Proudlock, and J. Poole, *LHC Design Report*, tech. rep., CERN, 2004.

[38] C. Lefevre, *LHC: the guide (English version). Guide du LHC (version anglaise)*, Feb, 2009.

[39] L. Ponce, *LHC Machine Upgrades*, LHC France 2013, Annecy, 2013.

[40] L. Evans and P. Bryant, *LHC machine*, Journal of Instrumentation **3** (2008) no. 08, S08001.

[41] ATLAS Collaboration, *The ATLAS experiment at the CERN large hadron collider*, Journal of Instrumentation **3** (2008) no. 08, S08003.

[42] ATLAS Experiment public images http://www.atlas.ch/photos/index.html .

[43] ATLAS Collaboration, *ATLAS Inner Detector Technical Design Report*, CERN/LHCC (1997) 97–16.

[44] ATLAS Collaboration, *ATLAS liquid-argon calorimeter: Technical Design Report*. Technical Design Report ATLAS. CERN, Geneva, 1996.

[45] P. Krieger, *The ATLAS liquid argon calorimeter*, in *2005 IEEE Nuclear Science Symposium Conference Record*, pp. 1029–1033. 2005.

[46] ATLAS Collaboration, *ATLAS calorimeter performance: Technical Design Report*. Technical Design Report ATLAS. CERN, Geneva, 1996.

[47] ATLAS Collaboration, *ATLAS detector and physics performance: Technical Design Report, 1.* Technical Design Report ATLAS. CERN, Geneva, 1999. Electronic version not available.

[48] ATLAS Collaboration, *ATLAS tile calorimeter: Technical Design Report.* Technical Design Report ATLAS. CERN, Geneva, 1996.

[49] A. Artamonov, D. Bailey, G. Belanger, M. Cadabeschi, T.-Y. Chen, V. Epshteyn, P. Gorbounov, K. Joo, M. Khakzad, V. Khovanskiy, et al., *The ATLAS forward calorimeter*, Journal of Instrumentation **3** (2008) no. 02, P02010.

[50] Y. Takahashi, *ATLAS Muon Spectrometer*, .

[51] Atlas Collaboration, *ATLAS Muon Spectrometer Technical Design Report*, CERN/LHCC **97** (1997) 22.

[52] J. Bystricky, D. Calvet, J. Ernwein, O. Gachelin, T. Hansl-Kozanecka, J. R. Hubbard, M. Huet, P. Le Du, I. Mandjavidze, M. Mur, et al., *A sequential processing strategy for the ATLAS event selection*, Nuclear Science, IEEE Transactions on **44** (1997) no. 3, 342–347.

[53] ATLAS Collaboration, *Improved luminosity determination in pp collisions at* $\sqrt{s} = 7\,\text{TeV}$ *using the ATLAS detector at the LHC*, The European Physical Journal C **73** (2013) no. 8, 1–39.

[54] *ATLAS Luminosity Public Results*, `https://twiki.cern.ch/twiki/bin/view/AtlasPublic/LuminosityPublicResults`, 2012.

[55] *Electron efficiency measurements with the ATLAS detector using the 2012 LHC proton-proton collision data*, Tech. Rep. ATLAS-CONF-2014-032, CERN, Geneva, Jun, 2014.

[56] W. Lampl, S. Laplace, D. Lelas, P. Loch, H. Ma, S. Menke, S. Rajagopalan, D. Rousseau, S. Snyder, and G. Unal, *Calorimeter Clustering Algorithms: Description and Performance*, Tech. Rep. ATL-LARG-PUB-2008-002. ATL-COM-LARG-2008-003, CERN, Geneva, Apr, 2008.

[57] V. Gallo, *Identification and reconstruction of electrons and photons with the ATLAS detector at the LHC.*, Tech. Rep. ATL-PHYS-PROC-2012-044, CERN, Geneva, Feb, 2012.

[58] T. Cornelissen, M. Elsing, I. Gavrilenko, W. Liebig, and A. Salzburger, *Single Track Performance of the Inner Detector New Track Reconstruction (NEWT)*, Tech. Rep. ATL-INDET-PUB-2008-002. ATL-COM-INDET-2008-004, CERN, Geneva, Mar, 2008.

[59] T. Cornelissen, M. Elsing, S. Fleischmann, W. Liebig, E. Moyse, and A. Salzburger, *Concepts, Design and Implementation of the ATLAS New Tracking (NEWT)*, Tech. Rep. ATL-SOFT-PUB-2007-007. ATL-COM-SOFT-2007-002, CERN, Geneva, Mar, 2007.

[60] R. Frühwirth, *Application of Kalman filtering to track and vertex fitting*, Nuclear Instruments and Methods in Physics Research Section A: Accelerators, Spectrometers, Detectors and Associated Equipment **262** (1987) no. 2, 444–450.

[61] G. Welch and G. Bishop, *An introduction to the Kalman filter*, 1995.

[62] D. Wicke, *A New Algorithm For Solving Track Ambiguities*, Tech. Rep. DELPHI 98-163, PROG 236 TRACK 92, 1998.

[63] T. Cornelissen, M. Elsing, I. Gavrilenko, J. Laporte, W. Liebig, M. Limper, K. Nikolopoulos, A. Poppleton, and A. Salzburger, *The global $\chi 2$ track fitter in ATLAS*, in *Journal of Physics: Conference Series*, vol. 119, p. 032013. 2008.

[64] V. Lacuesta, *Track and Vertex Reconstruction in the ATLAS Experiment*, Tech. Rep. ATL-INDET-PROC-2012-034, CERN, Geneva, Dec, 2012.

[65] M. Tibbetts, *Tracking, vertexing and b-tagging performance in ATLAS*, Tech. Rep. ATL-PHYS-PROC-2012-307, CERN, Geneva, Dec, 2012.

[66] *Reconstruction of Photon Conversions*, Tech. Rep. ATL-PHYS-PUB-2009-006. ATL-COM-PHYS-2009-172, CERN, Geneva, Apr, 2009. CSC PUB Note.

[67] J. Hartert and I. Ludwig, *Electron isolation in the ATLAS experiment*, Tech. Rep. ATL-PHYS-INT-2010-052, CERN, Geneva, May, 2010.

[68] S. Laplace and J. de Vivie, *Calorimeter isolation and pile-up*, Tech. Rep. ATL-COM-PHYS-2012-467, CERN, Geneva, May, 2012.

[69] M. Hance, D. Olivito, and H. Williams, *Performance Studies for e/gamma Calorimeter Isolation*, Tech. Rep. ATL-COM-PHYS-2011-1186, CERN, Geneva, Sep, 2011.

[70] ATLAS Collaboration, *Electron and photon energy calibration with the ATLAS detector using LHC Run 1 data*, The European Physical Journal C **74** (2014) no. 10, 1–48.

[71] ATLAS Collaboration, *Expected Performance of the ATLAS Experiment, Detector, Trigger and Physics: Reconstruction and identification of photons*, `CERN-OPEN-2008-020`.

[72] ATLAS Collaboration, *Expected photon performance in the ATLAS experiment*, ATL-PHYS-PUB-2011-007 (2011) .

[73] C. Anastopoulos, E. Benhar-Noccioli, A. Bocci, K. Brendlinger, F. Bhrer, L. Iconomidou-Fayard, M. Delmastro, O. Ducu, R. Fletcher, D. Froidevaux, T. Guillemin, S. Heim, F. Hubaut, M. Karnevskiy,

J. Kretzschmar, J. Kroll, C. Lester, K. Lohwasser, J. B. Maurer, A. Morley, G. Psztor, E. Richter-Was, A. Schaffer, T. Serre, P. Sommer, E. Tiouchichine, and H. Williams, *Supporting document on electron efficiency measurements using the 2012 LHC proton-proton collision data*, Tech. Rep. ATL-COM-PHYS-2013-1295, CERN, Geneva, Sep, 2013.

[74] L. Devroye, *Sample-based non-uniform random variate generation*, in *Proceedings of the 18th conference on Winter simulation*, pp. 260–265, ACM. 1986.

[75] S. Catani, M. Fontannaz, J.-P. Guillet, and E. Pilon, *Cross section of isolated prompt photons in hadron-hadron collisions*, Journal of High Energy Physics **2002** (2002) no. 05, 028.

[76] P. Aurenche, J. P. Guillet, E. Pilon, M. Werlen, and M. Fontannaz, *Recent critical study of photon production in hadronic collisions*, Phys. Rev. D **73** (2006) 094007.

[77] K. Liu, Y. Liu, G. Marchiori, and E. Soldatov, *Measurement of the identification efficiency of isolated prompt photons using radiative $Z \to \ell\ell\gamma$ decays in 20.7 fb^{-1} of pp collisions at $\sqrt{s} = 8\,\text{TeV}$*, Tech. Rep. ATL-COM-PHYS-2013-1639, CERN, Geneva, Dec, 2013.

[78] M. Kuna, K. Liu, Y. Liu, G. Marchiori, and M. Pitt, *Measurement of the identification efficiency of isolated prompt photons with the "matrix method" in pp collisions at $\sqrt{s} = 8\,\text{TeV}$ using 21.0fb^{-1} of ATLAS data*, Tech. Rep. ATL-COM-PHYS-2013-1628, CERN, Geneva, Dec, 2013.

[79] A. Valassi, *Combining correlated measurements of several different physical quantities*, Nuclear Instruments and Methods in Physics Research Section A: Accelerators, Spectrometers, Detectors and Associated Equipment **500** (2003) no. 1, 391–405.

[80] CERN, *CERN experiments observe particle consistent with long-sought Higgs boson*, http://press.web.cern.ch/press-releases/2012/07/cern-experiments-observe-particle-consistent-long-sought-higgs-boson, 2012. [Online; accessed 25-August-2014].

[81] ATLAS Collaboration, *Evidence for the spin-0 nature of the Higgs boson using ATLAS data*, Physics Letters B **726** (2013) no. 13, 120 – 144. http://www.sciencedirect.com/science/article/pii/S0370269313006527.

[82] CMS Collaboration, *Study of the Mass and Spin-Parity of the Higgs Boson Candidate via Its Decays to Z Boson Pairs. On the mass and spin-parity of the Higgs boson candidate via its decays to Z boson pairs*, Phys. Rev. Lett. **110** (2012) no. arXiv:1212.6639. CMS-HIG-12-041. CERN-PH-EP-2012-372, 081803. 25 p.

[83] ATLAS Collaboration, *Measurements of Higgs boson production and couplings in diboson final states with the ATLAS detector at the LHC*, Phys.Lett. **B726** (2013) 88–119, arXiv:1307.1427 [hep-ex].

[84] CMS Collaboration, *Evidence for the direct decay of the* 125 GeV *Higgs boson to fermions*, Nature Phys. **10** (2014) no. arXiv:1401.6527. CMS-HIG-13-033. CERN-PH-EP-2014-004, xx. 25 p. Comments: Submitted to Nature Physics.

[85] P. Nason, *A new method for combining NLO QCD with shower Monte Carlo algorithms*, Journal of High Energy Physics **2004** (2004) no. 11, 040.

[86] S. Frixione, P. Nason, and C. Oleari, *Matching NLO QCD computations with Parton Shower simulations: the POWHEG method*, Journal of High Energy Physics **2007** (2007) no. 11, 070.

[87] S. Alioli, P. Nason, C. Oleari, and E. Re, *A general framework for implementing NLO calculations in shower Monte Carlo programs: the POWHEG BOX*, Journal of High Energy Physics **2010** (2010) no. 6, 1–58.

[88] S. Alioli, P. Nason, C. Oleari, and E. Re, *NLO Higgs boson production via gluon fusion matched with shower in POWHEG*, Journal of High Energy Physics **2009** (2009) no. 04, 002.

[89] T. Sjöstrand, S. Mrenna, and P. Skands, *A brief introduction to PYTHIA 8.1*, Computer Physics Communications **178** (2008) no. 11, 852–867.

[90] H.-L. Lai, M. Guzzi, J. Huston, Z. Li, P. M. Nadolsky, J. Pumplin, and C.-P. Yuan, *New parton distributions for collider physics*, Physical Review D **82** (2010) no. 7, 074024.

[91] S. Actis, G. Passarino, C. Sturm, and S. Uccirati, *NLO electroweak corrections to Higgs boson production at hadron colliders*, Physics Letters B **670** (2008) no. 1, 12–17.

[92] P. M. Nadolsky, H.-L. Lai, Q.-H. Cao, J. Huston, J. Pumplin, D. Stump, W.-K. Tung, and C.-P. Yuan, *Implications of CTEQ global analysis for collider observables*, Physical Review D **78** (2008) no. 1, 013004.

[93] T. Gleisberg, S. Höche, F. Krauss, M. Schönherr, S. Schumann, F. Siegert, and J. Winter, *Event generation with SHERPA 1.1*, Journal of High Energy Physics **2009** (2009) no. 02, 007.

[94] D. de Florian, G. Ferrera, M. Grazzini, and D. Tommasini, *Higgs boson production at the LHC: transverse momentum resummation effects in the $H\to\gamma\gamma$, $H\to WW\to\ell\nu\ell\nu$ and $H\to ZZ\to 4\ell$ decay modes*, Journal of High Energy Physics **2012** (2012) no. 6, 1–26.

[95] A. Martin, W. J. Stirling, R. S. Thorne, and G. Watt, *Parton distributions for the LHC*, The European Physical Journal C **63** (2009) no. 2, 189–285.

[96] R. D. Ball, V. Bertone, S. Carrazza, C. S. Deans, L. Del Debbio, S. Forte, A. Guffanti, N. P. Hartland, J. I. Latorre, J. Rojo, et al., *Parton distributions with LHC data*, Nuclear Physics B **867** (2013) no. 2, 244–289.

[97] ATLAS Collaboration, *Measurement of Higgs boson production in the diphoton decay channel in pp collisions at center-of-mass energies of 7 and 8 TeV with the ATLAS detector*, Phys. Rev. **D90** (2014) no. 11, 112015, arXiv:1408.7084 [hep-ex].

[98] ATLAS Collaboration, *Measurement of the Higgs boson mass from the $H \to \gamma\gamma$ and $H \to ZZ^* \to 4\ell$ channels with the ATLAS detector using 25 fb^{-1} of pp collision data*, arXiv:1406.3827 [hep-ex].

[99] ATLAS Collaboration, *Differential cross sections of the Higgs boson measured in the diphoton decay channel using* 8 TeV *pp collisions*, Tech. Rep. ATLAS-CONF-2013-072, CERN, Geneva, Jul, 2013. http://cds.cern.ch/record/1562925.

[100] T. Skwarnicki, *A Study of the Radiative Cascade Transitions Between the Upsilon-prime and Upsilon Resonances*, . DESY-F31-86-02.

[101] HSG1 Working Group, *Measurement of fiducial and differential cross sections of the Higgs boson in the diphoton decay channel using centre-of-mass energy of* 8 TeV, Tech. Rep. ATL-COM-PHYS-2013-1664, CERN, Geneva, Dec, 2013. https://cds.cern.ch/record/1639554.

[102] N. Lorenzo Martinez and R. Turra, *Mass measurement in the $H \to \gamma\gamma$ channel: Supporting documentation for the Mass Paper*, Tech. Rep. ATL-COM-PHYS-2014-018, CERN, Geneva, Jan, 2014. https://cds.cern.ch/record/1642851.

[103] G. Cowan, K. Cranmer, E. Gross, and O. Vitells, *Asymptotic formulae for likelihood-based tests of new physics*, The European Physical Journal C **71** (2011) no. 2, 1–19.

[104] K. Hamilton, P. Nason, and G. Zanderighi, *MINLO: Multi-scale improved NLO*, J. High Energy Phys. **10** (2012) no. arXiv:1206.3572. CERN-PH-TH-2012-166. OUTP-12-11p. MCNET-12-07, 155. 27 p.

[105] J. Butterworth, J. Forshaw, M. Seymour, and R. Walker, *JIMMY Generator: Multiparton Interactions in Herweig*, `https://jimmy.hepforge.org`, 2004.

[106] HSG1 Working Group, *Selection for $H \to \gamma\gamma$ analysis supporting note, for Moriond 2013*, Tech. Rep. ATL-COM-PHYS-2013-093, CERN, Geneva, Jan, 2013. `https://cds.cern.ch/record/1510141`.

[107] D. A. Dicus and W. W. Repko, *Dalitz decay $H \to f\overline{f}\gamma$ as a background for $H \to \gamma\gamma$*, Physical Review D **89** (2014) no. 9, 093013.